Blast Mitigation using Cementitious Foams:

Experimental Investigation and Theoretical Development

By

WEIMIN NIAN

A dissertation submitted to the Graduate Faculty in Engineering in partial fulfillment of
the requirements for the degree of Doctor of Philosophy,
The City University of New York
2010

This manuscript has been read and accepted for the
Graduate Faculty in Engineering in satisfaction of the
dissertation requirement for the degree of Doctor of Philosophy.

Professor Kolluru V. Subramaniam

Date

Chair of Examining Committee

Professor Mumtaz K. Kassir

Date

Executive Officer

Professor Anil K. Agrawal, The City College of New York

Professor Hansong Tang, The City College of New York

Professor Huabei Liu, The City College of New York

Professor Feng-Bao Lin, The City College of New York

Professor Yiannis Andreopoulos, The City College of New York

Supervisory Committee

THE CITY UNIVERSITY OF NEW YORK

Abstract

Blast Mitigation using Cementitious Foams: Experimental Investigation and Theoretical Development

by

Weimin Nian

Advisor: Professor Kolluru V. Subramaniam

Blast vulnerability of buildings in an urban environment has motivated the Structural Engineering community to develop and implement blast mitigation strategies for existing structures. The work presented in this dissertation is aimed at researching the concept of a protective system for structural elements consisting of compressible, low-strength, cementitious foam. A cladding made of cement foam is intended for use as a sacrificial protective material, which would reduce the stress amplitude transmitted to the structural element from an applied blast pressure loading. The attenuation of the applied pressure loading is produced by the irreversible compaction of the material. Brittle shattering or spalling of structural elements, primarily made of reinforced concrete or brick masonry, can be prevented or suppressed in cement foam cladded structures.

Experiments were conducted to investigate the quasi-static and dynamic response of cement foam. Instrumentation for accurately measuring the applied blast pressure and the stress pulse transmitted through the foam to the structural element were developed. Specimens made of cement foams of different densities and lengths were evaluated for different blast pressure loadings. The cementitious foams exhibit a concave stress-strain relationship associated with crushing of cells, which leads to densification of the material.

Under blast loading, a compaction front which exhibits shock-type characteristics, forms and propagates in the foam. The compaction front creates an interface which separates the densified material consisting of crushed cells from the uncrushed cells. Experimental results identified a critical length, L_{cr}, which depends on the stress-strain response of the foam, required for completely attenuating an applied blast pressure loading. When foam of length larger than L_{cr} is used, there is a clear beneficial effect in reducing the amplitude of the transmitted stress. The blast pressure loading applied at one end of foam specimen is transmitted to the substrate as a rectangular shaped pulse. The stress amplitude of the rectangular pulse is close, but slightly higher than the crushing strength of cement foam. When a length smaller than L_{cr}, is used, there is an increase in the stress following the initial rectangular stress pulse. The stress enhancement can exceed the applied blast pressure amplitude when the length of foam is significantly smaller than L_{cr}.

Two approaches based on different representations of the bulk deformation of the cement foam were developed to predict the dynamic compaction of the cement foam under transient loadings. The first approach considers a rigid-plastic-plastic-locking (RPPL) idealization of the quasi-static stress-strain curve and results in a simplified one-dimensional ‘shock’ model. Closed form solutions for calculating L_{cr} and the transmitted stress when the length of foam exceeds L_{cr} were also obtained analytically for typical blast loadings. The second approach considers the actual stress-strain behavior of the foam, which, when combined with the conservation laws, results in a set of non-linear hyperbolic equations. A finite volume implementation of the hyperbolic conservation equations in a Lagrangian framework was developed. A Second-Order TVD version of WAF scheme based on the exact solution of the local Riemann problem successfully

predicted the wave structure consisting of the elastic wave and compaction fronts propagating in foam materials undergoing dynamic compression. The transmitted stress predicted by the exact Riemann based finite volume method compares favorably with the experimental measurement when the length of the foam is both larger and smaller than L_{cr}. The finite volume simulation provides an insight into the wave structure in the foam following blast wave incidence and leads to an understanding of the stress enhancement phenomenon. There is a steady attenuation of the compaction front, which results in diminishing its amplitude as it travels in the material. A completely diminished compaction front results in a reduce level of transmitted when the length of foam exceeds L_{cr}. The reflection of a partially attenuated compaction front leads to the stress enhancement when the length of the foam is less than L_{cr}.

A design guideline for using foam cladding to protect the structural elements made of quasi-brittle material, such as reinforced, un-reinforced concrete or masonry, for a prescribed level of projected threat from a blast is presented. The proposed design approach includes a two step process and considers damage mechanisms in two time scales associated with stress wave propagation and structural motion.

DEDICATION

To my family

ACKNOWLEDGEMENTS

I would like to express my sincere gratitude and appreciation to my advisor, Professor Kolluru V. Subramaniam for his continuous academic support, mentorship and moral support throughout my Ph.D. study.

My sincere appreciation also goes to the faculty members of Department of Civil Engineering and Mechanical Engineering at the City College of New York for their guidance and help. In particular, I would like to thank Professor Yiannis Andreopoulos, Professor Feng-Bao Lin, Professor Michel Ghosn, Professor Anil K. Agrawal, Professor Hansong Tang and Professor Huabei Liu.

I would also like to sincerely acknowledge the support of Dr. Xu Zhou, Dr. Mingdong Bi, Dr. Zhihua Yi, Mr. Vahid Kamyab, Mr. Hadi kamyab, Mr. Guangyong Liu and Mr. Xiaojun Wang for their help, assistance and encouragement.

Finally, I am always grateful to my wife Jie Xu for her unconditional love.

…

TABLE OF CONTENTS

Chapter 1: Introduction 1
  1.1. Introduction 1
  1.2. Outline of Work 6
  1.3. Organization of the Dissertation 7
Chapter 2: Literature Review 10
  2.1. Introduction 10
  2.2. Experimental Investigation of Dynamic Response of Foams 12
    2.2.1. Low-density Electrometric Foams under Shock Loading 12
    2.2.2. Rigid Metal Foams under Shock Loading 14
    2.2.3. Metal Foams under Impact Loading 14
    2.2.4. Foams under Blast Loading 20
    2.2.5. Summary of Experimental Results 23
  2.3. Modeling the Dynamic Response of Foams 24
    2.3.1. One-phase Approach 25
    2.3.2. Two-phase Approach 32
  2.4. Conclusions 35
Chapter 3: An Evaluation of the Dynamic Compaction of Foam under Air Blast Loading Considering Fluid-structure Interaction Effects 36
  3.1. Introduction 36
  3.2. Dynamic Compaction of Foam 39
    3.2.1. Critical Length and Maximum Displacement 42
  3.3. Objectives 44
  3.4. Problem Statement 44
  3.5. Numerical Discretization 46
    3.5.1. Fluid Medium 47
    3.5.2. Air-foam interface 52
  3.6. Results of Analysis 55
  3.7. Discussion 60
  3.8. Conclusions 69
Chapter 4: Finite Volume Implementation of a Riemann Solver for Evaluating Dynamic Compaction of Foams 71
  4.1. Introduction 71
  4.2. Problem Statement 75
  4.3. Solution of the Riemann Problem 77
    4.3.1 Wave Structure and Relations for Stress and Particle Velocity 78
    4.3.2. Formulation of the Riemann Problem (RP) 82
  4.4. Numerical Implementation and the Second-order Godunov Method 83
    4.4.1. Shock Capturing Scheme 84
    4.4.2. Treatment of Boundary Nodes 86
  4.5. Evaluation of the Numerical Scheme 88
    4.5.1. One Linear Wave Case 89
    4.5.2. One Compaction Wave Case 90
    4.5.3. One Linear Wave and One Compaction Front Case 91

    - 4.5.4. One Linear wave, One Compaction Front Followed by Linear Unloading Wave Case 93
  - 4.6. Discussion of the Numerical Results 94
  - 4.7. Foam Bar Subjected to Transient Loading 98
    - 4.7.1. Foam Bar Subjected to a Solid Impact 98
    - 4.7.2. Foam Bar Subjected to a Blast 101
  - 4.8. Summary and Conclusions 104
- Chapter 5: Dynamic Compaction of Cement Foam Subjected to Blast Load: Experimental Investigation and Theoretical Development 106
  - 5.1. Introduction 106
  - 5.2. Experimental Setup 110
    - 5.2.1. Shock tube for generating blast pressure waves 111
    - 5.2.2. Setup for measuring transmitted stress 115
    - 5.2.3. Sensors and Instrumentation 118
  - 5.3. Measurement procedure for applied blast pressure and transmitted stress 120
    - 5.3.1. Cement Foam 121
    - 5.3.2. Validation of the measurement procedure 125
    - 5.3.3. Calibration of the instrumented short rod 129
  - 5.4. Experimental Results with Cement Foam 133
    - 5.4.1. Foam samples of different lengths subjected to the same blast loading 135
    - 5.4.2. Analysis of Compacted Foam 138
    - 5.4.3. Transmitted stress for different blast when $L > L_{cr}$ 141
  - 5.5. Numerical Simulation 145
    - 5.5.1. The Exact Riemann Solver Based Finite Volume Scheme 145
    - 5.5.2. Prediction using the RPPL Idealization 155
  - 5.6. Discussion 158
    - 5.6.1. The Transmitted Stress through Foam Bar when $L > L_{cr}$ 158
    - 5.6.2. Critical Length L_{cr} and Stress Enhancement when $L < L_{cr}$ 162
  - 5.7. Conclusions 165
- Chapter 6: Design Guidelines for Foam Cladded Structure 168
  - 6.1. Introduction 168
  - 6.2. Development of Design Procedure 174
    - 6.2.1 Control the Stress (Stress Criteria) 175
    - 6.2.2 The Deflection-based Evaluation of the Structural Response to Transmitted Stress (Deflection Criteria) 180
  - 6.3. A Design Example 185
  - 6.4. Discussion 189
    - 6.4.1. Approach for using Blast Protection in a Blast Mitigation Strategy 193
  - 6.5. Conclusions 194

LIST OF FIGURES

Figure 1.1: Blast pressure wave produced by an explosion 1
Figure 1.2: Time scales in the blast response of a structural element 3
Figure 1.3: Schematic illustration of the proposed blast mitigation strategy. 6
Figure 2.1: Experimental evidences showing a sharp compaction front under high-velocity impacts cited from (a) Tan et al. [2005a] and (b) Radford et al. [2005]. 18
Figure 2.2: Photograph of layered sacrificial claddings and the experimental set-up by Guruprasad and Mukherjee [2000b]. 21
Figure 2.3: Schematic of the pendulum test set-up by Hanssen et al. [2002]. 22
Figure 2.4: Schematic compressive engineering stress-engineering strain curve for foams (solid line) and RPPL idealization (dotted lines). 28
Figure 3.1: Typical compressive stress-strain curve for foams and RPPL idealization (dotted lines) 37
Figure 3.2: Compaction of foam up to time *t*. 40
Figure 3.3: Setup for studying blast pressure wave interaction with foam. 45
Figure 3.4: Schematic of the numerical implementation of moving boundary problem for blast pressure loading of foam. 47
Figure 3.5: Schematic representation of solving for the Interfacial pressure and velocity53
Figure 3.6: Schematic representation of the algorithm for fluid-structure coupling 55
Figure 3.7: Comparison between uncoupled analysis and analysis considering FSI: (a), (b), (c) reflected pressure, displacement and velocity for σ_o =1MPa foam; (d), (e), and (f) reflected pressure, displacement and velocity for σ_o =5MPa foam. 58
Figure 3.8: Comparison of the applied blast over pressure and transmitted stress wave in the foam. 60
Figure 3.9: Control volume of shock front. 62
Figure 3.10: Jump across the shock chord for the RPPL material model. 63
Figure 3.11: The work done by the blast pressure wave and the energy during compaction of the foam, (a) σ_o =1Mpa; (b) σ_o =5Mpa. (I: Work done by blast; II: kinetic energy of the compacted foam; III: Energy dissipated under the shock chord; IV: Total energy; V: Energy dissipation under stress-strain curve). 65
Figure 3.12: Schematic representation of the time scales involved in the blast response of a structure 69
Figure 4.1: Typical stress-strain curve of foams (Aluminum, nominal density 351kg/m^3). 73
Figure 4.2: Case 1, (a) loading history and (b) wave structure. 79
Figure 4.3: Case 2, (a) loading history and (b) wave structure. 80
Figure 4.4: Case 3 (a) loading history and (b) wave structure 81
Figure 4.5: Wave structure associated with the local Riemann Problem 83
Figure 4.6: Structure of a typical local Riemann Problem for the current WAF scheme . 85
Figure 4.7: The computational domain and boundary cells 86
Figure 4.8: Left boundary conditions 88
Figure 4.9: (a) schematic of waves in the foam and (b) loading history of the foam for the case of one right running linear wave. 89
Figure 4.10: Comparison of numerical and exact solution for the case of one right running

linear wave: (a) particle velocity and (b) stress. 90
Figure 4.11: (a) schematic of waves in the foam and (b) loading history of the foam for the case of one right running compaction wave. 91
Figure 4.12: Comparison of numerical and exact solution for the case of one right running compaction wave: (a) particle velocity and (b) stress.. 91
Figure 4.13: (a) schematic of waves in the foam and (b) loading history of the foam for the case of one right running linear wave and compaction wave. 92
Figure 4.14: Comparison of numerical and exact solution for the case of one right running linear wave and compaction wave: (a) particle velocity and (b) stress. 92
Figure 4.15: (a) schematic of waves in the foam and (b) loading history of the foam for the case of one right running linear wave and compaction wave followed by one linear unloading wave. 93
Figure 4.16: Comparison of numerical and exact solution for the case of one right running linear wave and compaction wave followed by one linear unloading wave: (a) particle velocity and (b) stress. 94
Figure 4.17: The numerical results based on wave velocity $c_{1,2}$ evaluated using Equation 4.24.. 97
Figure 4.18: The numerical results based on wave velocity $c_{1,2}$ evaluated using Equation 4.25.. 97
Figure 4.19: Engineering strain–engineering stress curve for the Duocels Aluminum foam (40 ppi, nominal density=258 kg/m^3) 100
Figure 4.20: Transmitted stress history for the foam specimen impacted with a 1.46 kg projectile traveling at 52.6 m/s.. 100
Figure 4.21: Time history of the applied blast pressure and transmitted stress. 102
Figure 4.22: Stress induced in the foam bar at a successive time between (a) t=0~0.378ms and (b) t=0.454~0.795ms. 103
Figure 4.23: Energy dissipation associated with shock compaction in the foam. 103
Figure 5.1: Shock tube test facility: (a) photo and (b) schematic diagram. 1) driver section; 2) nozzle; 3) driven section; 4) instrumented step rod; 5) screw-driven piston; 6) high-pressure gas inlet; 7) diaphragm; 8) specimen; 9) pressure transducers. 112
Figure 5.2: Formation of a blast pressure wave in the shock tube.................................114
Figure 5.3: (a) Schematics and (b) photo of instrumented short rod. 118
Figure 5.4: Schematics of a constant current circuit (Cited from [www.micron-piezo.com/store/backedgage.aspx]).. 120
Figure 5.5: Lab Foam generator... 122
Figure 5.6: Photographs of the cement foam sample (a) cross-section and (b) a section along longitudinal axis 123
Figure 5.7: Static stress-strain curves of cement foams of different densities............... 124
Table 5.1: Parameters used for the fitted curves in Figure 5.7 124
Figure 5.8: (a) Ansys and (b) Dyna model of the short rod. 126
Figure 5.9: Stress history at a fixed location of the short rod due to a triangular pulse. (Applied: applied stress at the loaded end; Unfiltered: unfiltered original stress response at the measured point; Filtered: filtered stress.)... 128
Figure 5.10: Stress history at a point on the short rod due to two triangular pulses....... 129
Figure 5.11: Stress history from the instrumented short rod for a directly applied blast. (a) Applied pressure and calibrated filtered stress, (b) unfiltered and filtered voltage........ 132

Figure 5.12: (a) and (b): applied pressure and the calibrated filtered stress for different blast loadings. 132
Figure 5.13: Typical response of cement foam under blast loadings: (a) applied pressure and transmitted stress and (b) the impulse of applied pressure and transmitted stress... 134
Figure 5.14: Applied blast pressure versus transmitted stress under similar blast for three samples lengths (long, mid and short) and two densities: (a) 384 and (b) 480 kg/m^3. ... 137
Figure 5.15: Deformation of L = 184 mm sample made with the 384 kg/m^3 cement foam before and after compaction ($L > L_{cr}$ case), (a) face 1 and (b) face 2. 139
Figure 5.16: Engineering strain after compaction measured from Figure 5.15. 140
Figure 5.17: Deformation of L = 76 mm sample made with the 384 kg/m^3 cement foam before and after compaction ($L < L_{cr}$ case), (a) face 1 and (b) face 2. 140
Figure 5.18: Engineering strain after compaction measured from Figure 5.17. 141
Figure 5.19: Blast pressure versus transmitted stress under high, mid, and low blasts and for (a) 384 and (b) 480 kg/m^3 foams and the corresponding momentums (c) and (d). .. 144
Figure 5.20 Prediction of transmitted stress using exact Finite Volume Formulation and comparison to experimental results for $L>L_{cr}$. (a) 384 and (b) 480 kg/m^3. 147
Figure 5.21 Prediction of transmitted stress using Finite Volume Formulation and comparison to experimental results for L<Lcr. (a) 384 and (b) 480 kg/m3 cement foams. 148
Figure 5.22: Comparison of strain after compaction (numerical and experimental) for cases (a) $L > L_{cr}$ and (b) $L < L_{cr}$ 151
Figure 5.23: (a) Stress contour plot (stress unit: MPa) and (b) Strain contour plot for $L>L_{cr}$ corresponding to Figure 5.22 (a). 153
Figure 5.24: (a) Stress contour plot (stress unit: MPa) and (b) Strain contour plot for $L < L_{cr}$ corresponding to Figure 5.22 (b). 154
Figure 5.25: Actual stress-strain response and the RPPL idealization. 156
Figure 5.26: Prediction of transmitted stress using the shock model and comparison to experimental results for L > Lcr: (a) 384 kg/m^3 and (b) 480 kg/m^3. 157
Figure 5.27: Pre- and post-wave state across a (a) elastic precursor (before reflection) and (b) compaction front (after reflection). 161
Figure 5.28: States of cement foam before and after the reflection of an elastic precursor. 162
Figure 5.29: Stress in foam at a successive time between (a) t=119.5 ~363.3 s; (b) t=485.2~1338.7 s; (c) t=1485.0~1728.8 s. 164
Figure 5.30: (a) Strain and (b) particle velocity at a successive time between t=1485.0~1728.8 s. 164
Figure 6.1 (a) spalling due to stress wave reflection at back face at a short time scale and (b) final structural failure associate large deflection at a long time scale [YI 2009] 173
Figure 6.2: Schematic representation of the two step process. 175
Figure 6.3: p -i_L diagram for required foam length 179
Figure 6.4: Representation of stress transmitted through the foam and applied on the cladded structures on the p -iL diagram. 180
Figure 6.5 pressure-impulse diagram for rectangular pulse 184
Figure 6.6: A simply supported beam under uniform blast loads [Yi 2009, page 99] 186
Figure 6.7: Applied blast loads plotted on the P -i_l plot 187
Figure 6.8: check the displacement criteria 188

Figure 6.9: The effect of foam in the blast mitigation 190
Figure 6.10: Schematic representation of the role of stiffness of the structure in the blast mitigation strategy. 192
Figure 6.11: Schematic illustration of a blast mitigation strategy involving the combined use of protective material system and structural strengthening. 193

LIST OF TABLES

Table 5.1: Parameters used for the fitted curves in Figure 5.7 124
Table 6.1 Elastic properties of the Beam in Figure 6.6... 186
Table 6.2: Identified blast pressure loads.. 186
Table 6.3: Normalized blast loads according to Equations 6.7 and 6.8. 187
Table 6.4 normalized transmitted pulse according to Equations 6.14a and 6.14b.......... 188

Chapter 1: Introduction

1.1. Introduction

Blast vulnerability of buildings in an urban environment has motivated the Structural Engineering community to develop and implement blast mitigation strategies for existing buildings and structures. Studies have shown that in densely constructed space, buildings which are not the primary target will also be subjected to intense pressure loading not originally designed for. Developing blast retrofit measures primarily focuses on dealing with the pressure wave and its effects on buildings (as shown in Figure 1.1).

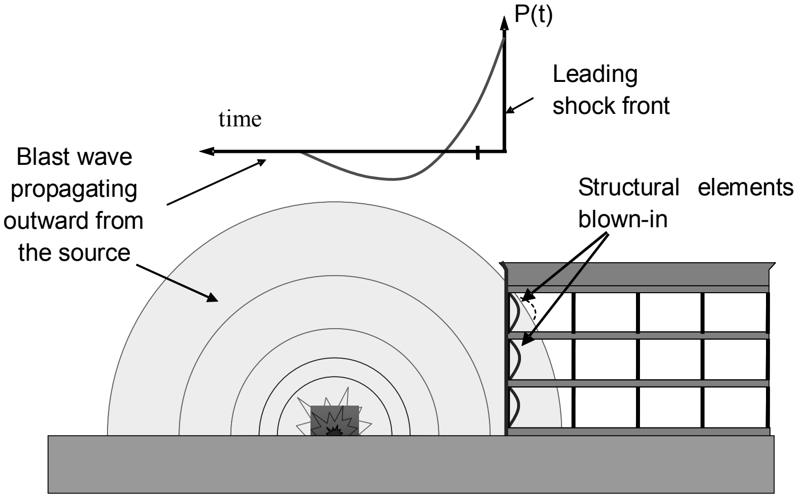

Figure 1.1: Blast pressure wave produced by an explosion

Engineering measures for blast mitigation primarily focus on minimizing the threat of, and the potential damage and casualties resulting from a blast pressure wave [Hinman 1998; DTRA/TSWG Status Report 1999]. The realistic objectives in developing blast mitigation strategies are: (a) to protect the occupants, the contents and the essential functions of a structure; (b) to provide adequate structural response under unexpected loads and load configurations not initially designed for; and (c) to provide for absorbing the extra energy due to blast loading [Hinman 1998, DTRA/TSWG Status Report 1999].

A blast pressure wave consists of a compression shock front followed by a rarefaction (expansion) wave as shown in Figure 1.2 [Kingery and Bulmash 1984, Briassulis 2001, TM 5-1300 1990]. The duration of the shock and the compression wave are typically in the order of 10^{-6} s and are 10^{3} times larger than those associated with the expansion wave [Kingery and Bulmash 1984]. The response of a structural element subjected to a blast wave evolves with time; there are several time-scales in the blast response of the structural element as shown in Figure 1.2. In the very short time frame (in the order of duration of the compression wave), the transient response is governed by the stress changes produced by wave propagation in the material. The strain rates in the order of 100 s^{-1} and higher are produced at the very short time scales. With time, the response of the structure evolves to produce vibration of the entire structural element at frequencies, which are determined by the stiffness of the element and the boundary conditions [TM 5-1300 1990; Conley and Gregory 1999 & 2000, Mosalam and Mosallam 2001]. The vibration response of the structural elements usually occurs in the milli-second time-scale and produces strain rates in the range of 0.1-1.0 s^{-1}. The vibration response might be completely absent in the case where complete failure or loss of integrity is produced by the high amplitude stress wave produced by shock front. In the short time scales, a large magnitude blast can result in significant damage and even brittle shattering in concrete or masonry leading to a collapse of the structural element [Davidson 2005, Hamoush et al. 2001, Conley and Gregory 1999 & 2000]. The failure of a few critical load-bearing structural elements may eventually lead to the progressive collapse of the entire structure [DTRA/TSWG Status Report 1999].

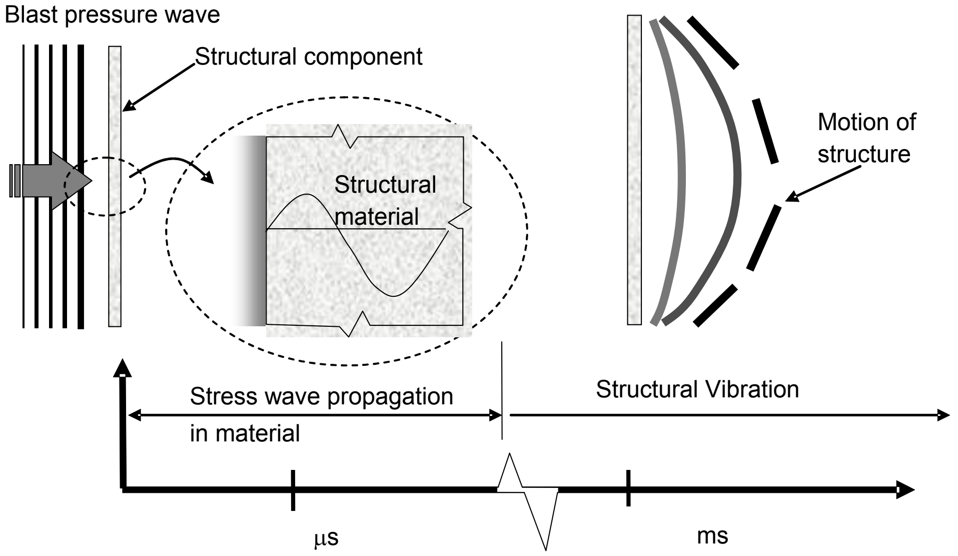

Figure 1.2: Time scales in the blast response of a structural element

Most of the blast mitigation strategies currently in practice for existing buildings and structures fall in the category of structural strengthening and/or restraint systems, which enhance the strength and continuity in critical elements. The use of fiber reinforced polymer (FRP) composites and pure polymeric systems comprising of thin layers of Polyurethane have recently been explored to retrofit existing concrete and masonry structures. These strengthening systems have been shown to increase the out-of-plane load resistance and stability, decrease deflections and generation of debris in concrete and/or masonry structural elements subjected to blast [Conley and Gregory 1999 & 2000; Davidson et al. 2005; Hamoush et al. 2001]. The blast retrofit measures, which rely on strengthening or hardening a structural element are only effective in the time frame associated with the structural motion (typically in the order of milli-seconds) of the structural element (shown in Figure 1.2). These systems do not directly influence the magnitude of the stress wave generated in the material (on the time scale associated with wave propagation in the material) when the blast wave is incident on the structural element. In the case of quasi-brittle materials, such as masonry and concrete, the high amplitude stress waves produced in the material can cause significant damage, well before the structure shows signs of deflection [Eamon et al. 2004]. There is hence a need to develop protective systems for structural elements, which decrease the amplitude of the blast pressure experienced by the material of the structural element. Such protective systems can then be used in conjunction with strengthening systems for developing effective blast mitigation strategies.

Protective material systems which use porous metal foams for attenuating an incoming blast wave are being researched for specialized applications [Cooper et. al. 1991, Guruprasad and Mukherjee 2000a and b; Hanssen et al. 2002]. Applications based on metal foams are however impractical for infrastructure applications because of the cost involved. Material systems for use in Civil Engineering applications, which provide for energy dissipation of the blast wave prior to impacting the structural element are either under development or currently unavailable. Some of the challenges, which have limited the research in this area, are:

1. Blast loading is of a very transient nature and is imposed on the structure in the form of a pressure wave. A complete understanding of the shock wave-structure interaction requires a multi-disciplinary approach that combines both solid and fluid mechanics, and

2. Research into the blast is often hampered by difficulties and risks associated with conducting such experiments. Uncontrolled blast sources (such as explosive charges) have been used, which besides being dangerous, do not allow for obtaining parameters for developing material models [Conley and Gregory 1999 and 2000, Davidson 2005].

The work presented in this dissertation is aimed at researching the concept of a protective system for structural elements consisting of compressible, low-strength, cementitious material, which will provide dissipation of incident blast wave energy (as shown in Figure 1.3). A porous, low-strength cementitious material,[1] with low impedance (resistance) to shock wave propagation is proposed to achieve energy dissipation through irreversible compaction of the material. This damage mechanism in the porous material provides for energy dissipation and hence an attenuation of the incident blast wave. The foam cladding is intended for use as a sacrificial protective material, which would reduce the stress amplitude transmitted to the structural element from an applied blast pressure loading. Brittle shattering or spalling of structural elements, primarily made of reinforced concrete or brick masonry, could be prevented or suppressed in cement foam cladded structures. The low-strength material, once developed, can be used in conjunction with existing structural strengthening systems such as externally bonded polymer laminates to develop effective blast mitigation strategies.

---

[1] Porous cementitious material implies a material with a cementitious matrix which contains entrained porosity. Entrained porosity is introduced by the addition of air bubbles or other inclusions.

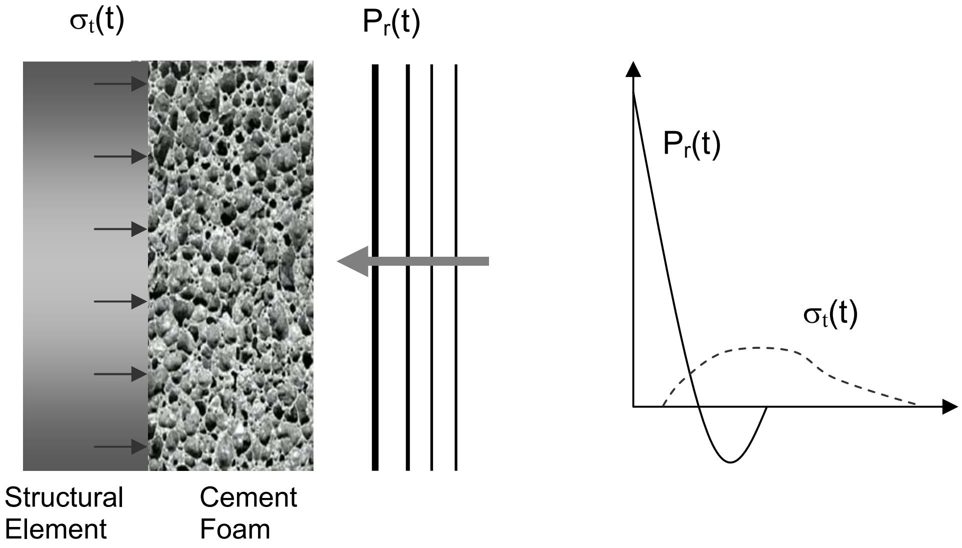

Figure 1.3: Schematic illustration of the proposed blast mitigation strategy.

1.2. Outline of Work

Development of effective protective strategies using low-strength cementitious foams requires an integrated approach involving: (a) Development of an understanding of the dynamic response of foam subjected to transient loading from blast; (b) Modeling the response and developing calibrated predictive capability; and (c) Developing practical guidelines for incorporating cement foams in a protective scheme for structural elements. A broad outline of the work presented in this dissertation is as follows:

1. A test setup required for generating and measuring blast pressure waves is developed and used to investigate dynamic response of cementitious foams.
2. Theoretical framework and numerical procedures for predicting the dynamic response of blast loaded cement foam and account for the irreversible densification

of material induced by a well-defined compaction front, which exhibits shock-type characteristics are developed and calibrated with the experimental data.

3. A design guideline for using cement foam in a protective design against blast loading is developed using the information from experimental investigation and the theoretical development. Two damage mechanisms in the two time scale associated with wave propagations and structural motion are considered.

1.3. Organization of the Dissertation

The dissertation is organized in six chapters. Each of these chapters deals with separate but inherently integrated tasks. The outline of this dissertation is as follows:

Chapter 2 gives a detailed review of literature relevant to current research, including experimental approaches, theoretical modeling and numerical methods used to study the dynamic response of the foam under high velocity impact, shock and blast loadings.

Chapter 3 presents a one-dimensional ‘shock’ model for predicting the dynamic response of foams subjected to transient loading associated with a shock front. A numerical implementation considering fluid-structure interaction (FSI) between an air blast and foam is developed for modeling the dynamic compaction of foam. In the numerical implementation, the domain for the air medium with the boundary represented by the edge of the porous solid is developed within an arbitrary Lagrangian-Eulerian (ALE) framework. A coupling algorithm based on enforcement of congruence conditions and simultaneous integration of fluid and solid equations is presented. The evolution of energy dissipation associated with the dynamic compaction of foam is explored.

Chapter 4 presents the development of a numerical scheme for predicting the dynamic compaction of foams associated with cell collapse under conditions of one-dimensional strain. Finite volume implementation of the hyperbolic conservation equations in the Lagrangian framework capable of predicting the propagation of an elastic wave and a compaction front which exhibits shock-type characteristics in such materials is described. The solution to the local Riemann problem is developed considering the possible wave structure(s) and used in implementing a finite volume scheme based on the second order Godunov method for determining the propagation of a stress waves and compaction front in foams. The numerical solution for predicting the dynamic compaction response of the foams subjected to solid impact and air blast loading is presented. The attenuation of transmitted stress achieved by compaction of foam for incident blast pressure waves is illustrated.

Chapter 5 presents the experimental investigation of the one-dimensional dynamic response of cement foams subjected to blast pressure loading. The experimental setup for generating blast pressure waves of given duration and amplitude is described. Instrumentation for measuring the applied and the transmitted stresses are detailed. Experimental results from cement foams of different densities and different lengths subjected to different blast pressure loadings are presented. The numerical methods developed in Chapter 3 and 4, the shock model and the exact Riemann based finite volume method, are calibrated with the experimental results.

Chapter 6 aims to develop a design guideline for using foam in a protective strategy for a prescribed level of projected threat from a blast. A two-step design approach, which considers damage mechanisms in two time scales associated with stress wave propagation and structural motion, is developed. Finally, a design example is presented and the effect of foam in increasing the resistance of a structural element again blast loads in both time scales is clearly illustrated on a pressure-impulse (p-i) diagram.

Chapter 2: Literature Review

2.1. Introduction

Foam is an important class of lightweight cellular engineering materials. An interconnected network of solid struts or plates, form the edges and the faces of the basic elements of foam, called cells. Foam is usually categorized based on the property of its solid component, as elastic, plastic or brittle foam [Gibson and Ashby 1999]. If the solid of which the foam is made is contained in the cell edges only (so that the cells connect though open faces), the foam is said to be open-celled; otherwise, if the faces are solid too, so that each cell is sealed off from its neighbors, it is called be closed-celled [Gibson and Ashby 1999].

Studies and successful applications of foams in applications involving transient loading have received considerable attention and significant progress has been achieved in developing practical applications. The transient dynamic loadings applied on the foams can be classified as blast loading, shock loading and impact loading depending upon the source of applied stress. Blast and shock loading involve pressure applied from a fluid medium such as air or water. Both blast and shock involve an abrupt pressure rise associated with a shock front and differ in the pressure history following the shock. Impact loading on the other hand involves stress applied by the impact of a solid impactor.

The advantage of using various metal foams to reduce the maximum transmitted loading due to an impact has been supported by experimental and theoretical research and practical applications such as improving crash worthiness, packing and automobile impact have successfully been developed [see Ashby and Gibson 1999 for a review]. Blast mitigation using foam is however an emerging field and there is limited data on the blast response of foams available in the literature. The idea of using aluminum foam as a protection for blast loading has only been briefly mentioned in the design handbook for metal foams [Hutchinson et al. 2000]. A clear understanding of the dynamic response foam and the beneficial effects of using foam in application involving blast are still emerging.

Foams subjected to dynamic loading evoke transient dynamic response, which depends upon the pore structure and the material of the foam. In open celled foams, the dynamic response involves the transport of air in the voids surrounded by the solid matrix and the deformation of solid matrix. In closed celled foams on the other hand, the contribution of the disconnected fluid phase to the applied pressure loading is insignificant. In both cases, the transient dynamic load generates stress waves propagating in the foam and produces deformation of the solid skeletal frame. When the transient load is intensive, it produces significant deformation of the frame and lead to a collapse of the microstructure for brittle and plastic foams. The crushing of the foam produces an irreversible compaction of the material. The nonlinearities associated with the material deformation and fluid flow within the pores of the foam pose significant challenges in modeling the dynamic response of foams subjected to transient loading. The significant experimental and modeling of foams are summarized in the next few sections. A review of the available experimental works associated with the dynamic response of various foams subjected to these dynamic loadings is presented in section 2.1. The analytical and numerical methods developed for modeling the dynamic response of foams subjected to shock, blast and impact loads are reviewed in section 2.2.

2.2. Experimental Investigation of Dynamic Response of Foams

In this section the available information from the dynamic tests of foams under the aforementioned three types of transient loads, i.e. shock wave, impact and blast wave loads, is reviewed. The available experimental data is categorized and presented as: a). low-density electrometric foams under shock loading; b) rigid metal foams under shock loading; c) metal foams under impact loading; and d) metal foams under blast loading.

2.2.1. Low-density Electrometric Foams under Shock Loading

Interaction of a shock wave with flexible porous material was first reported by Monti [1970]. The work focused on the strength of a planar shock wave reflected off the front face of the porous material. An analytically framework for shock wave interaction with a deformable material was also presented. The results indicated that the transferred pressure at back wall through the foam could exceed the pressure magnitude obtained from reflection of the shock wave off of a stationary rigid wall.

Gvozdeva et al. [1985] conducted shock tube tests on high porosity, polyurethane foam (porosity =97%) of different lengths. The pressure generated at the back end of the foam was found to be higher than the pressure generated by the incident shock wave reflected directly from the back wall without the foam. The peak pressure was found to increase with an increase in the initial length of the foam. The pressure enhancement produced by the foam was found to reach an asymptotic value as the initial length of the foam was increased.

Similar shock tube experiments indicating pressure amplification were also reported by skews et al. [1993]. Two open-celled, compressible, polyether foams were tested. Piezoelectric pressure transducers were used to record the pressure before, alongside and behind the foam specimen. A reduction in reflected shock wave strength and a substantial increase in the back wall pressure compared to rigid wall reflection, found by other workers, were confirmed. In addition, Schlieren photographs showed a flow of gas across the face of the foam during the interaction. Photographs of the deformation of the foam were used to study wave propagation in the solid skeleton. It was established that the compaction wave front in the solid skeleton travels at a considerably lower velocity (about 90m/s) than the wave speed in the gas as detected by the pressure transducer along the foam (about 200m/s). The results indicated that an open celled foam behave like two phase medium and not as a homogenous one-phase material. A simple physical model based on a zone of compacted material in the foam acting as a high-resistance flow barrier, was proposed to explain the observed phenomena. Similar experiments on the shock wave interaction with low-density, flexible foam and pressure enhancement were also conducted by Ben-Dor et al. [1994], where open cell polyurethane foam of density 31.5kg/m^3 and porosity of 0.97 was used.

The available experimental evidence clearly indicates that low-density flexible polymeric foams result in pressure enhancement when subjected to shock loading. It should be noted that the all the results in the literature were obtained for shock loading where a shock front is followed by constant pressure of infinite duration. Such loading is associated with an infinite impulse and energy input. Loading associated with a blast pressure wave, however, has a decaying profile which follows the sudden pressure rise produced by the shock front. Blast pressure loading is of finite duration associated with finite impulse input. Therefore extension of the findings from shock loading to the case of transient loadings with finite impulse is not yet clear.

2.2.2. Rigid Metal Foams under Shock Loading

The head-on collision of a planar shock wave with an open-celled, rigid porous material was investigated experimentally by Levy et al. [1993]. Experiments with the use of metallic (Alumina matrix) and brittle (Silicon Carbide matrix) foams were confined to the studying the interaction at shock pressure amplitudes which do not produce significant deformation of the solid skeleton. This study was limited to understanding the change in the characteristics of the pressure wave upon transmission through the porous matrix. The measured pressure history suggested that the shock wave breaks down and develops a dispersed wave structure in the foam. Further, the pressure recorded at the end wall indicated a continuous increase, which finally reached an asymptotic value slightly higher than the pressure corresponding to the reflection off a stationary rigid wall. The final pressure value of the pressure was found to increase with an increase in the porosity of the foam. These experimental results were later used for calibrating the numerical model [Levy et al. 1996a] and the analytical models [Levy et al. 1996b] for studying the shock wave-rigid foam interaction.

2.2.3. Metal Foams under Impact Loading

The dynamic response of the metal foams and the energy-absorbing characteristics due to an impact loading has been experimentally studied by many researchers [Reid and

Peng 1997, Tan et al. 2005a; Lopatnikov et al. 2003; Nemat-Nasser 2007]. The reason for this interest is because of the capacity of these materials to absorb the energy from various forms of impacts. Gibson and Ashby [1999] have devoted a chapter of their book to the selection of materials for low speed impact applications. Under high speed impact, the material experiences deformation at high strain rates. Experimental results indicate a dramatic change in the deformation behavior at high speed impact, characterized by a more localized deformation in the foam, rather than a more uniform deformation typically observed in low velocity impact [Tan et al. 2005a]. The localized deformation is associated with a traveling compaction front in the foam, which has the characteristics of a shock wave.

The two commonly used experimental techniques for studying the high-rate testing of metal foams are the compression split Hopkinson pressure bar (SHPB) and the direct-impact test. Both techniques utilize strain-gauged, cylindrical pressure bar(s) for measuring stress (or, more correctly, strain) wave pulses generated by an impact. The split Hopkinson pressure bar (SHPB) technique was originally proposed by Kolsky [1949] as a means of determining the stress versus strain relationship of materials at high strain rates. In the test setup, the loading pulse is generated by the impact of a striker bar, which is accelerated to a prescribed impact velocity by a high-pressure air gun. A compressive stress wave propagates from the impacted end of the incident bar towards the specimen, which is placed between the incident bar and the transmitter bar. The specimen is subjected to an incident pressure pulse of approximately constant amplitude and duration, which is proportional to the length of the striker bar. The amplitude of the incident pulse is directly proportional to the impact velocity, which can be controlled by adjusting the pressure of the air gun. The strain pulses recorded from the incident and transmitter pressure bars are used to determine the stress versus strain response of the specimen at high strain rate. Testing of acoustically soft materials, such as foam, rubber and clay, using a traditional steel bar faces difficulties of poor transmission to the transmitter bar. Use of aluminum and PMMA bars are common in the measurement of transmitted stress for soft materials [Chen et al. 1999; 2000].

In the direct impact test, the specimen is fired from a gas gun onto the end of a strain-gauged transmitter bar. The contact stress between the specimen and the transmitter bar and the average strain response are measured. The velocity of the specimen immediately prior to impact is measured by timing the passage of the specimen between two narrow light beams. Sometimes a backing mass is attached to the back face of the specimen in order to provide additional kinetic energy and to improve the alignment of the specimen within the barrel of the gun. If a large backing mass is used, the kinetic energy of the striker at impact is much greater than the energy required to compact the foam. The velocity of the striker is assumed to be constant during the crushing of the foam and used to calculate the average strain accumulated within the specimen [Deshpande and Fleck 2000].

Direct impact tests were carried out to study the dynamic response of wood foam at high rates of loading by Reid and Peng [1997]. Cylindrical wood specimens without a backing mass were fired directly on to a strain-gauged transmitter bar at impact velocities ranging between 30 and 300 m/s. Stress reading on the transmitter bar showed that significant enhancements of the initial crushing strengths of the specimens occur under dynamic loading conditions and the enhancement increases with increasing impact velocity. At high impact velocity, the deformation of the foam was localized and a discontinuity wave propagated through the material in the form of a crushing front, which has some of the characteristics of a shock wave. The enhancement of the crushing stress was attributed primarily to a planar discontinuity wave propagating through the cellular material. The discontinuity wave was referred to as the compaction wave and it separates the compacted material from the uncrushed foam.

Similar experimental studies using the direct impact technique were performed subsequently by many researchers for metal foams, especially aluminum foams [Tan et al. 2005a; Lopatnikov et al. 2003; Nemat-Nasser 2007]. Tan et al. [2005a] studied the dynamic compressive behavior of closed-cell Hydro/Cymat aluminum alloy foams with two different average cell sizes (diameters) of approximately 4 and 14 mm at a range of impact velocities from 10 to 210m/s. An aluminum backing mass was attached to the rear (distal) end of each specimen. The study confirmed the formation of localized crushing front which propagates in the material in the form of a compaction front when the impact velocity exceeded a critical value. At sub-critical velocity, the deformation pattern was observed to be similar to quasi-static loading. Overall shortening of the specimen, in the low velocity regime, is achieved by the accumulation of discrete, non-contiguous bands of crushed cells. However, beyond the critical impact velocity of approximately 42 ms^{-1} for large celled specimens and 108 ms^{-1} for the small celled specimens, cell crushing occurred sequentially, in a planar manner, along the axis of the specimen. The crushing initiated from the impact-end and the crushing wave front exhibited ‘shock-type’ characteristics as shown in Figure 2.1 (a). Such a phenomenon was also clearly evident in the scanning electron micrograph of the metal foam specimen after impact by Radford et al. [2005] (Figure 2.1 (b)). The micrograph clearly shows a sharp compression front, which separates the compressed and un-deformed regions of the foam.

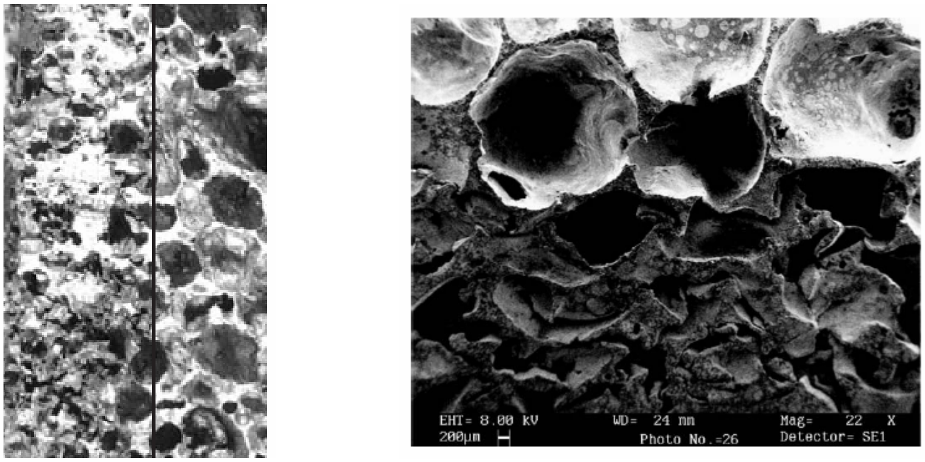

(a) (b)

Figure 2.1: Experimental evidences showing a sharp compaction front under high-velocity impacts cited from (a) Tan et al. [2005a] and (b) Radford et al. [2005].

The dynamic response of aluminum foam with an average density of 0.37 g/cm^3 and strength of 4 MPa was tested using the Taylor cylinder–Hopkinson bar impact setup (the same as direct impact test) by Lopatnikov et al. [2003]. An ultra-light, polymeric foam of negligible mass, was attached to the back of the specimen to guide the foam sample in the gas gun and provided a planar impact. The impact velocities were in the range 20–200 m/s. At an impact velocity of 26 m/s, no shock front appeared and the specimen was almost undeformed. At an impact velocity of 79 m/s, about half of the specimen was densified, and the shock front was clearly visible. At an impact velocity of 200 m/s, the foam specimen completely collapsed.

The dynamic response of a sandwich structure to impulsive loads was experimentally investigated by Nemat-Nasser et al. [2007] for potential use in mitigating impulse loads. The sandwich structure had a metal foam core and metal cover plates. The Duocel aluminum foam made from Aluminum with 8–10% nominal density was used in the tests. The dynamic response of each component was tested and characterized independently. The energy-absorbing characteristics of the core material in a sandwich structure were studied using the modified SHPB technique, where the incident bar was removed and a short projectile directly impacted on the aluminum foam specimen. Results from two different impact velocities equal to 30 and 55 m/s were reported. For the smaller impact velocity, large deformations are initiated first at the far end of the specimen, whereas for the larger impact velocity, large deformations initiated near the impact zone. Finally, the dynamic behavior of sandwich panels composed of front and back plate and foam cord, under a blast loading was analyzed by finite-element simulations. It is found explosion energy can be almost absorbed by the deformation of front plate and core if the sandwich panel was effectively design. The back plate experienced a much smaller deformation than that of the front plate.

The experimental results on the use of metallic foams obtained from studies involving impact have shown the benefit of using foam for providing energy dissipation [Reid and Peng 1997; Tan et al. 2005a; Lopatnikov et al. 2003; Nemat-Nasser 2007]. It should however be noted that there is a fundamental difference in the nature of loading associated with impact and blast pressure. In an impact, the energy delivered to the system associated with a projectile traveling at a given velocity is a fixed value but the stress transmitted at the interface can vary depending on the materials in contact. Whereas for blast, the loading history produced by a same incident blast wave at different solid substrate is always the same (if neglecting the effect of the fluid solid interaction) but the energy transferred to the solid substrate varies depending upon the stiffness of the substrate (larger for softer material).

2.2.4. Foams under Blast Loading

Experiments conducted on foam or foam like structures subjected to blast load are limited to a few investigations. Free-field experiments on layered sacrificial claddings subjected to blast loading were carried out by Guruprasad and Mukherjee [2000b]. The cellular construction of the claddings and the experimental set-up are shown in Figure 2.2. Blast pressure loading was generated from the explosion generated by a TNT charge. The test results indicated a progressively decreasing level of damage in the successive layers. While the first layer completely collapsed, the second layer exhibited partial collapse of the structure and the third layer had undergone marginal plastic deformations. The results suggested that the top layers of the structure undergo plastic deformations and reduce the energy transmitted to subsequent layers, thus protects the structure underneath. The experimental results indicate the layered sacrificial claddings as an effective energy absorbing device for design of structures under blast loads.

Figure 2.2: Photograph of layered sacrificial claddings and the experimental set-up by Guruprasad and Mukherjee [2000b].

Experimental results on the blast response of aluminum foam panels as sacrificial layers subjected to blast loading were presented by Hanssen et al. [2002]. A pendulum test set-up was used as shown in Figure 2.3. In this test set-up, foam panels (with and without solid covers attached to the outer face) were attached to the bob (strike face) of the pendulum. The explosive charge was located at a given standoff distance in front of the pendulum's bob. When the charge detonated, the blast loading accelerated the bob of the pendulum and the maximum swing angle was measured. The maximum swing angle of the ballistic pendulum was used to determine the energy and impulse transfer from the blast loading. The results showed that the addition of the foam panels significantly increased the energy and impulse transfer to the pendulum. The counter-intuitive behavior was attributed to the geometric effect associated with the continuous change of shape of the initially plane panel surface into a double-curved shape. In the experiments, the applied blast pressure and the pressure transmitted to the substrate were not measured directly. The pressures were inferred indirectly using numerical simulations and it was found that the bob experiences a reduced pressure level compared to the blast loading pressure. Hanssen et al. [2002] proposed that the collapse load of the sacrificial layer when kept below the minimum elastic capacity of the main structure could prevent the explosion not to damage the main structure.

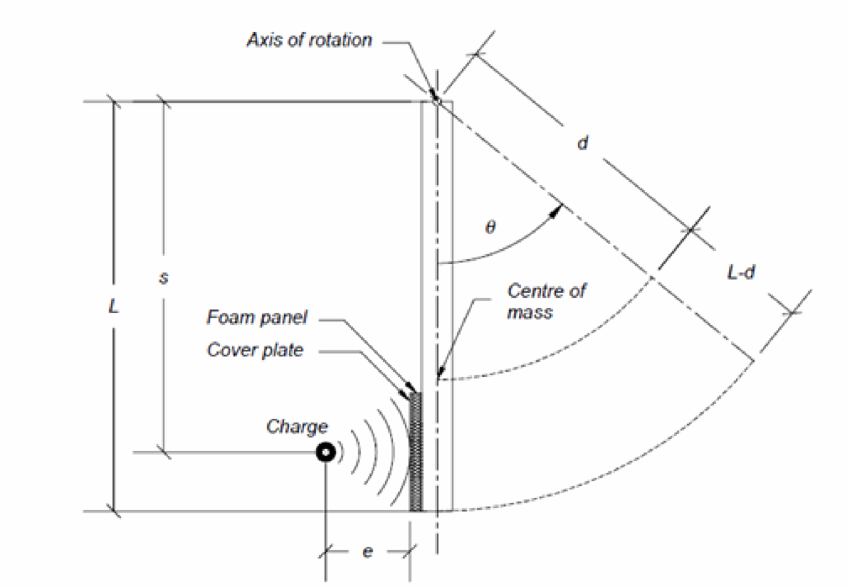

Figure 2.3: Schematic of the pendulum test set-up by Hanssen et al. [2002].

The above blast experimental results contain contradictory indications as to the benefit of foam or foam like material in mitigating blast loading. The experimental results of Guruprasad and Mukherjee [2000b] suggests a benefit of using cellular materials composed of layered sacrificial claddings in effectively absorbing the blast energy. The experimental results of Hanssen et al. [2002], on the other hand, showed a disadvantage of foam because the addition of the aluminum foam panels significantly increased the energy and impulse transfer to the pendulum. However, unlike the case of solid impactor, the energy input associated with a blast loading is not fixed. When the attached foam ‘absorbs’ a large amount of energy, the more flexible material also increases the energy inputted to the system because it results in a larger displacement on the loading path/face. It is therefore point out that ‘absorbing the energy’ should not be the judgment for benefit of using foam in blast mitigation, which actually may leads to confusion in this application. It is claimed in the current study that the benefit of foam is to reduce the magnitude of the peak stress transferred through foams to the solid substrates rather than reducing the energy (or impulse). However the actual transmitted stress through the protective material is missing in both experiments.

2.2.5. Summary of Experimental Results

The information available from the different studies is inconsistent with regard to the protective effect of foam. While the benefit of using a porous material in reducing the maximum transmitted stress associated with impact loading has been demonstrated, experimental evidence regarding the performance of foams subjected to shock loading is inconsistent. Shock wave loading on the low-density electrometric foams suggests the possibility of stress enhancement. Clear experimental evidence showing the protective effect of foam under applied blast pressure loading is currently not available.

In conclusion, both the successful use of foam in mitigating impact [Reid and Peng 1997, Tan et al. 2005a; Lopatnikov et al. 2003; Nemat-Nasser 2007] and the available information on the pressure enhancement caused by the flexible foams associated with shock loading [Monti 1970, Gvozdeva 1985, Skews 1993, Ben-Dor 1994] do not provide sufficient indication as to the application of foam in mitigating blast loading. The blast test results available in the literature [Guruprasad and Mukherjee 2000b and Hanssen et al. 2002] are also not helpful since the stress transmitted from the foam to the solid substrate were not measured, which is the key to understand the behavior of foam in blast mitigation. Careful experiments on blast response of foams obtained from experiments with well defined input blast pressure wave and an accrete measurement of transmitted stress, which would lead to a fundamental understanding of the behavior of foam, are currently not available.

2.3. Modeling the Dynamic Response of Foams

Due to the inherent heterogeneously, the diversity in the type of material and the pore structure of the foams and depending on the interests in their applications associated with dynamic loadings, different approaches for modeling the dynamic response of foam have been employed. For instance, metal foams are widely used as protective materials in packaging and automobile industries for improving crash worthiness. In modeling the dynamic compaction of the metal foam during impact, the bulk stress-strain relationship of the solid matrix is usually employed, where the actual two phase material is modeled as a homogeneous solid material without any voids [Gibson and Ashby [1999]. Another example is the response of an open-celled foam subjected to a shock wave [Bear and Bachmat [1990]]. In this case, the approach involves formulating the balance equations for each phase of the air-saturated foam with a focus on giving a detailed description of the motion of each phase including the deformation of solid matrix, the motion of air flux inside the connected pores, as well as the interaction of two phases. These models for the dynamic response of foam are categorized into two groups: a) one-phase approach; and b) the two-phase approach. The applications, limitations of these approaches and the relation to the current research are also included.

2.3.1. One-phase Approach

In one-phase approach, the foam is treated as fictitious one-component homogenous material. The mechanical and thermal properties of the fictitious material, such as strain, stress, particle velocity, temperature and etc, are defined as bulk quantities of both phases comprising the foam. The solids and gaseous phases have the same motion and the interaction between two phases is ignored. The classical conservation equations of a continuum are used for modeling the dynamic response of foam subjected to various dynamic loads. The conservation equations combined with a specific material model described in terms of the bulk properties of the fictitious one-phase material constitute a set of closed non-linear hyperbolic equations, which describes the motion of the continuum.

In the following, three popular one-phase approaches, the pseudo gas approach [Olim et al. 1994; Li and Ben-Dor 1995], the bulk approach [Gibson and Ashby 1999] and the idealized shock model [Reid and Peng 1997; Harrigan et al. 1999; Tan et al. 2005b; Hanssen et al. 2002] are reviewed. The pseudo gas approach has been used to treat the response of weak foam with extremely low density, which is treated as a homogeneous pseudo-gas. The bulk approach has been widely accepted for modeling the high-speed impact of metal foams. The idealized shock model is a special case of the bulk approach, where the bulk strain-stress relationship of foam is further simplified.

2.3.1.1. The Pseudo Gas Approach for Low-density Foams

The pseudo-gas approach has been used by several researches to model the response of a weak foam subjected to head-on impact by a shock wave. The properties of the pseudo gas are derived as a function of the properties of air and the solid matrix and the porosity of the foam. The foam is modeled using Euler equation with the equation of state (EOS) of the pseudo gas. The shock wave-weak foam interaction at the interface is treated using gas dynamic relations together with the pressure and velocity congruence conditions at the interface between air and the pseudo-gas.

The approach was used by researchers [Olim et al. 1994; Li and Ben-Dor 1995] to develop analytical models for computing the flow field in the vincinity of the interface between air and the foam at shock wave incidence. Li and Ben-Dor [1995] used simple wave relations and the Hugoniot relation in gas dynamics to determine the peak reflected pressure at the end-wall supporting the foam. The end-wall pressure is determined to be equal to the stagnation pressure of the transmitted shock wave induced flow field. The solution was compared to a series of shock tube experiments conducted by Skews et al. [1993], in which the interaction of weak planar shock waves with polymeric foam with extremely low-density around 30 g/cm^3 and high porosity around 98% was studied.

2.3.1.2. Bulk Approach for Metal Foams

The application of metal foam, such as Alcan, Alulight and Duocel aluminium alloy foam, have found applications in various fields as protective material against impact. The foam functions as a sacrificial material to absorb the kinetic energy of the impact through the large plastic deformation (compaction). The motion of the impactor is arrested and the peak force delivered to the solid substrate covered by foam is reduced. In modeling the dynamic compaction of the metal foam during the impact, a bulk approach is usually employed. In this approach, the deformation behavior of the foam is described in terms of the bulk stress and strain relations, which are measured as an average over a representative volume on the scale of the unit cell rather than the real stress or strain of the solid matrix. The two phase material is thus modeled as a homogeneous solid material with identical stress-strain behavior as the actual porous foam.

The constitutive model of foams, especially the aluminum foams, has been studied by many researchers. A review of this information is provided by Gibson and Ashby [1999]. Most foams exhibit a unique (bulk) stress-strain relationship under one dimensional quasi-static compression test, as shown in Figure 2.4. There are three distinct regions in a typical deformation curve, namely the linear elastic response, the crushing plateau and the densification region. At small strains, usually less than 5%, the behavior is linear elastic, with a slope equal to the Young modulus of the foam. As the load increases, the foam cells begin to collapse by elastic buckling, plastic yielding or brittle crushing, depending on the material of the cell walls. Collapse progresses at roughly constant load, giving a stress plateau, until the opposing walls in the cells meet and touch, when densification causes the stress to increase steeply and approach that of the intrinsic material.

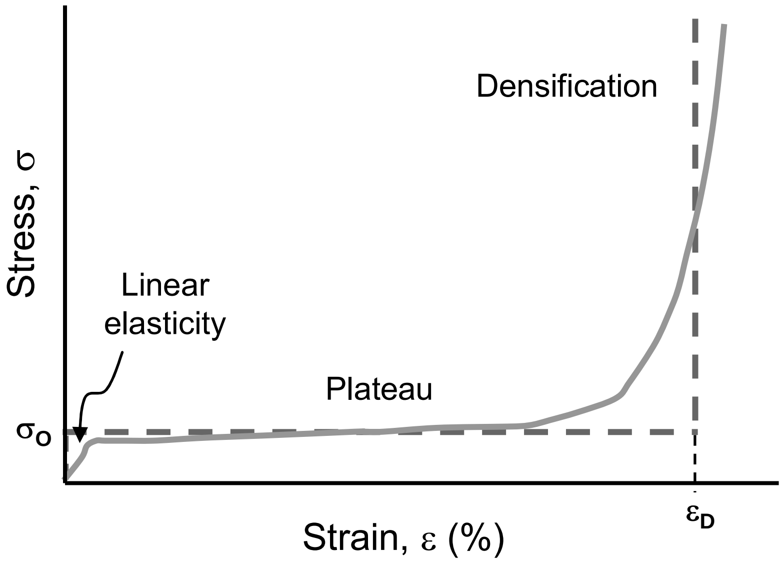

Figure 2.4: Schematic compressive engineering stress-engineering strain curve for foams (solid line) and RPPL idealization (dotted lines).

The strain-stress relationship shown in Figure 2.4 refers to the quasi-static deformation behavior of foams. The use of metal foams in various dynamic problems often requires an evaluation of the strain rate effect on their compressive behavior. The strain rate effect has been studied for the different types of aluminum alloy foam (Alcan, Alulight, Doucel etc.), which is a major metal foam used in practice. There is growing evidence showing that the metal foam is insensitive to applied strain rate. Kenny [1996] reported that the specific energy absorption of Alcan foam was independent of applied strain rate in the range 10^{-3}-10^{3} s^{-1}. More recently, the high strain rate compressive behavior of Alulight and Duocel was investigated using the split Hopkinson pressure bar and the direct impact tests [Deshpande and Fleck 2000]. Strain rates up to $5x10^{3}s^{-1}$ were employed, which are within the practical range for many applications of these materials. Over the range of nominal strain rates employed (10^{-3}-$5x10^{3}$ s^{-1}), no elevation of the dynamic stress versus strain curves was observed compared to the corresponding quasi-static curves and the plateau stress was almost insensitive to strain rate for strain rate. The three likely contributions to the rate-sensitivity of the material response of a cellular solid are: 1) entrapped air within the closed-cell foams; 2) strain rate sensitivity of the cell wall material which is dependent on thermal activation or dislocation drag processes; and 3) the micro-inertia of the individual cell walls. It was established through analysis that these contributions are negligibly small over the range of strain rates evaluated in most test programs.

In the bulk, one-phase approach, the constitutive relationship combined with the conservation equation of mass and momentum become the mathematical governing equation system for predicating the dynamic compaction of metal foams. The governing equation is a non-linear hyperbolic system, which admits the possibility of shock formation. In materials which exhibit concave stress-strain curve, the possibility of the formation of a strong discontinuity, which resembles a “shock” wave, has been established [Hopkins 1968, Morland 1959, Nowinski 1965]. The presence of a strong discontinuity in the solution field poses stringent requirements for any numerical scheme used to evaluate the transient dynamic response of foam. Most of numerical methods have difficulties in simulating shockwave propagation since oscillations are always observed behind the shock wave fronts. One of the common techniques to reduce the oscillations behind the shock wave fronts is artificial bulk viscosity [Xiao, 2004]. It can efficiently eliminate the oscillations but the shock wave fronts are observed to be spread over several elements or space step sizes if finite element or finite difference methods are used, respectively. The finite volume method of Godunov type is a modern shock capturing scheme of high-resolution and has been proven to be a powerful tool for systems of non-linear hyperbolic equations. The method was originally developed for compressible gas dynamics, to treat the Euler equations, in which the shock wave is part of the solution [Toro 1999]. Since Euler equations are nonlinear hyperbolic system, the extension of Govdunov method to general wave-propagation problems associated with different media is natural.

2.3.1.3. Simplified Model, RPPL

Recently, a one-dimensional 'shock' model based on an idealized stress-strain curve has been developed to analyze the dynamic response of metal foams and honeycombs under the impacts of solid objects [Reid and Peng 1997, Harrigan et al. 1999, Tan et al. 2005b] and air blasts [Hanssen et al. 2002]. The one-dimensional 'shock' model is a simplification to the one phase continuum approach resulting from simplifying assumptions. The typical material response is idealized as rigid, perfectly-plastic, locking (RPPL), as shown in Figure 2.4 by the dotted line. The second assumption relates to the deformation process of foam during an impact. Foam is compacted form zero strain to densification strain abruptly across a compaction front, the jump condition across which resembles the Rankine-Hugoniot relation of a shock wave. The compaction front initiates at the impact end and travels downstream. Considering these two assumptions and the locking state of strain in the material, the conservation of momentum is largely simplified and analytical solutions for the velocity of propagation of a finite disturbance, the motion of the compacted foam, the stress history transmitted to the supported end of the foam during the compaction of foam can be derived.

The shock model based on the RPPL idealization was first formulated by Reid and Peng [1997] for analyzing in the high-velocity crushing of wood foam. Harrigan et al. [1999] used the shock model to analyze the dynamic crushing of aluminum honeycombs.

Hassen [2002] studied the blast response of aluminum foam panels as sacrificial layers subjected to blast loading and adopted the shock model to predict the deformation behavior of a one-dimensional foam bar subjected to a linearly decaying blast loading. The shock model was also used by Tan et al. [2005a and 2005b] for studying the dynamic compressive response of the foam of closed-cell Hydro/Cymat aluminum alloy foams. The one-dimensional 'steady-shock' model based on RPPL idealization of the quasi-static stress-strain curves for aluminum foams were formulated using a thermo-mechanical approach. A kinematics existence condition for 'shock' propagation in aluminum foams was established using thermodynamics arguments and its predictions compare well with the experimental data.

Recently, a new shock model based on elastic-perfectly-plastic-rigid (EPPL) was developed by Lopatnikov et al. [2003, 2004]. In EPPL idealization, the initial linear elastic response of foam was accounted for, which results in an elastic precursor running ahead of the compaction. The analytical solutions using the new shock model were found to be in good agreement with the results obtained from the high velocity impact tests to the metal foam. In particular, results showed that the predicted change in length of foam specimens is in good agreement with the experiments [Lopatnikov et al. 2004].

The one-phase shock model has several shortcomings. First, in the shock model, the strain and the density in the densified material are equal to the values predicted by the idealized plastic locking response, regardless of the strength of the compaction front and the severity of the impact. Therefore, the foam is either intact or fully compacted and there is no intermediate value. In reality, the density of the compacted foam depends upon the strength of the compaction front. Second, the shock model only allows the foam to be compressed by the compaction front. However continuous compression stress waves may also develop in the foam considering different loading characteristics, leading to material compression in a continuous manner. Third, the solution procedure of the shock model is implicitly limited to the case when the length of foam is sufficient to completely arrest an impactor (or completely absorb the kinetic energy of the impact). The shock model is incapable of dealing with cases where the length of the foam is insufficient to completely absorb the energy of impact. In conclusion, the shock model largely simplifies the real situations using the RPPL or EPPL idealizations of the actual strain-stress relation of the foam. However, it is simpler to use offers the advantage of analytical solutions.

2.3.2. Two-phase Approach

The different constituents of a solid foam, the solids matrix and fluid in the pore space, have different motions, different material properties and there is an interaction among the constituents due to their relative motions. The two-phase approach accounts for the different mechanical and the thermo mechanical behavior of each constituent and the interaction between the two phases. Continuum mechanics based relations are derived for each constituent. The early work of Biot's [1956] on compression waves propagation in saturated porous media was the first attempt to model the wave propagation in porous material. In this approach, microscopic representations of the phase balance equations are developed within the framework of the theory of mixtures.

A macroscopic description of the porous material, which involves a combination of the representative elementary volume (REV) concept and the mixture theory has also been developed. In the last three decade the macroscopic porous material theory in wave propagation has made decisive progress concerning the fundamentals of the theory and the development of mathematical models. The development of macroscopic balance equations for mass, momentum and energy was provided by Bear and Bachmat [1990]. The macroscopic quantities of the porous material are obtained by averaging microscopic quantities over the REV. The interaction between the two phases, which is associated with relative movement, is considered using parameters, which account for the micromechanical effects, such as tortuosity factor and Forchheimer term [Bear and Bachmat 1990, Levy et al. 1995]. The tortuosity factor was introduced in the conservation equations by Bear and Bachmat [1990], and it is physically associated with the directional cosines of the pore orientation, the hydraulic radius of the pore spaces, and the porosity. Levy et al. [1995] advanced the two phase macroscopic balance equation to include an additional Forchheimer term. Levy et al. [1995] showed that the Forchheimer term should be included as an additional macroscopic inertia term arising from the microscopic inertia exchange between the phases at the solid-fluid interface.

Predicting the dynamic response of foam using the macroscopic approach involves solving coupled non-linear hyperbolic equations requiring numerical solution. The full one-dimensional set of governing equations developed by Levy et al. [1995] were numerically solved by Levy et al. [1996a] for predicting the propagation of planar shock waves through gas-saturated elastic rigid porous materials. The governing equations of two phases are both stated in Eulerian coordinate and equation system was solved simultaneous. A total variation diminishing (TVD)-based 2nd order Godunov method, which was traditionally developed for classical gas dynamics, was extended to solve the governing equations containing three conservation equations for each phase. Good comparison between their numerical predictions and the experimental results were observed. The numerical investigation was restricted to the ‘rigid’ case, where the deformation of the solid skeleton is negligible. Subsequently, Levi-Hevroni [2002] extended the one dimensional formulation to more general elasto-plastic flexible porous materials, where the solid matrix is allowed extremely large deformations. A different numerical approach was developed to tackle the difficulty concerning large deformation of the solid matrix and compatibility of two phases. The governing equations of the gaseous and solid phase were treated separately. The governing equations of the gaseous phase were formulated in an Eulerian framework and solved using the upwind TVD shock-capturing scheme. The governing equations of the solid phase were solved using the Arbitrary Lagrangian Eulerian (ALE) method, the classical version of which can be found in Hint et al. [1974] and Chan [1975]. The numerical solution is compared to the experimental results of Skews et al. [1993] for the case of the head-on interaction of planar shock waves with elasto-plastic flexible porous materials (i.e. large deformations). However, as was noted by Levi-Hevroni [2002] the comparison between the numerical and the experimental results was only qualitative, since the geometrical coefficients associated with the porous medium, namely the tortuosity factor and the Forchheimer coefficients, are not available in the literature.

The two phase approach implicitly assumes the porous material to be open-celled and therefore not directly applicable to closed cell foams. The two-phase approach may not suitable for modeling the dynamic compaction of foam where compaction of material is associated with cell collapse and irreversible compaction. As was mentioned above, some of the internal parameters such as tortuosity factor and the Forchheimer coefficients that reflect the internal microstructure of the material cannot not readily be determined experimentally. Further, as the internal microstructure of the material would change dramatically during the compaction, it would result in a significant change of the geometrical coefficients during the loading. The relation of these geometrical coefficients to the deformation of porous material cannot be predicted. Further, under the impact of a large impact or blast load, the compaction and the associated cell collapse would clog the interconnected channel of the open-celled porous material, which would prevent flux of air inside the material.

2.4. Conclusions

In conclusion, although a large number of studies has been conducted in many aspects of porous material, strategies that provide effective means of mitigating the influence of blast are either under development or currently unavailable. Moreover, experimental evidence on the energy absorption and force transmission in porous material indicated the possible fore enhancement in practical applications. These uncertainties are yet to be clarified and a clear understanding of the behavior of foams under blast loading is still emerging.

Chapter 3: An Evaluation of the Dynamic Compaction of Foam under Air Blast Loading Considering Fluid-structure Interaction Effects

3.1. Introduction

Low-strength foams are typically achieved by entraining air in the material matrix; the strength of the porous material can be varied by varying the air content (or the porosity). Such foams typically exhibit a concave stress-strain relation, where an increase in the stress is achieved due to compaction of material. The compaction of the material is an irreversible localized phenomenon associated with the collapse of the microstructure leading to densification. The densification of the material is associated with crushing of cells and the overall decrease in strain is associated with accumulation of non-contiguous band of crushed cells. Eventually, the modulus of the porous material approaches that of the parent material when complete compaction is achieved (Ashby and Gibson 1999). Early work of Nowinski showed that dynamic loading of materials which have a concave stress-strain relationship results in the formation of a strong discontinuity associated with a shock (1969).

When foams exhibiting a concave stress-strain relation, which is associated with local cell collapse, are subjected to loading at rates exceeding a critical velocity, a planar compaction front associated with sequential collapse of cells results (Tan et al. 2005a.). The compaction front, which is associated with a strong discontinuity, has been shown to possess shock-like characteristics. A one-dimensional 'shock' model based on an idealized stress-strain curve for such materials has been developed to analyze the dynamic response of different foams and honeycombs under the impacts of solid objects (Tan et al. 2005a and b, Reid and Peng 1997) as well as an air blast (Hanssen et al. 2002). The material response is idealized using the rigid, perfectly-plastic, locking (RPPL) model, which is shown in Figure 3.1. When the real strain-stress curve is idealized using the RPPL model, simplified solution procedures can be developed for predicting the formation of a compaction front (shock) in such materials. The jump conditions across the compaction front are largely simplified due to the locked state of the strain in the material after compaction. Analytical solution for predicting the velocity of propagation of a finite disturbance in such a medium can also be derived.

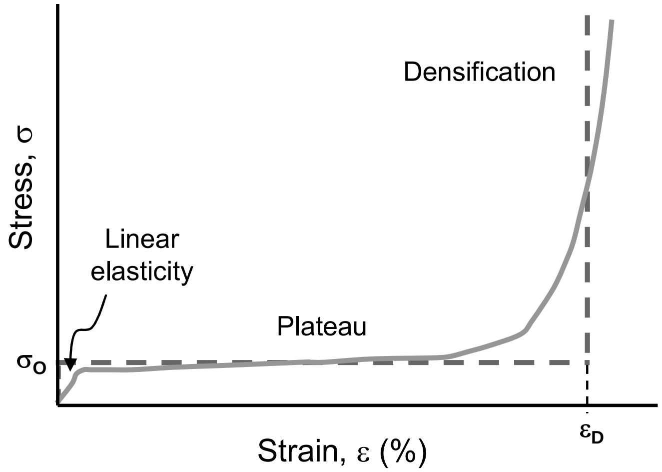

Figure 3.1: Typical compressive stress-strain curve for foams and RPPL idealization (dotted lines)

While some experimental data is available on the interaction of a shock wave with cellular and rigid porous materials (Skews et al. 1993, Ben Dor et al. 1994, Levy et al. 1993, Standley et al. 2002), very limited data is currently available on the dynamic compaction of low strength foams produced by a blast pressure wave in air (Hanssen et al. 2002). Results of Hanssen et al. (2002) using Aluminum foams show that there is an increase in the energy transferred from a blast pressure wave to a structure. The results of this investigation appear to be counter-intuitive since foam is usually assumed to decrease the energy transferred to the structure by dissipating energy in its crushing. The results from the foams are also counter to the results from sacrificial claddings where the collapse of layers was shown to contribute to dissipation of the blast pressure (Guruprasad and Mukherjee 2000a and b). A clear understanding of the energy absorption by a low-strength foam and dissipation provided by its irreversible compaction is currently not available.

Available literature shows that foams typically undergo large deformations under both quasi-static and dynamic loading (Mukai et al. 2005, Roberto 2005, Hanssen et al. 2002). The dynamic motion of the foam under pressure loading would also result in a large change in the fluid domain, thereby influencing the applied pressure. Changes in the applied pressure would directly influence the motion of the porous foam. It has been shown that the coupling effect could potentially influence the energy dissipation during the motion of a structure and it is particularly significant for compliant structures (Subramaniam et al. 2009). Therefore a proper study of irreversible dynamic compaction of foams requires a careful consideration of the fluid-structure interaction effects. The blast response of sandwich panels with core made of foams has been investigated considering FSI effect (Deshpande and Fleck 2005). The analysis however used the simplistic assumptions proposed by Taylor (1951), such as, no change in the fluid density and linear superposition of waves, which are acceptable for studying weak shock waves. Such an approach is however not suitable for studying the interaction of a strong shock wave in air blasts which involve non-linear, finite amplitude disturbances propagating in a compressible medium (Tan et al. 2005c).

In this paper, equations for one-dimensional dynamic compaction of low-strength foam idealized using the RPPL model are presented. A numerical implementation of the fluid-structure interaction in one-dimension during the dynamic compaction of foam is developed within an ALE framework. The compaction of the foam presents a moving boundary for the fluid, which influences the pressure adjacent to the face of the solid. In the numerical implementation, the fluid domain with the boundary represented by the edge of the porous solid is developed within the ALE framework. A coupling algorithm based on enforcement of congruence conditions and simultaneous integration of fluid and solid equations is presented. The numerical framework is used to investigate the interaction of blast pressure wave with foams.

3.2. Dynamic Compaction of Foam

One-dimensional equations for dynamic compaction of foam are developed in this section. The compressive behavior of foam is idealized using the RPPL model with a plateau-stress level of σ_0 and an engineering densification strain of ε_D, as shown in Figure 3.1. σ_O is also referred to as the strength of the foam. The initial foam density is ρ_f whereas the density after densification is ρ_{f0}. The foam bar has an initial length L_f. The main assumptions made in developing equations for dynamic compaction of foams considering the idealized RPPL material model are:

1. A compaction front forms and propagates in the foam[2].
2. The compaction front is infinite thin, and is treated as a strong discontinuity. After passing through the compaction front the material is compacted (densified).
3. Stress is σ_0 ahead of compaction front and jumps to a value equal to σ_D behind it
4. Strain is one-dimensional in the direction of motion of the compaction front. There are no lateral strains in the foam. The material is in a state of 1-D strain during the loading.

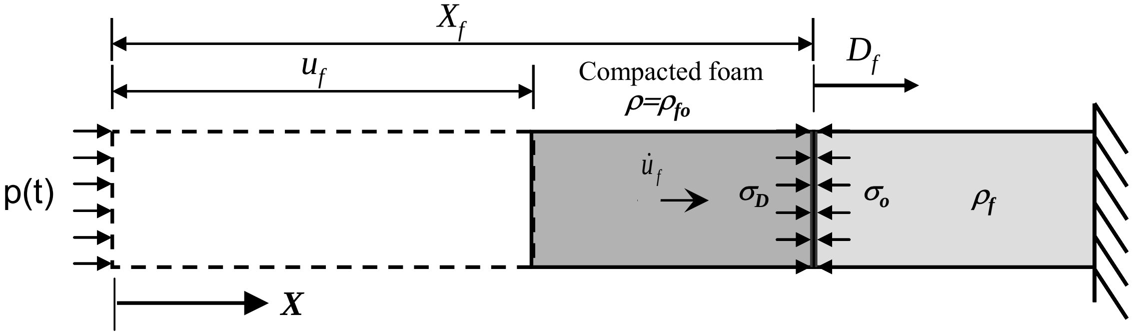

Figure 3.2: Compaction of foam up to time *t*.

At time *t=0*, when the blast pressure wave is incident on the foam, the stress in the foam instantaneously builds up to σ_0, while strain and particle velocity are equal to zero throughout the foam. The boundary conditions of the foam bar correspond with the applied pressure history, *p(t)* at the loaded end while the displacement and velocity at the other end (distal end) of the foam bar (supported by a reaction wall) are always zero. At any given time *t*, the compaction front is located at X_f in the global (fixed) coordinate system, while the displacement of loaded end produced by the compaction is equal to u_f (as shown in

---

[2] As pointed out by Tan et al. [2005], this compaction front resembles a shock front with a jump in the field variables across the front. However, unlike the classical shock front, it is an inertial phenomenon associated with high velocity compression of the porous material.

Figure 3.2). The instantaneous velocity of the compaction front is equal to D_f. The material behind the shock front is in a compacted state, while the material ahead of the traveling compaction front has a strain equal to zero. The strain in the material behind the shock front is uniform and equal to ε_D. From the definition of engineering strain,

$$\frac{u_f}{X_f} = \varepsilon_D \tag{3.1}$$

The conservation of mass of the foam can be written as (strictly valid for one-dimensional strain)

$$\rho_f A X_f = \rho_{f0}(X_f - u_f)A \tag{3.2}$$

From Equations 3.1 and 3.2, the density of foam after being compacted can be thus obtained as

$$\rho_{f0} = \frac{\rho_f}{(1-\varepsilon_D)} \tag{3.3}$$

Since in the RPPL model, the strain in the compacted part is always a constant equal to ε_D, the velocity is uniform throughout the compacted foam, an additional relation can be derived relating the velocity of the compaction front with the velocity of the loaded end

$$\frac{\dot{u}_f}{D_f} = \varepsilon_D \tag{3.4}$$

where $\dot{u}_f$ is the time derivative of u_f.

The conservation of momentum of the compacted portion of the bar up to time t, can be expressed as

$$\int_0^t \left(p(\tau) - \sigma_o\right) d\tau = \rho_f X_f \dot{u}_f \tag{3.5}$$

Substituting for X_f from Equation 3.1 in 3.5

$$\int_0^t \left(p(\tau) - \sigma_o\right) d\tau = \frac{\rho_f}{\varepsilon_D} u_f \dot{u}_f \tag{3.6}$$

The displacement of the loaded end can now be obtained by integrating Equation 3.6 with respect to time (when $u_f = 0$ at $t = 0$)

$$u_f^2 = 2\frac{\varepsilon_D}{\rho_f}\int_0^t \int_0^\eta \left(p(\tau) - \sigma_o\right) d\tau d\eta \tag{3.7}$$

Equation 3.7 can also be written as

$$u_f^2 = 2\frac{\varepsilon_D}{\rho_f}\int_0^t M(\eta) d\eta \tag{3.8}$$

where

$$M(\eta) = \int_0^\eta \left(p(\tau) - \sigma_o\right) d\tau \tag{3.9}$$

$M(\eta)$ is the impulse (net momentum) transferred to the foam up to time *t*. It can be seen that the square of the displacement is proportional to the area of the momentum up to time *t*. The velocity of the compacted foam can now be obtained from Equation 3.8 as

$$\dot{u}_f = \frac{\varepsilon_D}{\rho_f} \frac{M(t)}{u_f(t)} \tag{3.10}$$

3.2.1. Critical Length and Maximum Displacement

For foam bar subjected to a blast pressure loading, the compaction stops when the velocity of compacted foam becomes equal to zero. From Equation 3.10, for $t>0$, the condition for the end of compaction is determined as

$$M(T_c)=0 \tag{3.11}$$

where T_c is the critical time when corresponding to the end of compaction. At $t=T_c$, the displacement of the loaded end reaches its maximum value, u_{fc} and the length of foam bar compacted (measured from its original configuration) is referred to as the critical length, L_{cr}. For a foam of a given strength, L_{cr} is also the minimum length required for completely absorbing the impulse of the incident blast pressure wave. Therefore, when $t< T_c$, u_f is calculated using Equation 3.7, whereas when $t> T_c$, $u_f= u_{fc}$ is a constant and is computed by setting $t= T_c$ in Equation 3.7, where T_c is obtained from Equation 3.11.

The solution for the displacement and velocity of the compacted foam can be obtained if the pressure history, *p(t)* is known. In typical blast analysis, a pressure time-history with an exponential profile is considered, such as

$$p(t) = \left(P_o - atm\right)\exp\left(-\frac{t}{T_o}\right) + atm \qquad (3.12)$$

where T_o and P_o are the duration and amplitude of the blast pressure wave, respectively and *atm* refers to the atmospheric pressure. For the assumed blast pressure profile, the displacement u_f is obtained from Equation 3.7, and is given as

$$u_f^2 = \begin{cases} \dfrac{\varepsilon_D}{\rho_f}\left[2P_oT_ot + 2P_oT_o^2\left(e^{-\frac{t}{T_o}} - 1\right) - \sigma_o t\right] & t \le T_c \\ u_{fc}^2 & t > T_c \end{cases} \qquad (3.13)$$

Further, T_c is determined from Equation 3.11 and is given as

$$1 - e^{-\frac{T_c}{T_o}} = \frac{\sigma_o T_c}{P_o T_o} \qquad (3.14)$$

In conventional analysis the blast over-pressure obtained after reflection from a fixed rigid surface is directly prescribed in the form of pressure loading on the structure. In actual structures, the blast over-pressure experienced by a structure, *p(t)* is not predefined.

The magnitude of pressure depends upon the motion of the structure within the duration of the blast pressure wave and vice versa. This therefore represents a coupled problem where the motion of the solid influences the applied pressure, which in turn affects the motion of the solid. The influence of the fluid-structure interaction (FSI) effect has been shown to be particularly important for complaint structures [Subramaniam et al. 2009]. A proper evaluation of the dynamic compaction of foams therefore requires an evaluation of the FSI effects.

3.3. Objectives

The objectives of the work presented here are:

1. To develop a numerical framework for studying the dynamic compaction response of foam subjected to an incident blast pressure wave considering FSI effects.
2. To evaluate the energy transfer between the blast pressure wave and the foam as a function of deformation characteristics of the foam.
3. To evaluate the influence of FSI effects in the dynamic compaction of foam.

3.4. Problem Statement

The setup for evaluating the dynamic compaction of foam considering fluid-structure interaction comprises of the shock-tube arrangement as shown in Figure 3.3. The foam is assumed to fit perfectly inside the tube, which is frictionless. In this one-dimensional idealization, the shock front is planar and there is no flux of air perpendicular to the direction of blast wave propagation. The analysis is performed considering a unit cross-sectional area of the foam. It is assumed that the compaction of the foam results in a planar motion of the front face of foam. The idealization presented here allows for evaluating the compaction of the foam under conditions of one-dimensional strain conditions the incidence of a blast pressure wave with a planar shock front.

In this paper the foam-air interface is assumed to be a condition of no mass flux. This would be directly applicable to closed cell foams. It is also applicable in open cell foams where the magnitude of the applied pressure results in the localization of deformation resulting from crushing of a layer of cells located at the surface. The formation of the highly localized compacted layer then prevents flux of air into the rest of the foam (Ashby and Gibson 199, p. 249).

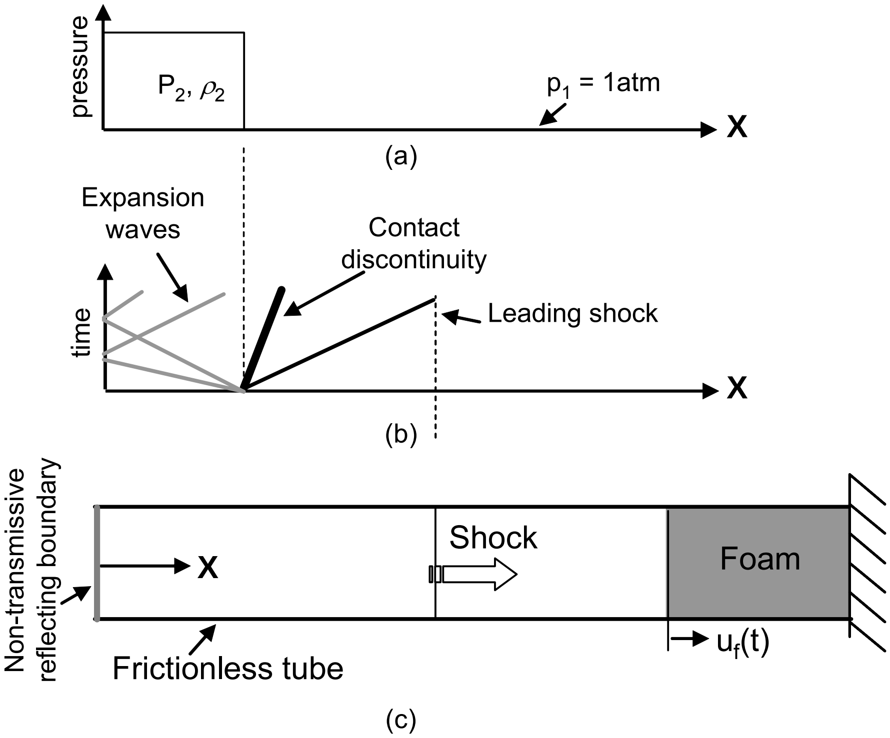

Figure 3.3: Setup for studying blast pressure wave interaction with foam.

The blast pressure wave is created using an initial condition where air at higher pressure and density is separated from air at ambient conditions (Figure 3.3b). A reflective boundary is placed behind the high pressure air. This corresponds to the classical shock-tube arrangement used for generating a blast pressure wave (shown schematically in Figure 3.3c) (Gong 2006, Saad 1998). Starting from the initial pressure discontinuity, a compression pressure pulse comprising of a shock front followed by constant pressure travels along the positive X coordinate, while expansion waves travel in the negative X direction. Upon reflection at the left boundary, the expansion waves start traveling in the positive X direction. The expansion waves catch up with the traveling compression pulse to produce a blast pressure wave with a decaying pressure profile. In this setup, the different parameters of the blast pressure wave such as the shock pressure amplitude and duration can be varied by changing the initial conditions, the location of the initial discontinuity, the location of the reflective back wall and the initial location of the foam.

3.5. Numerical Discretization

The framework for studying the dynamic compaction of foam within the shock tube arrangement is shown in Figure 3.4. The right boundary of the fluid medium is coincident with the free edge of the foam. The motion of the foam was obtained by numerically integrating the equation of motion in the fixed Lagrangian co-ordinates. The formation and propagation of the blast pressure wave is obtained by numerical discretization of the conservation equations within an Eulerian framework. However, since the compaction of the foam produces a movement of the right boundary of the fluid medium and hence results in a change in the fluid domain, an arbitrary moving Euler framework within the finite volume method was used. The fluid-solid coupling was achieved by enforcing the congruence conditions at the air-mass interface. A solution procedure for simultaneously updating the solution of the fluid and solid domains through the enforcement of congruence conditions was developed.

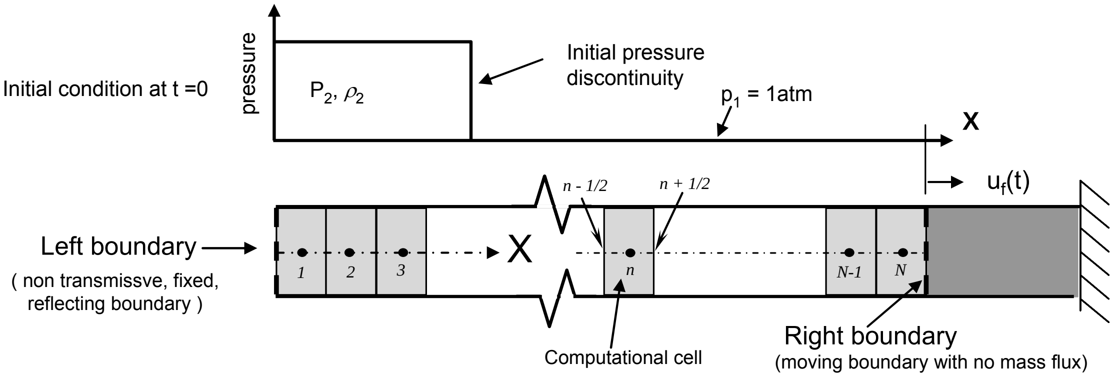

Figure 3.4: Schematic of the numerical implementation of moving boundary problem for blast pressure loading of foam.

3.5.1. Fluid Medium

The air in the shock tube can be described by the one-dimensional set of Euler equations given as

$$\vec{U}_t + \tilde{a}(\vec{U})\vec{U}_x = \vec{S} \qquad (3.15)$$

where

$$\vec{U} = \begin{Bmatrix} \rho \\ \rho v \\ \rho E \end{Bmatrix} \qquad \tilde{a}\left(\vec{U}\right) = \frac{\partial \vec{f}}{\partial \vec{U}} = \begin{Bmatrix} v & \rho & 0 \\ 0 & v & 1/\rho \\ 0 & \rho a^2 & v \end{Bmatrix} \qquad \vec{f} = \begin{Bmatrix} \rho v \\ \rho v^2 + p \\ v(\rho E + p) \end{Bmatrix} \qquad (3.16\text{ a,b,c})$$

a is the local sound speed, $\vec{U}$ is the conservative state vector, $\tilde{a}\left(\vec{U}\right)$ is the Jacobian coefficient matrix in the Eulerian coordinates, $\vec{f}$ is the flux vector, $\vec{S}$ is the vector of source terms (if any), ρ, v, E and p denote the density, velocity, total energy and pressure, respectively. The conservation equations are formulated in terms of four unknowns and therefore the equation of state for a perfect gas provides the additional equation.

$$p = (\gamma - 1)\rho\left[E - \frac{1}{2}v^2\right] \tag{3.17}$$

where γ is the specific heat ratio.

The fluid domain and the associated computational grid can undergo a large deformation due to the motion of the right boundary (the front edge of the foam). Therefore it is more convenient to state the conservation laws in an arbitrarily moving domain. In a general moving coordinate system the conservation laws are described by the Arbitrary Lagrange Euler (ALE) formulation [Hint et al. 1974, Donea et al. 1982]. The one-dimensional integral form of the conservation equations in the ALE formulation are given as

$$\frac{\partial}{\partial t}\int_{\Omega(t)} \vec{U} d\Omega(t) + \int_{\Omega(t)} \frac{\partial \vec{F}}{\partial x} d\Omega(t) = 0 \tag{3.18}$$

where the integral domain $\Omega(t)$ is a function of time, and $\vec{F}$ is the flux vector in the ALE formulation, which represents the net mass momentum and energy flux passing through the moving boundary $\partial\Omega(t)$.

$$\vec{F} = \begin{Bmatrix} \rho V \\ \rho v V + p \\ \rho E V + v p \end{Bmatrix} \tag{19}$$

The contravariant velocity, V is given as

$$V = v - V_c \tag{3.20}$$

where V_c is the prescribed coordinate velocity.

3.5.1.1. Finite Volume Implementation

The computational domain for the finite volume calculations is shown schematically in Figure 3.4. The left boundary of the air tube was treated as a non-transmissive, fixed, reflecting boundary. The right boundary of the fluid domain always coincided with the position of the piston, which is a non-transmissive, moving, reflective boundary. At any given time the entire fluid domain was discretized into N elements of equal size which are centered around grid/node points. The size of elements however varied during the analysis depending upon the motion of the right boundary.

In the ALE formulation, the entire grid can move with time. For each cell, the conservative state vector is defined at the grid point located in the center of the cell and the flux vector is computed at the interface between two adjoining cells. In the numerical scheme, the node/grid points are identified with integers ($1 \le i \le N$). The *i*/(*i*+1) and *i*/(*i*-1) interface is identified as *i*+1/2 and *i*+1/2, respectively.

The following discretized form of the conservation equations is obtained by integrating over the finite volumes [Blom and Leland 1997, Blom 1998].

$$\Delta x_i^{n+1}\vec{U}_i^{n+1} - \Delta x_i^n\vec{U}_i^n = -\Delta t\left\{\vec{F}_{i+1/2}^n - \vec{F}_{i-1/2}^n\right\} \tag{3.21}$$

where Δx is the grid size (the size of the cell) and $\vec{F}_{i-1/2}^n$ and $\vec{F}_{i+1/2}^n$ are the interfacial numerical fluxes at the *i*-1/*2* and *i+1*/2 interfaces at time step *n*. In the ALE formulation Δx_i^n and Δx_i^{n+1} need not be equal since the grid deforms and moves.

3.5.1.1.1. Shock Capturing Scheme

The Godunov's finite volume methodology for shock propagation [Godunov 1959, Van Leer 1979], which has been developed for the Euler-based hyperbolic system, was directly applied to the ALE-based formulation. In this approach, at any time step *n*, a Riemann problem was constructed between two cells defined by the states $\vec{U}_L$ and $\vec{U}_R$, separated by an interface. At every interface between any two cells the Riemann problem is given as RP($\vec{U}_L, \vec{U}_R$), where $\vec{U}_L$ and $\vec{U}_R$ are the vectors of conservative state variables obtained from the cells to the left and the right of the interface. The interfacial numerical flux was then calculated using either the exact Riemann or an approximate solver [Toro 1999, Roe and Pike 1984]. In this paper, the flux was calculated using the weighted averaged-flux (WAF) scheme. The WAF scheme is second order accurate in space and time. According to Godunov's theorem, spurious oscillations are produced in the vicinity of high gradients. So the total variation diminishing (TVD) constraint was applied, resulting in the TVD version of the WAF flux,

$$\vec{F}_{i+1/2} = \frac{1}{2}\left(\vec{F}_i + \vec{F}_{i+1}\right) - \frac{1}{2}\sum_{k=1}^{M} sign\left(c_{i+1/2}^{(k)}\right)\phi_{i+1/2}^{(k)}\Delta\vec{F}_{i+1/2}^{(k)} \tag{3.22}$$

where M is the number of waves in the solution of the Riemann problem. $\Delta\vec{F}_{i+1/2}^{(k)}$ is the flux jump across wave *k* of CFL number given as

$$\Delta\vec{F}_{i+1/2}^{(k)} = \vec{F}_{i+1/2}^{(k+1)} - \vec{F}_{i+1/2}^{(k)} \tag{3.23}$$

$c_{i+1/2}^{(k)}$ is the Courant number for the k^{th} wave of speed $\lambda_{i+1/2}^{(k)}$, given as

$$c_{i+1/2}^{(k)} = \frac{\Delta t}{\Delta x}\lambda_{i+1/2}^{(k)}, \qquad c_{i+1/2}^{(0)} = -1, \quad c_{i+1/2}^{(M+1)} = 1 \tag{3.24}$$

$\phi_{i+1/2}^{(k)}$ is a WAF limiter function. The SUPERBEE limiter was used in the WAF scheme in the present numerical work.

In order to obtain WAF flux from RP($\vec{U}_i^n$, $\vec{U}_{i+1}^n$) using Equation 3.16, the RP($\vec{U}_i^n$,$\vec{U}_{i+1}^n$) needs to be solved in advance to give the following quantities: states $\vec{U}^{(k)}$, fluxes $\vec{F}^{(k)}$, wave speeds $\lambda^{(k)}$ and the jump of the required variables across each waves. In this paper, the approximate Riemann solver of Roe is used to obtain such quantities. Once the numerical flux is determined at time step n the solution can be updated to the next time step *n+1*.

3.5.1.1.2. Treatment of boundary nodes

The left boundary of the fluid domain is a fixed, non-transmissive, reflecting boundary. The right boundary on the other hand represents a moving boundary, which does permit mass flux across the interface. To advance the solution of the *1*st and *N*th nodes (grid points), numerical fluxes at the two boundaries need to be evaluated using a 2nd order accurate scheme. This was done by adding two fictitious grid points on the other side of each boundary, whose states were reflective symmetric to the inside grid points/nodes [Toro 1999, p.491]. For the left boundary at $x = 0$ the fictitious cells are denoted by $i = -1$ and $i = 0$ and for the right boundary the fictitious cells are denoted by $i = N+1$ and $i = N+2$. The right boundary was modeled using reflective/mirror symmetry. The states of the fictitious grid points at the right end are given as

$$\begin{cases} \rho_{N+1}^n = \rho_N^n ; v_{N+1}^n = -v_N^n + 2\dot{u}_s^n ; p_{N+1}^n = p_N^n \\ \rho_{N+2}^n = \rho_{N-1}^n ; v_{N+2}^n = -v_{N-1}^n + 2\dot{u}_s^n ; p_{N+2}^n = p_{N-1}^n \end{cases} \tag{3.25}$$

where $\dot{u}_S^n$ is the velocity of the right boundary, (v^n_{N+1}, ρ^n_{N+1}, p^n_{N+1}) and (v^n_{N+2}, ρ^n_{N+2}, p^n_{N+2}) are the velocity, density and pressure at the fictitious nodes N+1 and N+2.

The states of the fictitious grid points at the left end are given as

$$v_{-1}^n = v_2^n ; \rho_{-1}^n = \rho_2^n ; p_{-1}^n = p_2^n ; v_0^n = v_1^n ; \rho_0^n = \rho_1^n ; p_0^n = p_1^n ; \tag{3.26}$$

where (v^n_{-1}, ρ^n_{-1}, p^n_{-1}) and (v^n_0, ρ^n_0 p^n_0) are the velocity, density and pressure, respectively at the fictitious grid points i=-1 and i=0.

3.5.2. Air-foam interface

The motion of front end of the foam, which is subjected to pressure p(t) is obtained by numerically integrating Equation 3.7. $p(t)$ is the pressure in the N^{th} cell in the finite volume discretization of the fluid medium (air). However, since the motion of the solid obtained from the integration of Equation 3.7 produces a variation in p(t) a solution procedure where the solid and the fluid solutions are updated simultaneously while enforcing the congruence conditions of pressure and velocity at the air-foam interface is presented next.

Let the initial states of the air in the N^{th} cell at the end of a time step be represented by (v^L , ρ^L , p^L). The momentum of the foam at the end of the time step is given by M^R. Within the next time step, due to the motion of the air-foam interface, the transient conditions at the air-foam interface are identified by pressure, p^* and velocity, v^*. The pressure that is developed adjacent to the interface and velocity within the time step obtained from the fluid solver are identified by p^{*L} and v^{*L}, respectively (as shown in Figure 3.5). The relationship between the pressure and velocity at the interface p^{*L} and v^{*L} are available from aerodynamics depending on whether the left moving wave(s) is a shock or rarefactions (Toro 1999, p. 122-123 for rarefaction)

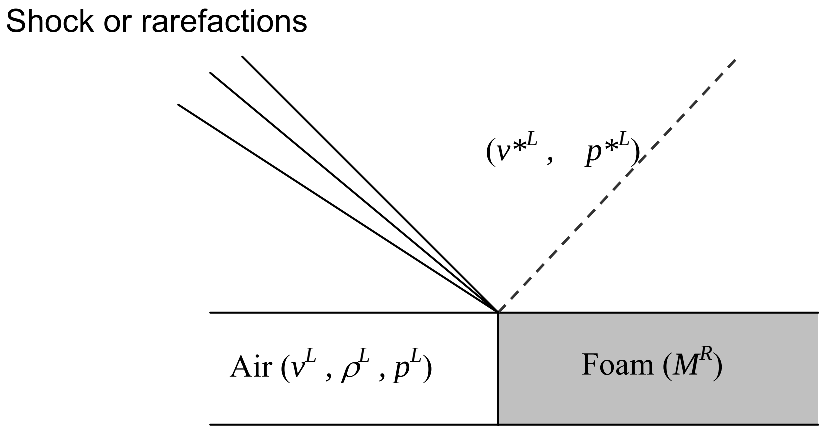

Figure 3.5: Schematic representation of solving for the Interfacial pressure and velocity

$$v^{*L} = v^{*L}(p^{*L}; U^L) = \begin{cases} v^L - \left(p^{*L} - p^L\right)\left(\dfrac{A^L}{p^{*L} + B^L}\right)^{\frac{1}{2}} & \textit{shock} \quad p^{*L} > p^L \\ v^L - \dfrac{2c_L}{\gamma - 1}\left[\left(\dfrac{p^{*L}}{p^L}\right)^{\frac{\gamma-1}{2\gamma}} - 1\right] & \textit{rarefaction} \quad p^{*L} < p^L \end{cases} \tag{3.27}$$

where

$$A_L = \frac{2}{(\gamma+1)\rho^{*L}}; B_L = \frac{(\gamma-1)}{(\gamma+1)} p^{*L}; and \quad U^L = \begin{Bmatrix} v^L \\ \rho^{*L}, \\ p^L \end{Bmatrix} \tag{3.28}$$

From the motion of the foam, the relationship between the applied pressure and velocity for the foam at the interface p^{*R} and v^{*R} can be derived considering the relationship between the displacement, u_f and applied pressure within a time step derived from Equation 3.7

$$\Delta u_f^2 = 2\frac{\varepsilon_D}{\rho_f}\int_{t_o}^{t_o+\Delta t}\int_0^{\varsigma}\left(p^{*R}(\tau)-\sigma_o\right)d\tau d\varsigma = 2\frac{\varepsilon_D}{\rho_f}\int_{t_o}^{t_o+\Delta t}\left[\int_0^{\varsigma}\left(p^{*R}(\tau)-\sigma_o\right)d\tau + \int_{t_o}^{\varsigma}\left(p^{*R}(\tau)-\sigma_o\right)d\tau\right]d\varsigma$$

$$= \frac{\varepsilon_D}{\rho_f}\left[2M^R\Delta t + \left(p^{*R}-\sigma_o\right)\Delta t^2\right] \tag{3.29}$$

If Δt is the duration of the time step, the average velocity in the time step is

$$v^{*R} = \frac{\Delta u_f}{\Delta t} \tag{3.30}$$

giving

$$v^{*R} = v^{*R}(\mathrm{p}^{*R};\mathrm{U}^R) = \sqrt{\frac{\varepsilon_D}{\rho_f}\left[\frac{2M^R}{\Delta t} + \left(p^{*R}-\sigma_o\right)\right]} \tag{3.31}$$

where

$$\mathrm{U}^R = M^R \tag{3.32}$$

The congruence conditions require that the following conditions are satisfied within each time step

$$p^{*L} = p^{*R} = p^* \tag{3.33}$$

and

$$v^{*L} = v^{*R} = v^* \tag{3.34}$$

which combined with Equations 3.27) and 3.31 leads to the following,

$$F(p^*; U^L, U^R) = v^{*L}(p^*; U^L) - v^{*R}(p^*; U^R) = 0 \tag{3.35}$$

where F is the objective function in $p*$. Equation 3.35 represents a non-linear equation in p^*, which was solved using the secant method given as

$$\mathrm{p}^{*k+1} = \mathrm{p}^{*k} - \frac{(\mathrm{p}^{*k} - \mathrm{p}^{*k-1})}{\mathrm{F}(\mathrm{p}^{*k}) - \mathrm{F}(\mathrm{p}^{*k-1})} * \mathrm{F}(\mathrm{p}^{*k})$$

where k is the iteration number.

Starting at $t=t_n$, when the initial states of the air and the foam (U^L, U^R) are known, the Air-Foam system is integrated in time to obtain the solution at time t_{n+1} as (shown in Figure 3.6)

1. At the beginning of each time step interfacial pressure and velocity are solved using an iterative scheme discussed above.
2. The air is integrated to tn+1 using the interfacial velocity from Step (i) as the boundary velocity.
3. The foam is updated to the next time level (tn+1) using the interfacial pressure calculated in Step (i).

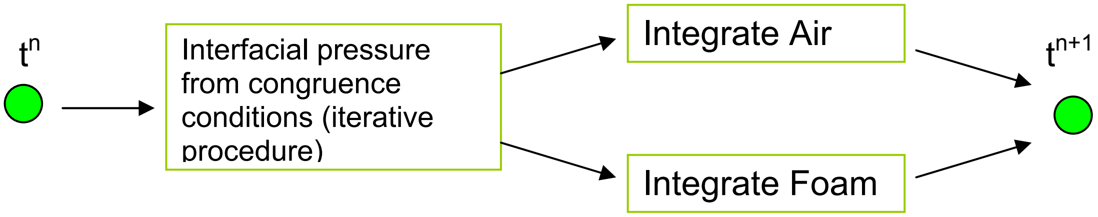

Figure 3.6: Schematic representation of the algorithm for fluid-structure coupling

3.6. Results of Analysis

The origin of the fixed global coordinate system was coincident with the left reflecting boundary. The entire fluid domain was discretized into 100 cells (elements). The number of cells was kept constant. The size of the cells was varied to account fro the moving boundary such that the entire fluid domain was divided into 100 cells of equal size at any given instant. The structural mass coincided with the right boundary of the 100th cell. The initial and boundary conditions were prescribed to achieve an incident blast pressure amplitude at the initial location of the mass equal to 10 MPa. The duration for the pressure to decrease to a value 10/e Mpa was equal to 0.32 ms. The blast pressure characteristics, were taken from the field experiments conducted by Hanssen et al. (2002). The incident blast pressure wave was created considering the initial length of the fluid domain equal to 1.5 m, which was discretized into 100 cells. The location of the initial discontinuity (in pressure and density) was located at the interface between the 5th and the 6th cells. Initial conditions in the first five cells were: $v_L = 0$ m/s, $p_L = 40$ atm (4.053 MPa) and $\rho_L = 49$ kg/m^3. The initial conditions in the remaining cells were: $v_R = 0$ m/s, $p_R = 1.0$ atm and $\rho_R = 1.225$ kg/m^3. In order to achieve the blast pressure wave of the required pressure amplitude and to increase the intensity of the blast, an extra source term was added to the conservation equation of energy in the first time step. The source term was added to the cells in the high pressure region and was a constant equal to 69.6x10^6 J. In addition, to achieve the require duration, the conditions given in Equation 3.36 were prescribed at the virtual grid points at the left boundary until a blast pressure wave formed within the fluid domain. Prescribing a lower pressure in the virtual cell resulted in a sharper decrease in the pressure.

$$v_{-1}^n = v_0^n = 0; \rho_{-1}^n = \rho_0^n = 1.225 kg/m^3; p_{-1}^n = p_0^n = 0.1 atm; \tag{3.36}$$

Analyses were performed to study the dynamic compaction of foams with different densities and hence strengths. Two different Aluminum foams with relative densities ρ_f equal to 150 and 350 kg/m^3 were considered. These foams were used by Hanssen et al (2002) in their experimental study and had σ_o values equal to 1 MPa and 5 MPa, respectively. The densification strain was estimated using the empirical formula provided by Ashby and Gibson (1999, p. 208)

$$\varepsilon_D = 1 - 1.4\left(\frac{\rho_f}{\rho_s}\right) \tag{3.37}$$

The ε_D was calculated to be 0.922 (for ρ_f = 150 kg/m^3) and 0.819 (for ρ_f = 350 kg/m^3).

The results of analysis showing the reflected pressure history, displacement and velocity of the loaded end of the foam are shown in Figure 3.7. The results obtained from an uncoupled analysis, where the reflected over-pressure off a fixed rigid surface is directly applied to the foam as an external pressure loading are also shown in the Figure for comparison. The difference in the reflected overpressure at the face of the foam is significant only in the early part. Subsequently, the reflected pressures history from the foam approaches values which are close to those obtained from the rigid wall. The difference in applied pressure history obtained from the coupled and uncoupled analysis is evident in the velocity of the front face of the foam. The initial velocity, immediately after reflection of the shock front, is significantly different for the two cases. With time, however, this difference reaches a constant value, when the driving pressures from the two analyses become equal. The final compacted length predicted by the two analyses, are also different, with the difference being more significant for the stronger foam. In both cases, the uncoupled analysis over-predicts the final compacted length of the foam.

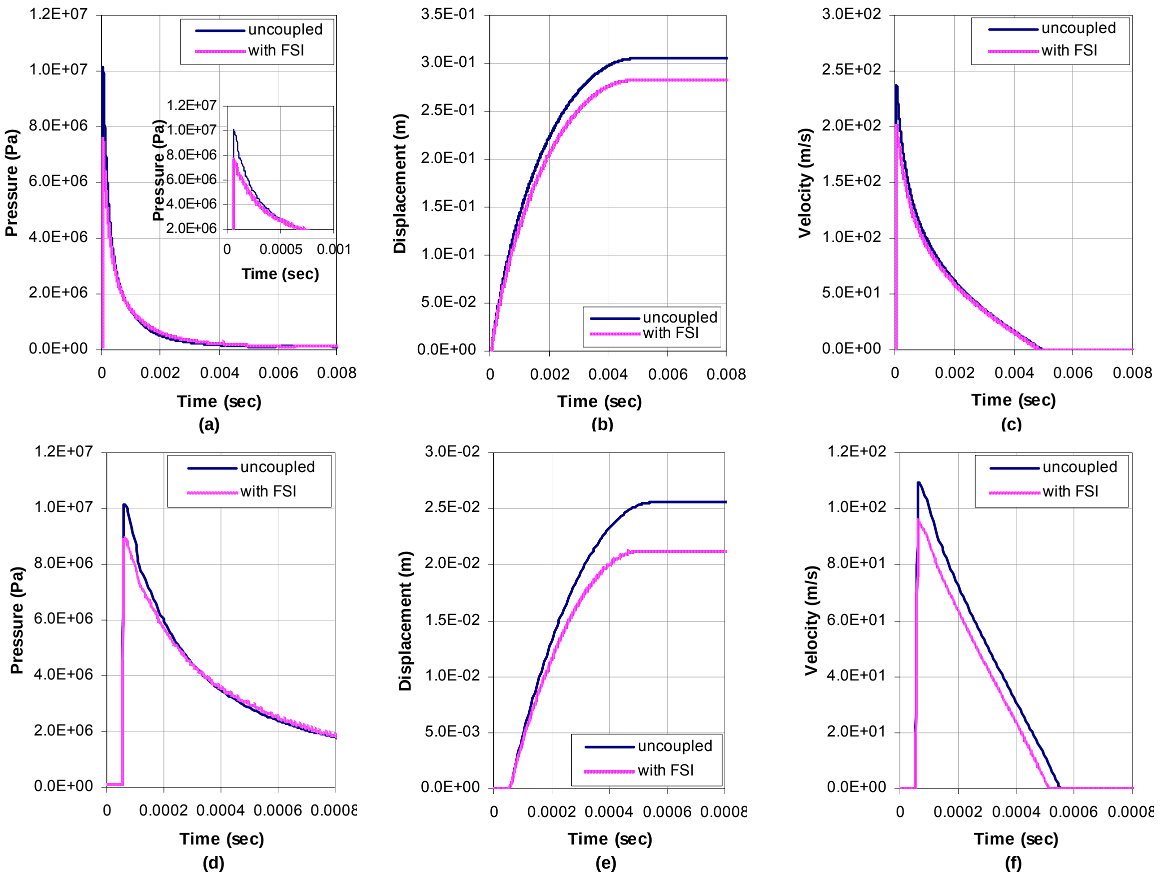

Figure 3.7: Comparison between uncoupled analysis and analysis considering FSI: (a), (b), (c) reflected pressure, displacement and velocity for σ_o =1MPa foam; (d), (e), and (f) reflected pressure, displacement and velocity for σ_o =5MPa foam.

Following the reflection of the shock front, there is an immediate increase in the velocity of the loaded face of the foam, which then decreases, eventually reaching a value of zero. It should be noted that under the assumption of the RPPL model, since the compacted foam behaves like a rigid body, the velocity of the loaded end of the foam is identical to the particle velocity of the compacted foam. The condition of the particle velocity of the compacted foam reaching a zero value corresponds with the end of the compaction front in the material. Comparing the different foams, it is obvious that the compaction of a stiffer foam lasts for a shorter time It is however interesting to note that the compaction of the foam continues even after the applied pressure decreases below σ_o.

The length of the foam compacted when the particle velocity of the compacted foam is equal to zero corresponds to the critical length, L_{cr}. The L_{cr} for the two foams were determined to be 0.306 m (for ρ_f = 150 kg/m^3) and 0.0259m (for ρ_f = 350 kg/m^3). In comparison, the L_{cr} for the two foams obtained using the conventional analysis, such as Equations 3.11-3.14, are equal to 0.331 m (for ρ_f = 150 kg/m^3) and 0.0311 m (for ρ_f = 350 kg/m^3).

A comparison of the applied blast over pressure and the transmitted stress pulse in material located at distance greater than L_{cr} from the loaded end is shown in Figure 3.8. The results of the analysis indicate that the applied blast pressure loading is transformed into a stress pulse of constant amplitude, followed by the pressure profile of the blast pressure wave after the end of compaction. It should be pointed out that the area under the pressure-time curve is identical for both blast-over pressure and transmitted stress. Since the area under the blast over-pressure curve is denoted as the impulse of the blast pressure wave, it should be noted that there is no change in the impulse of the transmitted stress pulse when compared to the applied blast over pressure.

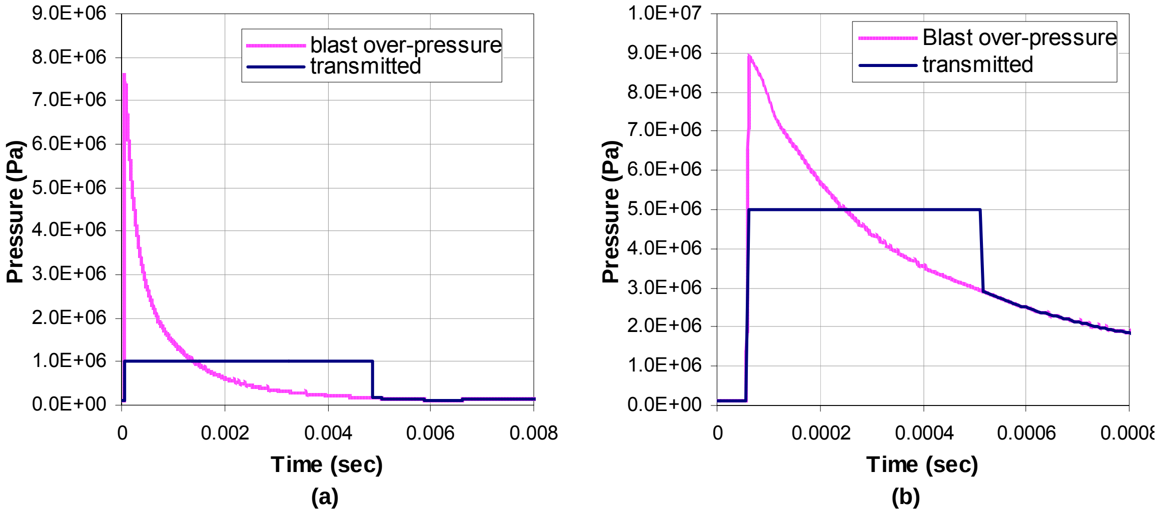

Figure 3.8: Comparison of the applied blast over pressure and transmitted stress wave in the foam.

3.7. Discussion

In the following, the argument of energy will be made for the shock induced dynamic compaction of foam. Even through the concept of foams as excellent energy absorbing materials has been widely used in applications for mitigating the influence of a blast or impact, the energy absorbed by the foam is often evaluated by simply measuring it as the area under the stress-strain curve (Deshpande and Fleck 2004, Li and Meng 2002, Lu and Yu 2003). The correct value of consumed energy by the foam bar in problems where a shock or compaction front forms in the material requires a careful examination of the energy condition across the shock. The required energy equations are formulated considering the configuration of a foam bar, acted by a blast loading *p(t)* at one end while the other end (distal end) of the foam bar is supported by a reaction wall (shown in Figure 3.1).

The equation of conservation of momentum across the shock front is first derived using the control volume method. As shown in Figure 3.9, the control volume (CV) is denoted by the dotted line surrounding the shock front. The pre- and post- compaction states of porous foam are shown in the figure in coordinates attached to the compaction front (where the shock front is treated stationary). Conservation of momentum requires that the change of momentum in CV should equal the net momentum flux from the CV. Since the compaction front is considered to be infinitely thin and weightless, the momentum and hence the change of momentum in the CV should be zero. Therefore the net flux passing through the CV should be zero as well, leading to the following conservation of momentum across the compacting front:

$$-\sigma_0 A dt - (\rho_f V_1 A) V_1 dt + \sigma_D A dt + (\rho_{f0} V_2 A) V_2 dt = 0 \tag{3.38}$$

where $V_1 = -D_f$ and $V_2 = \dot{u}_f - D_f$ are the pre and post compaction particle velocities in a coordinate system attached to the compaction front. Substituting from Equations 3.3 and 3.4 in Equation 3.38, results in an expression for the jump of stress across the compaction front in term of post compaction particle velocity

$$\sigma_D - \sigma_0 = \frac{\rho_f}{\varepsilon_D} \dot{u}_f^2 \tag{3.39}$$

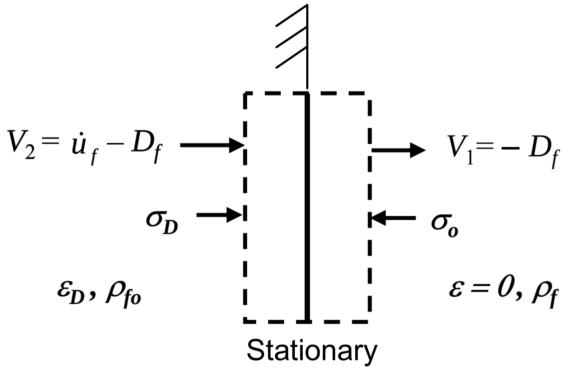

Figure 3.9: Control volume of shock front.

Using the control volume method, the conservation of energy requires that the change of energy within the control volume is equal to the net energy flux passing through the volume,

$$-\sigma_0 V_1 A dt - \left(\rho_f V_1 A dt\right)\left(e_1 + \frac{1}{2}V_1^{\,2}\right) + \sigma_D V_2 A dt + \left(\rho_{f0} V_2 A dt\right)\left(e_2 + \frac{1}{2}V_2^{\,2}\right) = 0 \tag{3.40}$$

where e_1 and e_2 are the pre and post-shock specific internal energies per unit mass. Combined with Equations 3.1, 3.3, 3.4 and 3.39, Equation 3.40 yields the jump condition of energy across the shock front, given as

$$[e] = \frac{1}{2}\frac{\left(\sigma_D + \sigma_0\right)\varepsilon_D}{\rho_f} \tag{3.41}$$

where $[e] = e_1 - e_2$ is the jump of the specific energy, which is also the energy consumed by the foam in the process of shock compaction.

The jump in specific internal energy, $[e]$ can be interpreted as the energy dissipated in the compaction front due to the shock compaction and can be interpreted as the area under the shock cord denoted by the dotted arrow, as shown in Figure 3.10. It should be noticed that the energy consumed in the shock induced compaction is different from the energy consumed in static compaction, which is represented by the area under the quasi-static stress-strain curve (area of the rectangular under line of the plateau stress σ_0). It is obvious that the energy consumed by the shock induced compaction is larger than the energy consumed in static compaction of the material.

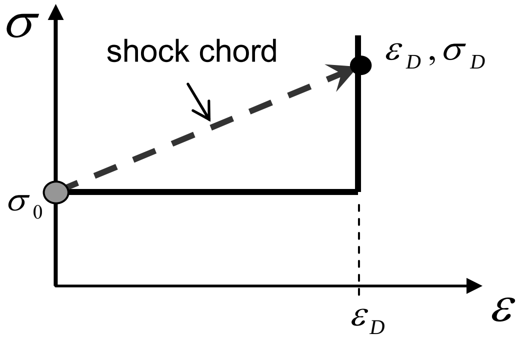

Figure 3.10: Jump across the shock chord for the RPPL material model.

Equation 3.41 can help explain the observed strain rate dependence of the energy absorption for cases where a compaction front is formed in the material during the process of load application (Ashby and Gibson, p. 326). In conventional measurement, when the strain is assumed to be uniform throughout the material, the apparent measured strain is obtained from the deformation of the loaded end as

$$\varepsilon_{app} = \frac{u_f}{L} \tag{3.42}$$

Considering Equations 3.4 and 3.39, the energy dissipation, [*e*], can be expressed in terms of the apparent strain rate as

$$[e] = \frac{1}{2\rho_f}\left(\frac{2\sigma_o L}{D_f}\dot{\varepsilon}_{app} + \rho_f L^2 \dot{\varepsilon}_{app}^2\right) \tag{3.43}$$

The total energy of the foam bar is equal to the summation of the energy dissipated in the compaction front and the kinetic energy of the compacted foam. From conservation of energy, the work done by the blast pressure wave in compacting the foam should balance the energy consumed by the foam and the kinetic energy of foam bar given as

$$\int_0^t \left(\rho_f D_f(\tau)\right)\left[e(\tau)\right]d\tau + \rho_f X_f \frac{\dot{u}_f^2}{2} = \int p^*(t)du_f \tag{3.44}$$

where, p^* is the pressure obtained considering the motion of the boundary. The total energy dissipated in compaction front, the kinetic energy of the compacted foam and the work done by the blast pressure wave as function of time after incidence of the pressure wave on the foam bar are plotted in Figure 3.11. The energy dissipated in the compaction of the foam is the area under the shock chord. The total energy which is the sum of the total energy dissipated and the kinetic energy of the compacted foam is also plotted in the figure. Analyses were performed for foams with different strengths. As seen in the figure, there is a continuous increase in the energy dissipated in the compaction of the foam At any time, the work done by the blast pressure wave on the foam is exactly equal to the total energy, thus proving the conservation of energy is only satisfied if the energy dissipation is taken as the area under the shock chord. The deformation energy based on the area under the stress-strain curve of the material, which has traditionally been used for evaluating energy dissipation in dynamic compaction of foams, is also presented in the figure for comparison. It can be seen that the traditional evaluation of deformation energy of foam under estimates the true energy dissipated in the compaction front. Further, using energy dissipation as the area under the quasi-static response of the material would result in a discrepancy between the work done and the total energy of the system, thereby violating the conservation of energy. Thus, the energy dissipated by the shock induced dynamic compaction is higher than the quasi static energy. It is also interesting to note that the discrepancy between the energy dissipated in dynamic compaction and the energy from quasi-static material response is larger for more compliant foams.

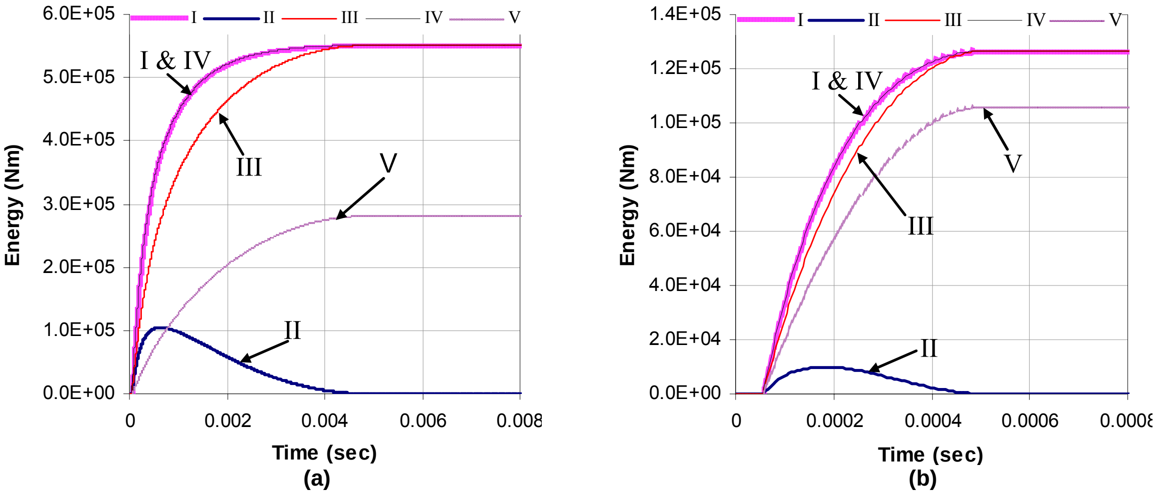

Figure 3.11: The work done by the blast pressure wave and the energy during compaction of the foam, (a) σ_o =1Mpa; (b) σ_o =5Mpa. (I: Work done by blast; II: kinetic energy of the compacted foam; III: Energy dissipated under the shock chord; IV: Total energy; V: Energy dissipation under stress-strain curve).

At any given time during the compaction of the foam, the difference between the work done by the blast pressure wave and the total energy dissipated in the compaction of the material is equal to the kinetic energy stored in the compacted part o the foam. During the dynamic compaction of the foam there is initially an increase in the kinetic energy of the compacted foam followed by a decrease. Since there is a continuous decrease in the particle velocity with time, this increase in the kinetic energy is attributed to the increase in the mass of the compacted foam. Initially, the incremental contribution from the increase in mass is larger than the contribution from the decrease in velocity. The compaction in the foam ends when the kinetic energy of the compacted foam approaches zero. This corresponds in time with the compaction of a length of foam equal to L_{cr}. The kinetic energy available in the foam can potentially explain the continuing compaction even after the applied pressure decreases below σ_o. While the driving force provided by the applied blast pressure decreases below σ_o, the kinetic energy in the compacted foam drives the compaction of the foam.

Comparing foams of different strengths, foams with lower strength (lower σ_o) absorb more energy from the incoming blast pressure wave. These foams therefore require a larger length of material to dissipate the energy, which explains the larger L_{cr} required for low-strength foams. In low-strength foams, during compaction, a higher proportion of the absorbed energy is available in the form of kinetic energy. This can be attributed to the higher particle velocity in low strength foams. These results are in agreement with the findings of Hanssen et al. (2002), who observed a decrease in the energy transfer from a charge driven blast to foam on increasing the foam density (and hence its strength).

In the case when the blast pressure wave is directly incident on the structure, there is a direct stress transfer to the solid. However, when a porous material is placed in front of the structure, the applied blast pressure is transmitted to the structure through the foam. When the length of the foam is less then L_{cr}, at the time of complete compaction of the foam, all the energy absorbed by the foam is not dissipated through compaction of the material. There is a significant portion of kinetic energy available in the compacted foam. The transmitted stress to the structure would therefore contain contribution of the momentum of the compacted foam. Since weaker foams (foams with low σ_o) absorb more energy from the blast pressure wave, if all the absorbed energy is not dissipated through compaction, the additional kinetic energy available in the compacted foam can potentially raise the stress in the structure to a value higher than σ_o. The resulting stress should therefore be higher than that obtained from the remaining blast over-pressure. The assumptions of the RPPL model, while simplifying the analysis, do not allow for determining the level of stress from the impact of the compacted foam with an elastic substrate. Because of the rigid assumptions, the actual stress upon the impact of a rigid object with an elastic substrate cannot be determined.

The results of Hanssen et al. (2002) can now be evaluated considering the time scales of the processes involved. In their experiments, the energy transmitted from a blast pressure wave to a suspended plate, which was arranged as a pendulum. The time period of the suspended plate was equal to 2.59 seconds, while the duration of the blast pressure wave was 0.32 ms. Since the blast pressure duration is insignificantly small when compared to the time period of the structure, it can be treated as a free standing plate for the duration of the blast. The initial velocity of a free standing plate subjected to a blast pressure wave is given as

$$v = \frac{I}{m} \tag{3.45}$$

where I is the impulse of the blast over pressure and m is the mass of the plate. Assuming the mass of the foam is negligible compared to the mass for the foam and since the compressible foam does not produce any changes in the transmitted impulse, the velocity of plate immediately following the blast pressure wave should be identical for foams of all strengths. Thus, if the blast pressure wave were planar there should be no difference in the initial velocity and hence the total height achieved during the motion of the plate as a pendulum. The observed increase in the total height achieved during the motion of the pendulum when using foam can thus be attributed to an increase in the transmitted impulse. This suggests that the geometric effects observed in the experiments, which produced the non-planar compression of the foam, resulted in an increase in the transmitted impulse to the structure. It should be mentioned that in their experiments, Hanssen et al., did not measure the incident blast pressure characteristics for each test. The mass of the charge was used to estimate the applied pressure. The increase in the transmitted impulse therefore cannot be directly verified from the experimental results.

These results however clearly illustrate the need to recognize the role of foam in providing blast mitigation. The role of foam needs to be evaluated considering the response of a structural element subjected to an applied blast pressure loading. As shown in Figure 3.12, there are two major time scales associated with the blast response of a structure. The short time scale which is ranges in order from 10^{-6} to 10^{-3} seconds is associated with wave propagation in the material. Eventually, motion of the structure associated with the vibration signature develops on a time scale on the order of 10^{-3} to 10 seconds. The primary role of foam in a blast mitigation strategy would be to decrease the amplitude of the stress transmitted to the substrate. This would directly influence the stress wave propagation in the substrate material of the structural element in contact with the foam. Thus the influence of the foam is only available in the short time scale associated with wave propagation in the material of the structure. Decreasing the stress amplitude of the blast pressure wave would decrease the level of damage in the material associated with stress wave generated in the material. If there is no damage associated with stress wave propagation in the material, the vibration signature of the structural member is not influenced by the presence of the foam when the blast pressure duration is shorter than the period of the structure since the total impulse of the blast is unchanged.

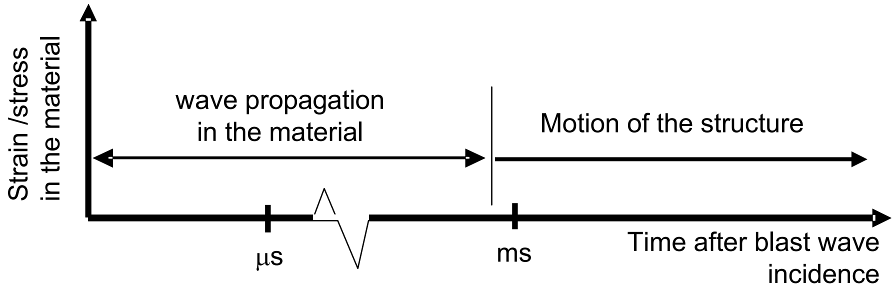

Figure 3.12: Schematic representation of the time scales involved in the blast response of a structure.

3.8. Conclusions

The dynamic compaction of foam which is subjected to an air blast pressure wave is investigated considering the influence of FSI during it motion. Based on the results the following conclusions can be drawn:

1. The influence of FSI is only significant during the early part of the applied blast pressure.
2. The compaction of the foam does not stop when the applied pressure decreases below the strength of the foam. The kinetic energy available in the compacted part of the foam produces additional compaction of the foam.
3. Foams with lower strength absorb higher energy from the incident blast pressure wave and require a larger length of compaction to fully dissipate this energy.

4. The energy dissipated by the foam during dynamic compaction produced by a blast pressure wave is higher than the energy obtained as the area under the stress-strain curve.
5. The energy dissipation would exhibit a strain rate sensitivity if the apparent strain measured using the displacement of the load is used.

Chapter 4: Finite Volume Implementation of a Riemann Solver for Evaluating Dynamic Compaction of Foams

4.1. Introduction

Brittle and metallic closed-cell foams and cellular materials with high porosity exhibit a concave stress-strain relationship which is associated with irreversible compaction of the internal structure. Such materials are often used for applications requiring energy absorption and attenuation of applied stresses such as, packaging, impact protection and blast mitigation. The cellular microstructure of foams endows them with several favorable characteristics for use in developing protective schemes, such as, a low weight and relatively constant strength at large strain associated with crushing of the microstructure [Ashby and Gibson 199 for a review; Hanssen et. al. 2002]. With the modern foam forming techniques, the crushing force can be tailored, thus limiting the transmitted stress to a target to a desired safe level. Developing applications for energy dissipation using foams requires an understanding of the compressive response under various transient loading such as solid impact or air blast/shock.

Typical uniaxial quasi-static stress-strain curve of closed-cell foam and cellular materials is shown in Figure 4.1. In the initial linear elastic region the material follows Hooke’s law. The Poission’s ratio of most foams in the initial linear elastic region has been shown to be relatively independent of the relative density and is equal to 1/3 [Ashby and

Gibson 1997, p. 193]. The concave response is associated with the collapse of the internal structure and leads to densification of the material. The end of the linear elastic response in the load envelope is identified by P_o which is defined by the initial critical strain and the initial critical stress $(\varepsilon_{po}, \sigma_{po})$. P_o is associated with the initiation of inelastic behavior, which leads to irreversible volumetric contraction and is associated with the collapse of cells. Cells within a small region collapse leading to a local densification of the material. The cell collapse is associated with formation of plastic hinges (or plastic collapse) for metallic foams and with brittle crushing for brittle foams [Gibson and Ashby 1999 pp. 203]. It should be noted that while engineering strain is calculated using the overall shortening of the entire length of foam, the local deformation in the material is very non-uniform in the concave part of the load-envelope. The statistical variations in the wall thickness, cell dimensions and orientation, and cell wall strength produce local anisotropy in the material properties and strength, which results in a localized crushing of cell. The accumulation of bands of non-contiguous crushed cells results in an overall shortening of the foam. The collapse of cells and the densification of material produce a gradual upward concave stress-strain response with increasing slope as more cells are compacted. In closed-cell foams, the contribution of gas pressure to the measured strength properties is insignificant and can be neglected [Tan et. al. 2005 Part I, Despande and Fleck 2000].

In materials which exhibit concave stress-strain curve, the possibility of shock formation has been established [Hopkins 1968, Morland 1959, Nowinski 1965]. The formation of a compaction front[3] that exhibits shock-type characteristics has been

---

[3] The term compaction front is used to define the strong discontinuity which is associated with high velocity compression of the material. Unlike the classical shock wave, the propagation of the interface in the material is an inertial phenomenon, and has a finite dimension on the order of the cell size. The

experimentally reported in aluminum foams subjected to a solid impact [Radford et. al. 2005, Tan et. al. 2005 part I]. The localization is initiated directly below the impact as the first layer of cells collapse. A well-defined compaction front, which is associated with a strong discontinuity and exhibits shock-type characteristics, propagates in the material. The strong discontinuity produces an interface between the crushed cells and the uncrushed cells. The densification of the material associated with the propagation of a well defined front, produces the dynamic compaction of the foam and leads to irreversible volumetric contraction.

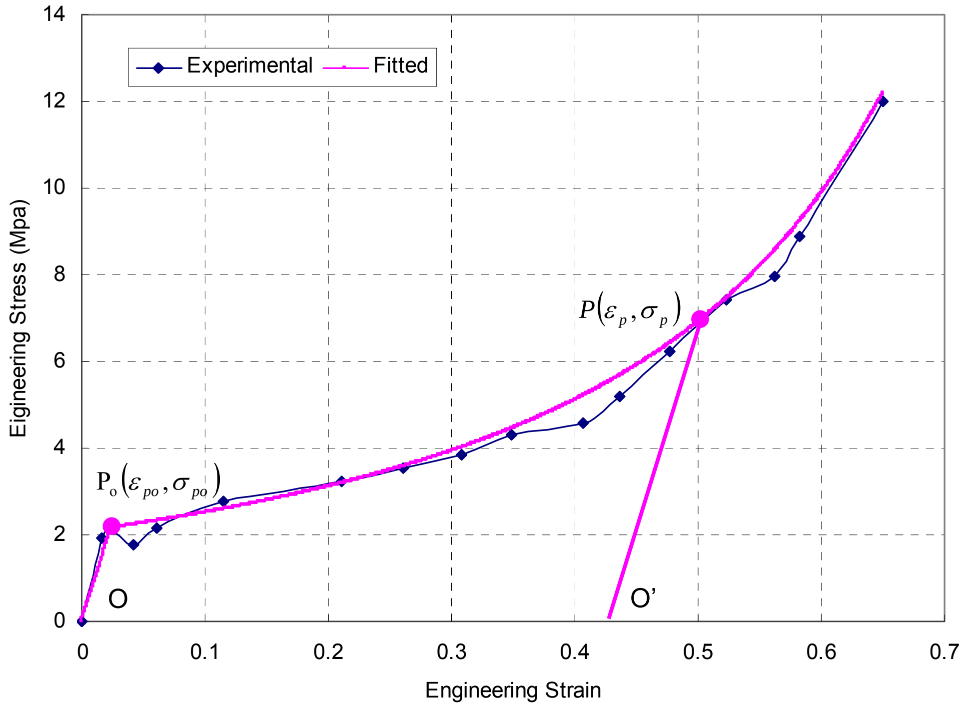

Figure 4.1: Typical stress-strain curve of foams (Aluminum, nominal density 351kg/m^3).

---

compaction front is idealized to be of zero thickness with shock-like jump conditions across the interface. This follows the convention previously defined by Tan et al. (2005).

Predicting the propagation of the compaction front[4], which is associated with a strong discontinuity and exhibits shock-type characteristics, in foams is challenging, requiring solutions to non-linear hyperbolic equations. One popular approach, known as the simplified shock model based on the rigid, perfectly-plastic, locking (RPPL) idealization of the actual stress strain response, leads to simple analytical models. This approach has been used for predicting the propagation of compaction front and the energy absorption in foams for transient loadings [Reid, S.R. and Peng 1997, Tan et. al. 2005 part II]. However, this approach does not allow for realistic predictions of transmitted stress when the compaction front is incident upon an elastic substrate since the rigid idealization predicts infinite stress.

The finite volume method of Godunov type is a shock capturing scheme of high-resolution and has been proven to be a powerful tool for systems of non-linear hyperbolic equations. The method was originally developed for compressible gas dynamics, to treat the Euler equations, in which the shock wave is part of the solution [Toro 1999]. Since Euler equations are nonlinear hyperbolic system, the extension of Govdunov method to general wave-propagation problems associated with different media is natural. The implementation of the finite-volume method within the Lagrangian framework for the linear and non-linear waves in solids has been made by LeVeque [2002]. Leveque and Yong [2003] also developed a finite volume implementation for predicting the propagation of a finite disturbance in materials which exhibit a simple concave strain-stress relation. For such strain-stress relations, the structure of the Riemann problem is fixed and comprises of one right running wave and one left running wave. The wave structure

---

[4] The term compaction front is used interchangeably with shock front.

associated with each wave is shown to be either a shock wave or a continuous tension fan. While this approach is promising, extension of this approach for the case of foams, which exhibit a significant initial elastic response in addition to the concave stress-strain curve requires careful consideration. To advance the solution in time the numerical flux obtained from the solution of the local Riemann problem defined by two adjacent cells is required. The stress strain curve of the type shown in Figure 4.1 is expected produce a more complex wave structure in the Riemann problem.

The main objective of this paper is to develop a numerical scheme, which can be used for predicting the propagation of finite disturbance in a material which exhibits an upward concave stress-strain relationship. A finite volume implementation for determining the propagation of a compaction front in foams, which exhibit an initial linear response followed by a concave response, is presented. The wave structure associated with the Riemann problem resulting from the stress-strain curve of the form shown in Figure 4.1 is considered. The solution of the Riemann problem is developed and is used in implementing the Second-Order TVD version of WAF Godunov Method for determining the propagation of a stress waves and compaction front in foams.

4.2. Problem Statement

Equations for dynamic compaction of foam under conditions of one-dimensional strain (1-D strain) are developed in this section. The compressive stress-strain response of the foam obtained from the uniaxial, monotonic, quasi-static loading is referred to as the load envelope in future discussions. The load-envelope for the case of 1-D strain can be fitted with the following relations [Lopatnikov et. al. 2003]

$$\sigma = \begin{cases} \sigma_p + E(\varepsilon - \varepsilon_p) & \varepsilon \le \varepsilon_p \\ \sigma_{po} - AE(1-\varepsilon_{po})^{-\alpha} + AE(1-\varepsilon)^{-\alpha} & \varepsilon > \varepsilon_p \end{cases} \tag{4.1}$$

where ε is the engineering strain, α is a constant greater than zero, A and E are material constants, ε_{po} and σ_{po} (=ε_{po}×E) are the initial critical strain and stress, respectively and ε_p and σ_p are the current critical strain and stress, respectively. In developing this relationship, the maximum stress in the concave part of the load-envelope experienced by the foam (Point P in Figure 4.1) is identified as the current critical stress (σ_p). At the initiation of loading, the current critical strain and the current critical stress are set equal to ε_{po} and σ_{po}, respectively. The values of ε_p and σ_p are updated when the stress exceeds σ_{po}. The unloading from the load-envelope is assumed to be along straight line parallel to the initial elastic response (line OP in Figure 4.1).When the foam is re-loaded, the material response follows the load-envelope when the stress exceeds the critical stress (σ_p). The strain-stress curve given by Eq. (1) is plotted in Figure 4.1 with $E=9\times10^7$ Pa, A=0.0294, α=1.5, ε_{po}=0.024 (which gives $\sigma_{po}=2.16\times10^6$pa). It should be noted that, E refers to elastic modulus under conditions of 1-D strain.

The governing equations for one-dimensional wave propagation in a compressible solid stated in the total Lagrangian coordinate form are given as [Leveque 2002]

$$\begin{cases} \dfrac{\partial \varepsilon}{\partial t} + \dfrac{\partial v}{\partial X} = 0 \\ \dfrac{\partial v}{\partial t} + \dfrac{1}{\rho_o}\dfrac{\partial \sigma}{\partial X} = 0 \end{cases} \tag{4.2}$$

or

$$\vec{U}_t + \vec{F}_X = 0$$

where

$$\vec{U} = \begin{Bmatrix} \varepsilon \\ v \end{Bmatrix}, \quad \vec{\mathrm{F}} = \begin{Bmatrix} \mathrm{v} \\ \sigma/\rho_o \end{Bmatrix} \tag{4.3}$$

ε is the engineering strain, *v* is the particle velocity, σ[5] is the stress and ρ_o is the initial density. It should be noted that in Equations 4.2 and 4.3, compressive strain and compressive stress are positive. Considering the non-linear stress-strain relationship given in Equation 4.1 or 4.2 will result in a non-linear set of hyperbolic equations, requiring a numerical solution.

4.3. Solution of the Riemann Problem

Before formulating the Riemann problem, it is instructive to look at the wave structure in the material. The strain-stress response of the material can be separated into to two parts: the linear part and the nonlinear concave curve with an abrupt change in slope at the critical stress. These would correspond to the initial critical stress for monotonic loading or Point P for reloading following an unloading from the load envelope. There is one elastic wave associated with the linear response and non-linear wave(s) associated with the non-linear concave stress response. The nonlinear waves can generally be either a continuous compression fan or a single shock wave. In materials which exhibit a concave stress-strain relation, the successive waves produced by loading travel faster and form a shock front [Tan et. al. 2005 part II]. For waves present in the Riemann Problem for such a material, when two initial states are separated by a discontinuity, the possibility of having a continuous nonlinear compression fan does not exist and only shock waves are possible.

---

[5] Note that for 1-D strain, the σ (Engineering stress) here obtained as P/(current area) is identical to P/(initial area) since there is no change in the cross-sectional area.

Therefore, the only wave associated with the non-linear compressive response of the foam is a shock wave.

4.3.1 Wave Structure and Relations for Stress and Particle Velocity

The two types of waves discussed above, the linear wave and the shock wave, can be present individually or together in the material depending on the current stress state and the magnitude and the direction of the applied stress. In the following discussion, three wave structures are identified for right running waves and the corresponding wave relations relating the states on the two sides of the wave are derived for each case. The wave structures and waves relations for left running waves are similar.

<u>Case 1:</u> For loading below the load envelope (one right running linear wave)

When the state of current stress in the material is below the load envelope, the corresponding stress-strain response is linear. Such a stress state exists when the material is in the initial linear elastic part of the load envelope or when it is unloaded from the load envelope. Below the critical point "P" (including the initial critical point "P$_o$") as shown in Figure 4.2 (a), where R denotes pre-wave state and R* denotes post-wave state, the material response is linear and one right running wave exists in the X-t plane as shown in Figure 4.2 (b). The wave relation across the right running wave is the linear wave relation, given as

$$v_{R*} = f_R(\sigma_{R*}) = v_R + \frac{(\sigma_{R*} - \sigma_R)}{a_E \rho_o} \quad \text{when} \quad \sigma_{R*} \le \sigma_p \ \text{ and } \ \sigma_R \le \sigma_p \tag{4.4}$$

where a_E is the linear wave velocity given as

$$a_E = \sqrt{E/\rho_o} \tag{4.5}$$

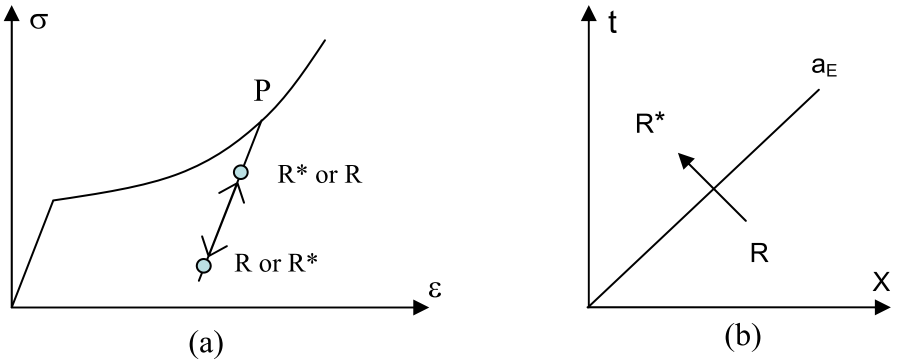

Figure 4.2: Case 1, (a) loading history and (b) wave structure.

***Case 2:* For loading from the load envelope (one right running compaction front)**

When the material is compressed from a point “R” which is coincident with the critical point P to the other point R* above P as shown in Figure 4.3 (a), a compaction front emerges in the X-t plane as shown in Figure 4.3(b). The pre-wave state “R” and post-wave state “R*” are related by the “Rankine-Hugoniot” relationship for right running shock wave, given as

$$v_{R*} = f_R(\sigma_{R*}) = v_R + \frac{(\sigma_{R*} - \sigma_R)}{s_R \rho_o} \qquad \text{when} \quad \sigma_{R*} > \sigma_p \ \text{ and } \ \sigma_R = \sigma_p \tag{4.6}$$

where s_R is the velocity of the shock wave given as

$$s_R = \sqrt{\frac{\sigma_{R*} - \sigma_p}{(\varepsilon_{R*} - \varepsilon_p)\rho_o}} \tag{4.7}$$

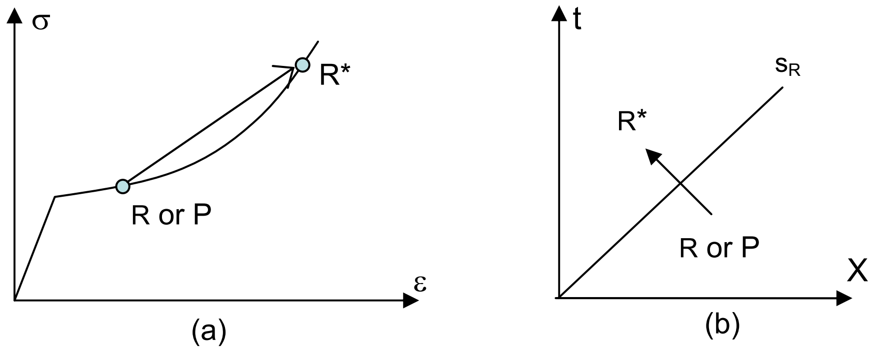

Figure 4.3: Case 2, (a) loading history and (b) wave structure.

***Case 3:* For loading from below the critical stress to a point on the load envelope (one right running linear precursor wave and one right running compaction front)**

In case 3, the material is compressed from a point R below the load-envelope and the corresponding critical stress, Point P, to a point R* above P as shown in Figure 4.4 (a). Two waves, one right running linear wave traveling at the speed a_E and one shock wave traveling at the speed of shock s_R, emerge in the X-t plane as shown in Figure 4.4 (b). From the stress-strain response of typical foams, the elastic modulus is larger than the slope of the shock chord. Thus it can safely be assumed that $a_E > s_{R.}$ and since the elastic wave generally travels faster than the compaction front, the two waves will not converge.

The initial state R is first changed to an intermediate state P, the current critical point, across the linear wave and than changed to the final state R* across the right running compaction front. The relation between state R and P obeys linear wave relations given by Equation 4.4 and the one between state P and R* obeys "Rankin-Hugoniot" relationship given by Equation 4.6. Combining Equations 4.4 and 4.6 leads to the relation between R and R* across the two waves, given as

$$\begin{aligned} v_{R*} = f_R(\sigma_{R*}) &= v_p + \frac{(\sigma_{R*} - \sigma_p)}{s_R \rho_o} \\ &= v_R + \frac{(\sigma_p - \sigma_R)}{a_E \rho_o} + \frac{(\sigma_{R*} - \sigma_p)}{s_R \rho_o} \end{aligned} \quad \text{when} \quad \sigma_{R*} > \sigma_p \quad \text{and} \quad \sigma_R < \sigma_p \qquad (4.8)$$

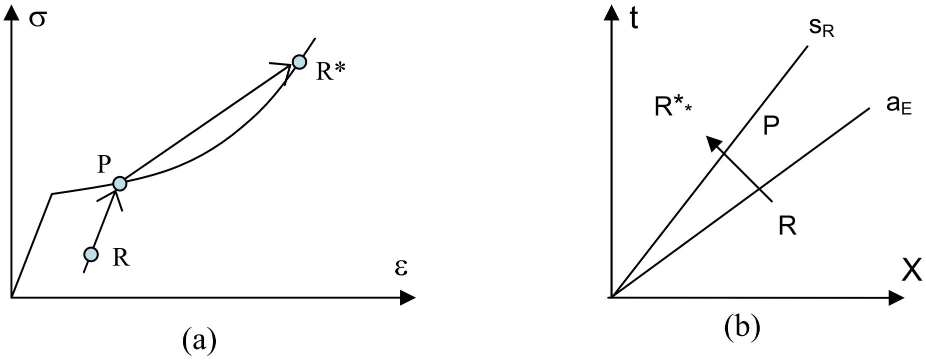

Figure 4.4: Case 3 (a) loading history and (b) wave structure

The wave structures and wave relations for left running waves are analogous to those for right running waves and are given in the following.

Case 1: ***(one left running linear wave)***

$$v_{L*} = f_L(\sigma_{L*}) = v_L - \frac{(\sigma_{L*} - \sigma_L)}{a_E \rho_o} \qquad \text{when} \quad \sigma_{L*} \le \sigma_p \quad \text{and} \quad \sigma_L \le \sigma_p \qquad (4.9)$$

Case 2: ***(one left running compaction front)***

$$v_{L*} = f_L(\sigma_{L*}) = v_L - \frac{(\sigma_{L*} - \sigma_L)}{s_L \rho_o} \qquad \text{when} \quad \sigma_{L*} > \sigma_p \quad \text{and} \quad \sigma_L = \sigma_p \qquad (4.10)$$

Case 3: ***(one left running linear precursor wave with one left running compaction front)***

$$v_{L*} = f_L(\sigma_{L*}) = v_L - \frac{(\sigma_p - \sigma_L)}{a_E \rho_o} - \frac{(\sigma_{L*} - \sigma_p)}{s_L \rho_o} \qquad \text{when} \quad \sigma_{L*} > \sigma_p \quad \text{and} \quad \sigma_L < \sigma_p \qquad (4.11)$$

where

$$s_L = \sqrt{\frac{\sigma_{L*} - \sigma_p}{\left(\varepsilon_{L*} - \varepsilon_p\right)\rho_o}} \tag{4.12}$$

It should be noted that in general, for cases associated with loading, such as case 2 and 3, continuous compression waves can also be part of the solution. However, only waves in accordance with a local Riemann Problem (RP) are considered here. Therefore the three cases for each direction include all possible wave structures of a local RP in the X-t plane.

4.3.2. Formulation of the Riemann Problem (RP)

For the typical stress-strain relation of foam, the wave patterns associated with the RP on one side of the X-t plane can be one of the 3 cases stated in the previous section. Thus depending on the case, the number of waves on one side of X-t plane is variable. Considering the variable wave structure, the scheme based on the approximate solver of Roe is not suitable. The solution to the Riemann problem is required.

The Riemann problem for the one-dimensional, hyperbolic equation 4.2 or 4.3 is the Initial Value Problem (IVP) with two adjacent constant initial states separated by an interface at X=0. Considering v and σ as the basic independent variables, the states on the left and right of X=0 are identified as $\vec{W}_L = (v_L, \sigma_L)^T$ and $\vec{W}_R = (v_R, \sigma_R)^T$, respectively and the Riemann problem defined by $\vec{W}_L$ and $\vec{W}_R$ is denoted as RP($\vec{W}_L, \vec{W}_R$). At time t>0, left and right running waves emerge in the X-t plane and change the initial states W_L and W_R to an unknown state identified as the star state, $\vec{W}^*$. In the star region, the velocity v^* and stress σ^* are constant on both side of the interface as required by the conditions of displacement compatibility and equilibrium [Toro 1999 pp. 118]. The relation between unknown v^* and σ^* across the right running waves is given by f_R in Equation 4.4, 4.6 or 4.8 and that across the left running wave is given by f_L in Equation 4.9, 4.10 or 4.11

$$v_* = f_L(\sigma_*) = f_R(\sigma_*) \tag{4.13}$$

Equation 4.13 can be solved for the unknown σ^* using an iterative solver. Once σ^* is solved v^* can be calculated using Equation 4.13.

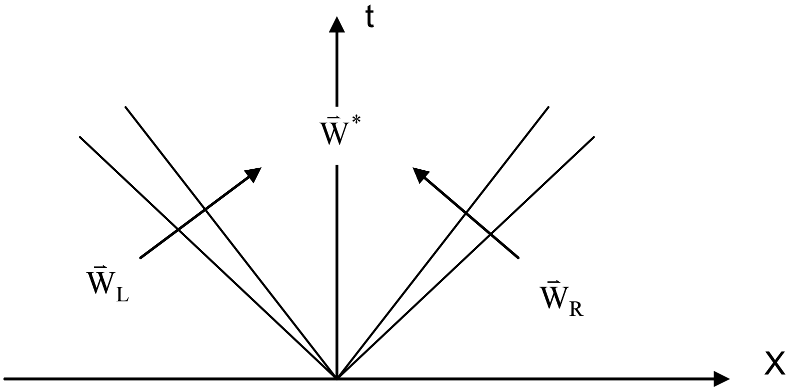

Figure 4.5: Wave structure associated with the local Riemann Problem

4.4. Numerical Implementation and the Second-order Godunov Method

The entire domain occupied by the foam is subdivided into a computational grid of N cells, which are centered around grid/node points. For each cell, the state vector ($\vec{U}$) is defined at the grid point located in the center of the cell and the flux vector is computed at the interface between two adjoining cells. In the numerical scheme, the node/grid points are identified with integers ($1 \le i \le N$). The i/(i+1) and i/(i-1) interface is identified as i+1/2 and i-1/2, respectively.

The following discretized form of the conservation equations is obtained by integrating over the finite volumes [Toro 1999 pp. 205].

$$\vec{U}_i^{n+1} = \vec{U}_i^n - \frac{\Delta t}{\Delta X}\left\{\vec{F}_{i+1/2}^n - \vec{F}_{i-1/2}^n\right\} \tag{4.14}$$

where ΔX is the grid size (the size of the cell) and $\vec{F}_{i-1/2}^n$ and $\vec{F}_{i+1/2}^n$ are the interfacial numerical fluxes at the *i*-1/*2* and *i+1*/2 interfaces at time step *n*.

4.4.1. Shock Capturing Scheme

At any time step *n*, a Riemann problem RP($\vec{\mathrm{W}}_\mathrm{L}, \vec{\mathrm{W}}_\mathrm{R}$) was constructed between two cells, the solution of which can be obtained using the Riemann solver. The numerical flux was calculated using the WAF scheme. The WAF scheme is second order accurate in space and time. According to Godunov's theorem, spurious oscillations in the vicinity of high gradients are to be expected. So the TVD constraint was applied, resulting in the TVD version of the WAF flux [Toro 1999 pp. 467],

$$\vec{F}_{i+1/2} = \frac{1}{2}\left(\vec{F}_i + \vec{F}_{i+1}\right) - \frac{1}{2}\sum_{k=1}^{M} sign\left(c_{i+1/2}^{(k)}\right)\phi_{i+1/2}^{(k)}\Delta\vec{F}_{i+1/2}^{(k)} \tag{4.15}$$

where M is the number of waves in the solution of Riemann problem and $\Delta\vec{F}_{i+1/2}^{(k)}$ is the jump of flux across wave *k*

$$\Delta\vec{F}_{i+1/2}^{(k)} = \vec{F}_{i+1/2}^{(k+1)} - \vec{F}_{i+1/2}^{(k)} \tag{4.16}$$

where $\vec{F}^{(k)}$ are obtained using the solution of the Riemann problem.

In the implementation of the WAF scheme, all left wave(s) are replaced by a single fictitious left running wave 1 carrying the jump from state (1) to the state (2) as shown in

Figure 4.6. Similarly, all right wave(s) are replaced by a single fictitious right running wave 2 carrying the jump from state (3) to the state (2). So M=2 and k=1, 2 in the scheme.

In Equation 4.15, $c^{(k)}$ is the Courant number of wave k at speed $S^{(k)}$,

$$c^{(k)} = \frac{\Delta t}{\Delta X} S^{(k)} \tag{4.17}$$

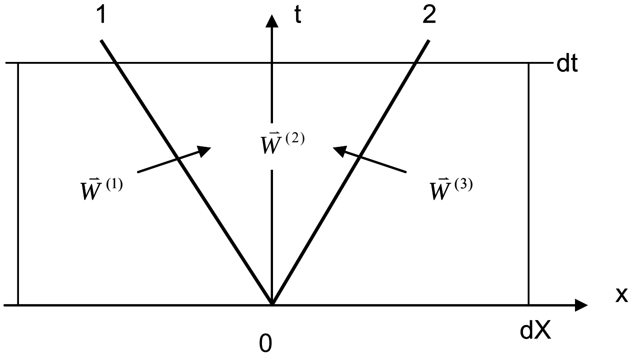

Figure 4.6: Structure of a typical local Riemann Problem for the current WAF scheme

$\phi_{i+1/2}^{(k)} = \phi\left(r_{i+1/2}^{(k)}\right)$ is a WAF limiter function. The parameter $r^{(k)}$ refers to wave k in the solution of RP and is the ratio

$$r_{i+1/2}^{(k)} = \begin{cases} \dfrac{\Delta q_{i-1/2}^{(k)}}{\Delta q_{i+1/2}^{(k)}} & c_k > 0 \\ \dfrac{\Delta q_{i+3/2}^{(k)}}{\Delta q_{i+1/2}^{(k)}} & c_k < 0 \end{cases} \tag{4.18}$$

A quantity that is known to change across each wave family in the solution of the RP can be chosen as the q. For the current problem, choice of q=u or q=σ give satisfactory results. As to the WAF limiters ϕ, the Van Leer's limiter [Toro 1999, p 498] was used

$$\phi_{vl}\left(r,|c|\right) = \begin{cases} 1 & r \le 0 \\ 1 - \dfrac{\left(1-|c|\right)2r}{1+r} & r > 0 \end{cases} \tag{4.19}$$

In order to obtain WAF flux from RP using Equation 4.15, the RP needs to be solved in advance to give the following quantities: states $\vec{U}^{(i)}$, fluxes $\vec{F}^{(i)}$ (i=1, 2 and 3), wave speeds $S^{(k)}$ (k=1 and 2) and the jump of the required variables across each waves. Once the numerical flux is determined at time step n the solution is updated to the next time step *n+1* using Equation 4.14.

4.4.2. Treatment of Boundary Nodes

The computational domain for the finite volume calculations is shown schematically in Figure 4.7. At any given time the entire fluid domain was discretized into N elements of equal size. The foam bar is subjected to a load p(t) at the left boundary and fixed at the right boundary. To advance the solution of the 1st and Nth nodes/grid points, numerical fluxes at the boundary need to be evaluated using the 2nd order scheme. This is done by adding two fictitious grid points on the other side of each boundary. For the left boundary at $x = 0$ the fictitious cells are denoted by $i = -2$ and $i = -1$ and for the right boundary the fictitious cells are denoted by $i = N+1$ and $i = N+2$.

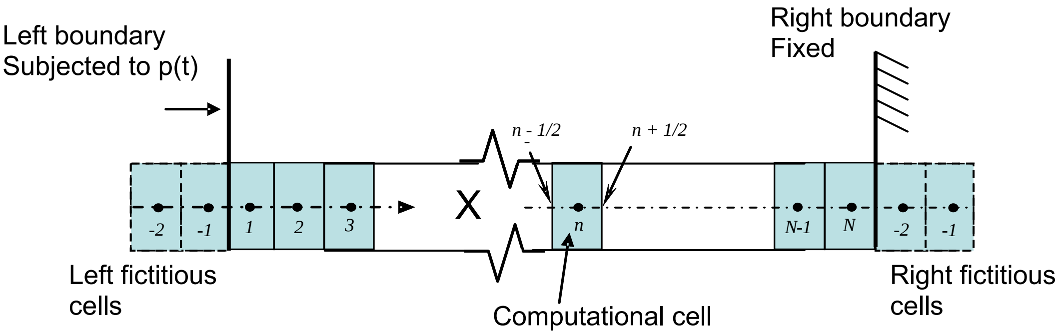

Figure 4.7: The computational domain and boundary cells

Both boundaries are modeled using reflective/mirror symmetry. The states of the fictitious grid points at the right end are given as

$$\begin{cases} \varepsilon_{N+1}^{n} = \varepsilon_{N}^{n}; \varepsilon_{p,N+1}^{\;\;n} = \varepsilon_{p,N}^{\;\;n}; \sigma_{N+1}^{n} = \sigma_{N}^{n}; \sigma_{p,N+1}^{\;\;n} = \sigma_{p,N}^{\;\;n}; v_{N+1}^{n} = -v_{N}^{n} + 2v_{RB}^{n} \\ \varepsilon_{N+2}^{n} = \varepsilon_{N-1}^{n}; \varepsilon_{p,N+1}^{\;\;n} = \varepsilon_{p,N}^{\;\;n}; \sigma_{N+2}^{n} = \sigma_{N-1}^{n}; \sigma_{p,N+2}^{\;\;n} = \sigma_{p,N-1}^{\;\;n}; v_{N+2}^{n} = -v_{N-1}^{n} + 2v_{RB}^{n} \end{cases} \tag{4.20}$$

where $(\varepsilon^{n}{}_{N+1}, \varepsilon_p{}^{n}{}_{N+1}, \sigma^{n}{}_{N+1}, \sigma_p{}^{n}{}_{N+1}, v^{n}{}_{N+1})$ and $(\varepsilon^{n}{}_{N+2}, \varepsilon_p{}^{n}{}_{N+2}, \sigma^{n}{}_{N+2}, \sigma_p{}^{n}{}_{N+2}, v^{n}{}_{N+2})$ are the strain, current critical strain, stress, current critical stress and velocity at nodes N+1 and N+2; v_{RB}^{n} is the velocity of the right boundary and v_{RB}^{n}=0 since the right boundary is fixed.

The states of the fictitious grid points at the left end are given as

$$\begin{cases} \varepsilon_{-1}^{n} = \varepsilon_{1}^{n}; \varepsilon_{p,-1}^{\;\;n} = \varepsilon_{p,1}^{\;\;n}; \sigma_{-1}^{n} = \sigma_{1}^{n}; \sigma_{p,-1}^{\;\;n} = \sigma_{p,1}^{\;\;n}; v_{-1}^{n} = -v_{1}^{n} + 2v_{LB}^{n} \\ \varepsilon_{-2}^{n} = \varepsilon_{2}^{n}; \varepsilon_{p,-2}^{\;\;n} = \varepsilon_{p,2}^{\;\;n}; \sigma_{-2}^{n} = \sigma_{2}^{n}; \sigma_{p,-2}^{\;\;n} = \sigma_{p,2}^{\;\;n}; v_{-2}^{n} = -v_{2}^{n} + 2v_{LB}^{n} \end{cases} \tag{4.21}$$

where $(\varepsilon^{n}{}_{-1}, \varepsilon_p{}^{n}{}_{-1}, \sigma^{n}{}_{-1}, \sigma_p{}^{n}{}_{-1}, v^{n}{}_{-1})$ and $(\varepsilon^{n}{}_{-2}, \varepsilon_p{}^{n}{}_{-2}, \sigma^{n}{}_{-2}, \sigma_p{}^{n}{}_{-2}, v^{n}{}_{-2})$ are the strain, current critical strain, stress, current critical stress and velocity at nodes -1 and -2; v_{LB}^{n} is the velocity of the left boundary. Note that when traction boundary condition p(t) is prescribed at the left boundary v_{LB}^{n} needs to be evaluated first. To determine the value of v_{LB}^{n} corresponding to the applied pressure during time step n p^{n}, we consider the states of experienced by cell 1 (adjacent to the left boundary) during time step n. The cell is initially occupied with states $\vec{W}_1^{\,n-1}$=(v_1^{n-1}, σ_1^{n-1}) obtained from the last time step and is applied by a constant force p^{n} at the left boundary. Right running wave(s) form within the current time step and change the pre-wave (initial) states $\vec{W}_1^{\,n-1}$ to post-wave states $\vec{W}_1^{\,n}$=(v_{LB}^{n}, p^{n}), as shown in Figure 4.8. The value of v_{LB}^{n} can thus be computed for the given p^{n} and initial states $\vec{W}_1^{n-1}$ by

$$v_{LB}^n = f_R(p^n) \tag{4.22}$$

where function f_R is the same wave relation as defined by Equation 4.4, 4.6 or 4.8.

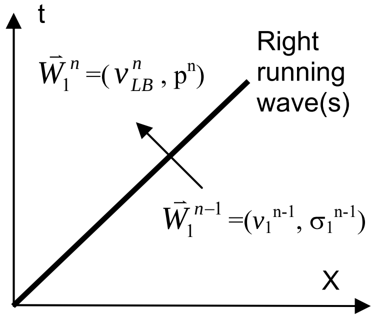

Figure 4.8: Left boundary conditions

4.5. Evaluation of the Numerical Scheme

The performance of the numerical scheme was evaluated using several simple loading conditions for which the exact solutions are available. The material parameters of the foam were equal to those shown in Figure 4.1. The initial density of the material, ρ_o and the initial critical stress of the material, σ_{po} were equal to 351 kg/m^3 and 2.16×10^6 Pa, respectively. The initial length of the foam, L=0.2 m which was discretized into N computational cells, where N=200. The foam bar was fixed at the right boundary and loaded at the left boundary. The time step was taken equal to 1.1849×10^{-6} s, the fastest wave speed was equal to 506.37 m/s (the linear wave speed c_E) and the CLF number was 0.6.

4.5.1. One Linear Wave Case

As shown in Figures 4.9 (a) and (b), a the initially unstressed foam is subjected to a constant load, $p_a = 2\times10^6$ Pa, which is less than σ_{po}. One right running linear wave traveling at velocity a_E = 506.4 m/s is expected, which produces a change in the state (0) (the initial state) with v_0=0, ε_0=0 and σ_0=0 to state (1) with v_1=11.253m/s, ε_1=0.0222 and $\sigma_1 = p_a = 2\times10^6$ pa. v_1 is computed from the linear wave relation for right running wave given in Equation 4.4. Figures 4.10 (a) and (b) give the velocity and stress along the foam bar at three distinct instants of time, t = 1.173×10^{-4} s, 2.358×10^{-4} s and 3.543×10^{-4} s. The results of the numerical computation and the exact solution are presented in the figures.

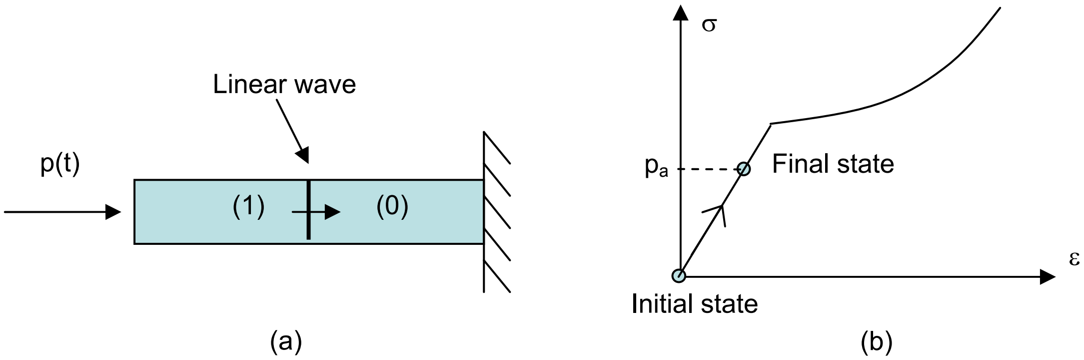

Figure 4.9: (a) schematic of waves in the foam and (b) loading history of the foam for the case of one right running linear wave.

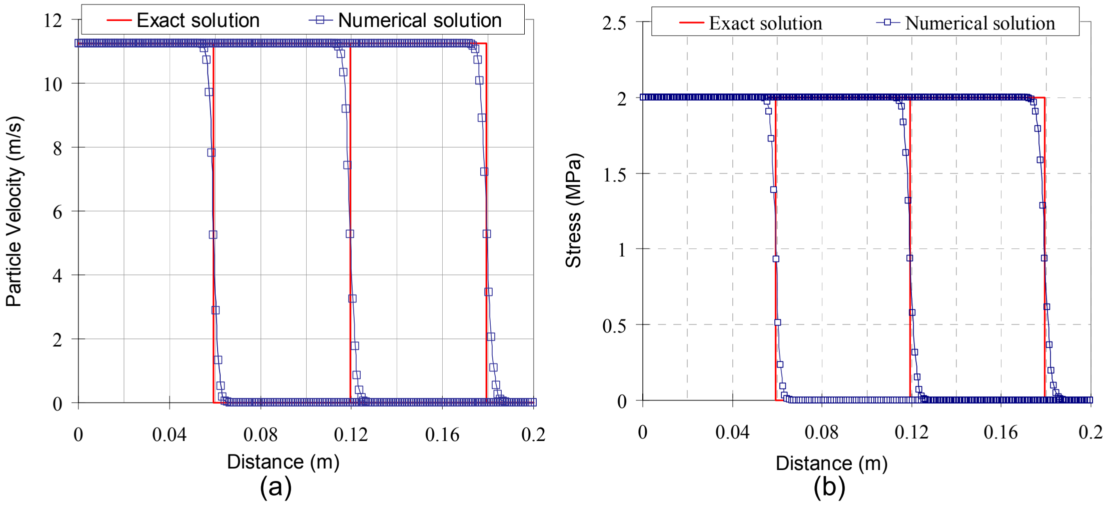

Figure 4.10: Comparison of numerical and exact solution for the case of one right running linear wave: (a) particle velocity and (b) stress.

4.5.2. One Compaction Wave Case

In this case the material is uniformly stressed to a value greater than σ_{po} and then shock loaded. To test the performance of the numerical scheme in dealing with a single compaction wave, the foam with initial stress $\sigma_o = 2.16\times10^6$ Pa $= \sigma_{po}$ is step loaded to $p_a=5\times10^6$ pa $> \sigma_{po}$, as shown in Figure 4.11 (a). The change in the stress state associated with the loading is shown in Figure 4.11 (b). A compaction front is generated at the loaded end of the foam and travels at a velocity, $s_R = 148.25$ m/s. The compaction front changes the initial state (0) with $v_0 = 0$, $\varepsilon_o = \varepsilon_{po} = 0.024$ and $\sigma_o = \sigma_{po} = 2.16\times10^6$ Pa to state (1) with $v_1 = 54.58$ m/s, $\varepsilon_1 = 0.3921$ and $\sigma_1 = p_a = 5\times10^6$ Pa. The velocities, v_1 and s_R are computed from the Hugoniot relation given in Equations 4.6 and 4.7. Figures 4.12 (a) and (b) show the velocity and stress, respectively along the foam bar at three distinct instants of time $t = 4\times10^{-4}$, 8×10^{-4} and 12×10^{-4} s. The results of the numerical computation and the exact solution are presented in the graphs.

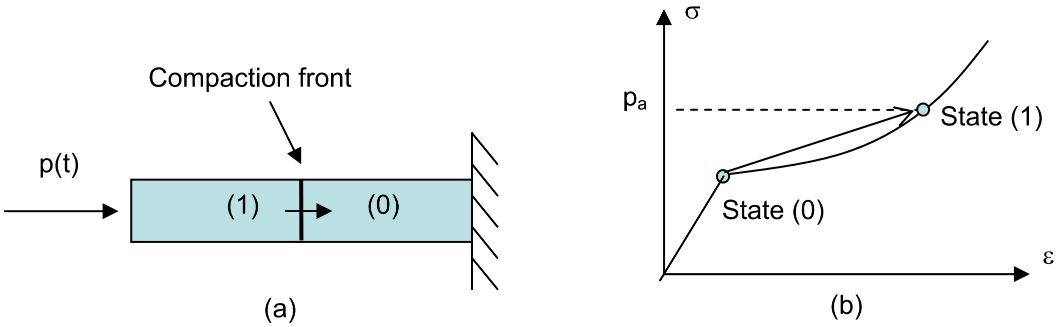

Figure 4.11: (a) schematic of waves in the foam and (b) loading history of the foam for the case of one right running compaction wave.

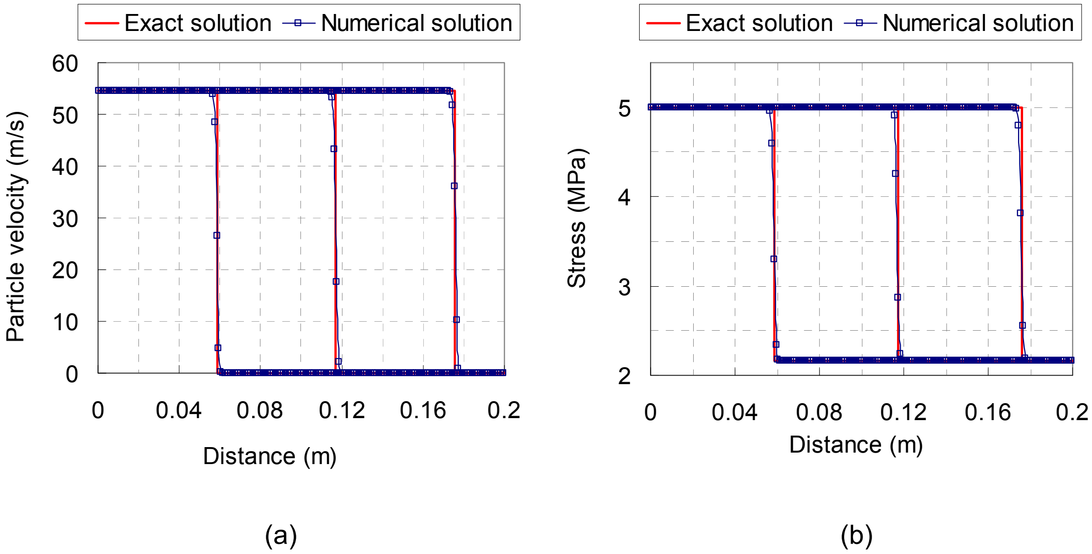

Figure 4.12: Comparison of numerical and exact solution for the case of one right running compaction wave: (a) particle velocity and (b) stress.

4.5.3. One Linear Wave and One Compaction Front Case

As shown in Figures 4.13 (a) and (b) the foam bar (initially unstressed) is subjected to a step load of magnitude $p_a=3.5\times10^6$ Pa > σ_{po}. Two waves are produced, as shown in Figure 4.13(a). One right running linear wave traveling at velocity $c_E = 506.37$ m/s, which changes the state (0) (the initial state) with $v_0 = 0$, $\varepsilon_0 = 0$ and $\sigma_0 = 0$ to an intermediate state

(1) with $v_1 = 12.15$ m/s, $\varepsilon_1 = \varepsilon_{po} = 0.024$ and $\sigma_1 = \sigma_{po} = 2.16\times10^6$ Pa. The linear wave is followed by a compaction front traveling at the velocity $s_R = 129.62$ m/s, which changes the state (1) to state (2) with v_2=41.60 m/s; $\varepsilon_2 = 0.251$ and $\sigma_2 = p_a = 3.5\times10^6$ Pa. Figure 4.14 (a) and (b) give the velocity and stress along the foam bar at three distinct points in time, t = 1.173×10^{-4}, 2.358×10^{-4} and 3.543×10^{-4} s.

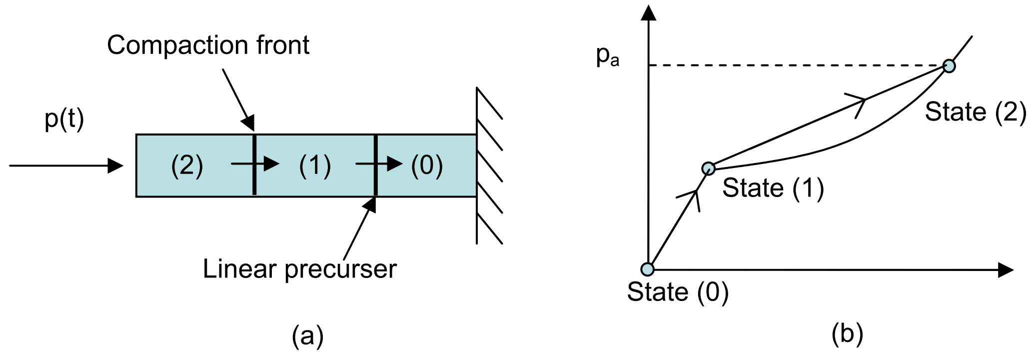

Figure 4.13: (a) schematic of waves in the foam and (b) loading history of the foam for the case of one right running linear wave and compaction wave.

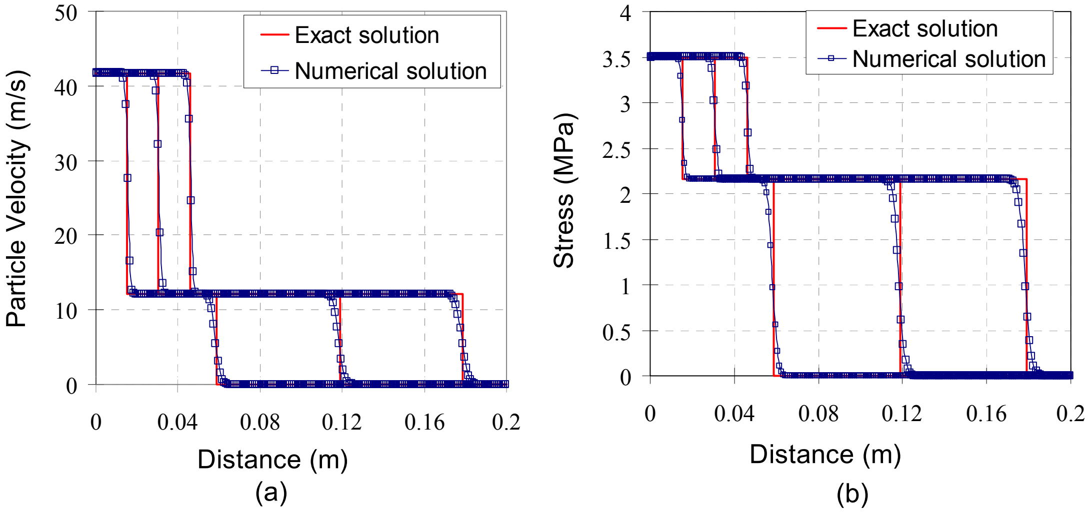

Figure 4.14: Comparison of numerical and exact solution for the case of one right running linear wave and compaction wave: (a) particle velocity and (b) stress.

4.5.4. One Linear wave, One Compaction Front Followed by Linear Unloading Wave Case

To test the performance of the numerical scheme in dealing with unloading, a step load, $p_{a1} = 3.5\times10^6$ Pa of duration 10.91 ms is followed by an unloading step load $p_{a2} = p_{a1}/3 = 1.167\times10^6$ Pa. The loading history is shown on the stress-strain curve of the material in Figure 4.15 (b). Three waves are produced in this load case, as shown in Figure 4.15 (a). One right running linear wave traveling at velocity $a_E = 506.37$ m/s changes the state (0) (the initial state) with $v_0 = 0$, $\varepsilon_0 = 0$ and $\sigma_0 = 0$ to state (1) with $v_1 = 12.15$ m/s, $\varepsilon_1 = \varepsilon_{po} = 0.024$ and $\sigma_1 = \sigma_{po} = 2.16\times10^6$ Pa. The linear wave is followed by a compaction front traveling at the velocity $s_R = 129.62$ m/s and changing states (1) further to state (2) with $v_2 = 41.60$ m/s; $\varepsilon_2 = 0.251$ and $\sigma_2 = p_{a1} = 3.5\times10^6$ Pa. Finally, the linear unloading wave travels at the velocity $a_E = 506.37$ m/s and changing state (2) to state (3) with $v_3 = 28.48$ m/s; $\varepsilon_3 = 0.225$ and $\sigma_3 = p_{a2} = 1.167\times10^6$ Pa. Figure 4.16 (a) and (b) give the velocity and stress along the length of the foam at a given time, $t = 3.554\times10^{-4}$ s. Both the numerical and exact solutions are presented in the figures.

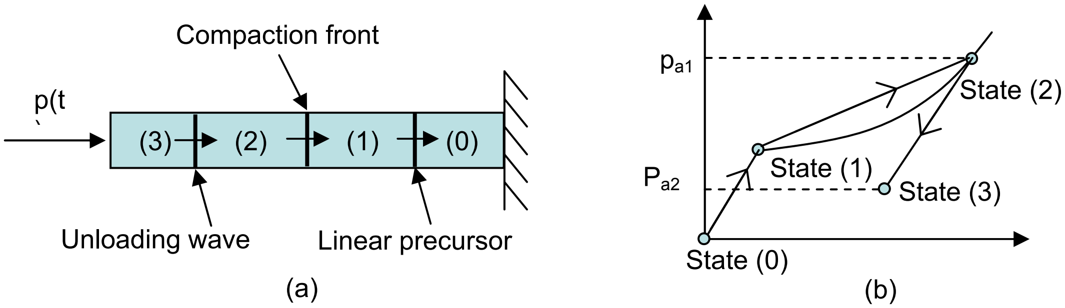

Figure 4.15: (a) schematic of waves in the foam and (b) loading history of the foam for the case of one right running linear wave and compaction wave followed by one linear unloading wave.

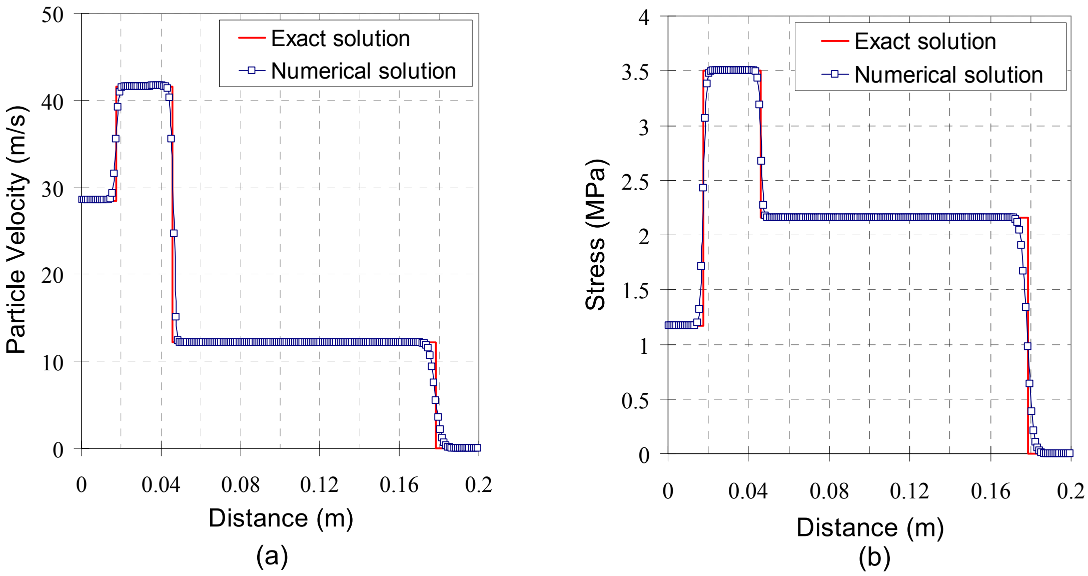

(a) (b)

Figure 4.16: Comparison of numerical and exact solution for the case of one right running linear wave and compaction wave followed by one linear unloading wave: (a) particle velocity and (b) stress.

4.6. Discussion of the Numerical Results

It can be seen that for all cases considered, the finite volume analysis using the Riemann solution provides an accurate prediction of the particle velocity and the stress profile within the bar. Since the applied step loads contain initial discontinuity, all the waves generated, either the linear wave or the compaction front, should also carry discontinuities at the wave fronts. It is interesting to note that the resolution of the compaction front appears better than the resolution of the linear waves; the compaction front is sharply resolved (3 cells) while the linear wave is smeared over 6 cells. This can be explained considering the two counteracting mechanisms, which control the resolution at the wave front. The first is associated with the numerical viscosity. The second order WAF scheme with TVD limiter has an embedded numerical viscosity, which suppresses non-physical oscillation but also produces a dispersion of the discontinuity [Toro 1999, p 452]. The second relates to the material stress-strain curve. Compression waves in the concave part of the stress-strain curve converge resulting in a less dispersed structure of a compaction front. This second mechanism only occurs on the compaction wave but not on the linear wave. Therefore, in the numerical simulation the linear wave develops a more dispersed structure.

It has been discussed previously that the structure of the Riemann problem in accordance with the typical material response of foam is not fixed, i.e. the number of waves (jumps) in the right or left side of the X-t plane is variable. However, in the implementation of the TVD version of the WAF scheme, a fixed structure of the Riemann problem is required at all cell interfaces. In the numerical scheme, WAF limiters defined by Equation 4.19 are used to suppress the non-physical oscillations. The limiter ϕ applies on each wave as shown in Equation 4.15 and is a function of the ratio r defined by Equation 4.18. The r is computed by comparing the change of a quantity q across a wave in the Riemann solution across one interface to the corresponding change in q across the corresponding wave in the Riemann problem for the adjacent interface. This requires finding corresponding wave structures at adjacent interfaces. In the implementation of the numerical scheme, multiple waves, if present in one direction, are replaced by a single fictitious wave to ensure the same wave structure at all interfaces. It is assumed that the single fictitious wave changes the initial (Region 1(left) or Region 3(right)) states to the final states in Region 2 (as shown in Figure 4.6). The velocity of the fictitious wave S can be computed using the Rankine-Hugoniot relationship which relates the wave velocity to the initial and final states on both sides of the fictitious wave. There are three different ways available to compute S.

The first choice is to calculate $S^{(1,2)}$ based on the initial and final stress and strain on both sides of the fictitious (left or right) wave. The absolute value is given in the following. Note that $S^{(1)}$ for the left wave has a negative sign and $S^{(2)}$ for the right wave has a positive sign.

$$\left|S^{(1,2)}\right| = \sqrt{\frac{\sigma_2 - \sigma_{3,1}}{\left(\varepsilon_2 - \varepsilon_{3,1}\right)\rho_o}} \tag{4.23}$$

The 2nd choice is based on the initial and final strains and particle velocities given as

$$\left|S^{(1,2)}\right| = \frac{v_2 - v_{3,1}}{\varepsilon_2 - \varepsilon_{3,1}} \tag{4.24}$$

The 3rd choice is based on the initial and final stresses and particle velocities given as

$$\left|S^{(1,2)}\right| = \frac{\sigma_2 - \sigma_{3,1}}{v_2 - v_{3,1}} \tag{4.25}$$

It should be noted that Equations 4.23-4.25 result in identical values when there is only one left or right running wave in the solution of Riemann problem (either linear elastic wave or compaction front). However, when elastic and compaction front co-exist, three different wave are generated and $a_E > S > s$ holds for all three equations.

The test case in Figure 4.14 contains two right running waves in the domain and the numerical results were obtained using Equation 4.23. To show the influence of S (given by Equations 4.23-4.25) on the numerical solutions, the numerical results for this case obtained with Equation 4.24 and 4.25 are also shown in Figures 4.17 and 4.18, respectively. There are significant oscillations close to the loaded end when Equations 4.24 and 4.25 are used, which are not present when Equation 4.23 is used.

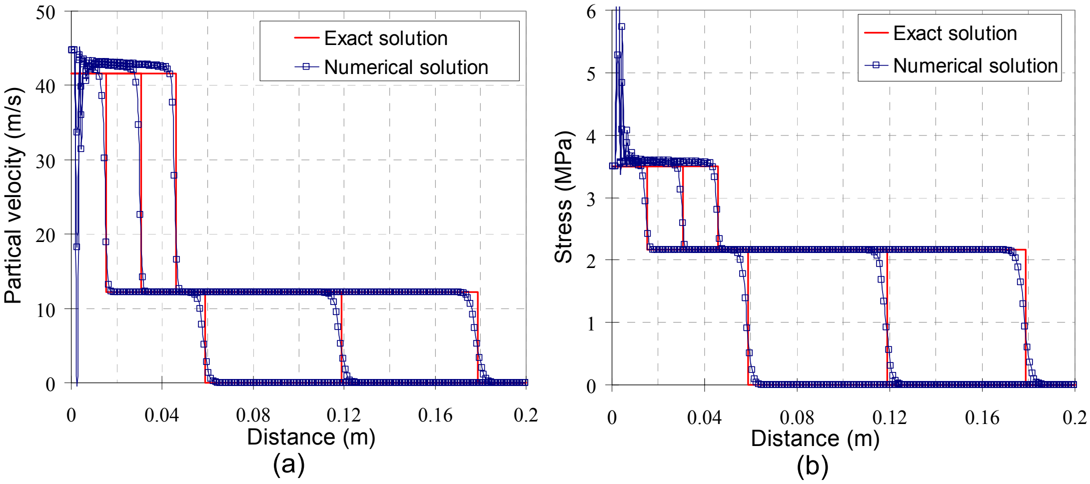

Figure 4.17: The numerical results based on wave velocity $c_{1,2}$ evaluated using Equation 4.24.

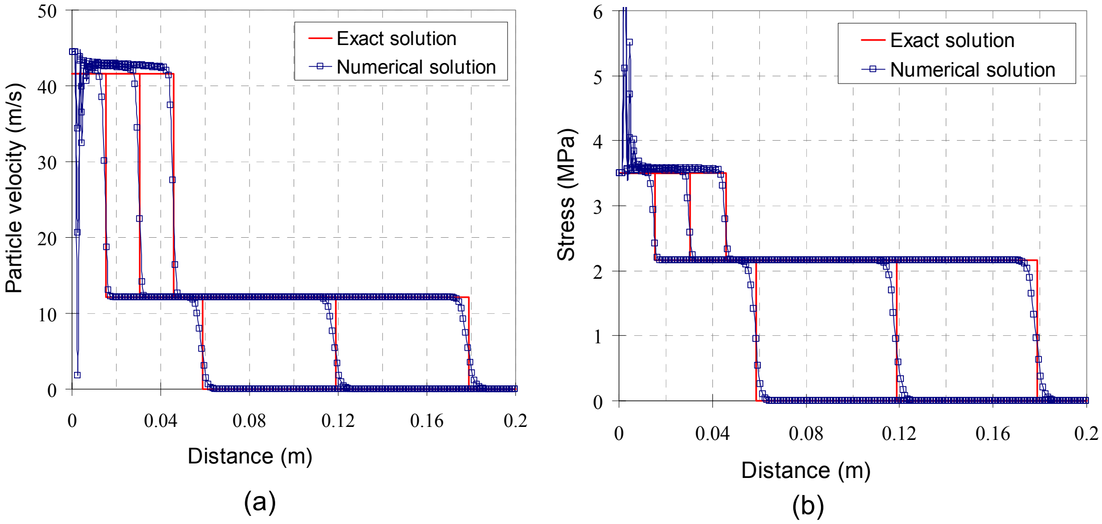

Figure 4.18: The numerical results based on wave velocity $c_{1,2}$ evaluated using Equation 4.25.

4.7. Foam Bar Subjected to Transient Loading

The ability of foam to damp out an intensive transient loading from a solid impact or blast pressure wave makes it suitable for use in developing protective devices. The finite volume implementation with the local Riemann solution can now be used to predict the response of foam and the transmitted stress to the solid substrate due to such loading. The solution from Riemann solver was first evaluated using the available data for foam subjected to solid impact and then used to evaluate the response of foam subjected to a blast pressure wave.

4.7.1. Foam Bar Subjected to a Solid Impact

Test data on the impact response of Aluminum foam has been reported [Nemat-Nasser et al. 2007] and was used for evaluating the numerical implementation of the local Riemann solver. In the experiment, the sample made from Aluminum foam was impacted by a solid projectile and the stress transmitted through the sample was measured using an instrumented Hopkinson bar facility. The foam bar, 76.2 mm in length was impacted by a solid impacter weighing 1.46 kg traveling with a velocity equal to 52.6 m/s. The quasi-static engineering stress-engineering strain curve of the aluminum foam (Duocels Aluminum Foam Alloy 6101, nominal density = 258 kg/m^3, 40 ppi) is shown in Figure 4.19. The stress- strain curve was fitted using Equation 4.1 with E=200 MPa, A=0.017, α=2.5, ε_{po}=0.014 (which gives σ_{po}=2.8×10^{6}pa) as shown in Figure 4.19.

A finite volume implementation of the aluminum foam loaded by the solid projectile at left boundary and fixed at right boundary was developed. The projectile was modeled as rigid body. The motion of the rigid body is described by the Newton's second law of motion. At the left boundary (the interface between projectile and aluminum foam), the continuity of velocity and stress was implemented in a staggered manner. At the beginning of each time step, the velocity of projectile was prescribed as the velocity boundary condition (at the left boundary) for the foam. The solution of foam is then advanced. At the end of each time step, the motion of projectile was updated using the Newton's second law of motion with the applied force corresponding to the stress at the left boundary of the aluminum foam. Foam bar was discretized into 50 cells and the CFL number was set to 0.6 in the numerical simulation.

A comparison of numerical and experimental results of the stress transmitted through the foam specimen is shown in Figure 4.20. It can be seen that the finite volume implementation with the local Riemann solution provides a favorable prediction of the transmitted stress history. The initial rise in the transmitted stress is due to the reflection of the leading linear wave at the right boundary and corresponds to crushing strength of the aluminum foam, which is not related to the initial velocity of the projectile. The stress history following the initial elastic wave is associated with the compaction front, which produces crushing of the microstructure. The compaction front creates an interface between the crushed and uncrushed cells. The material in the wake of the compaction front is densified. The subsequent jumps in stress following the first rise are due to the multiple reflection of the stress wave travelling in the densified material at the right boundary.

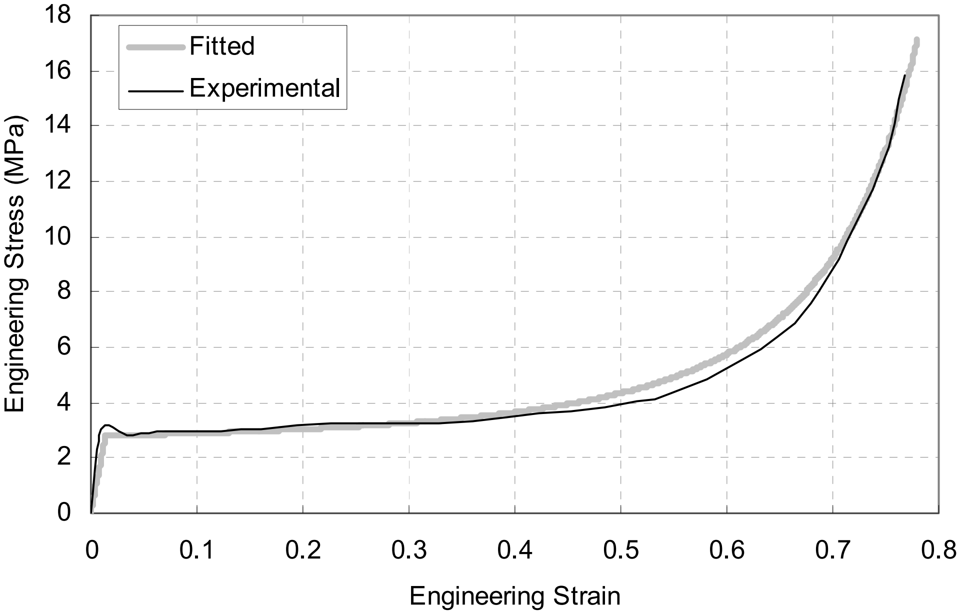

Figure 4.19: Engineering strain–engineering stress curve for the Duocels Aluminum foam (40 ppi, nominal density=258 kg/m^3)

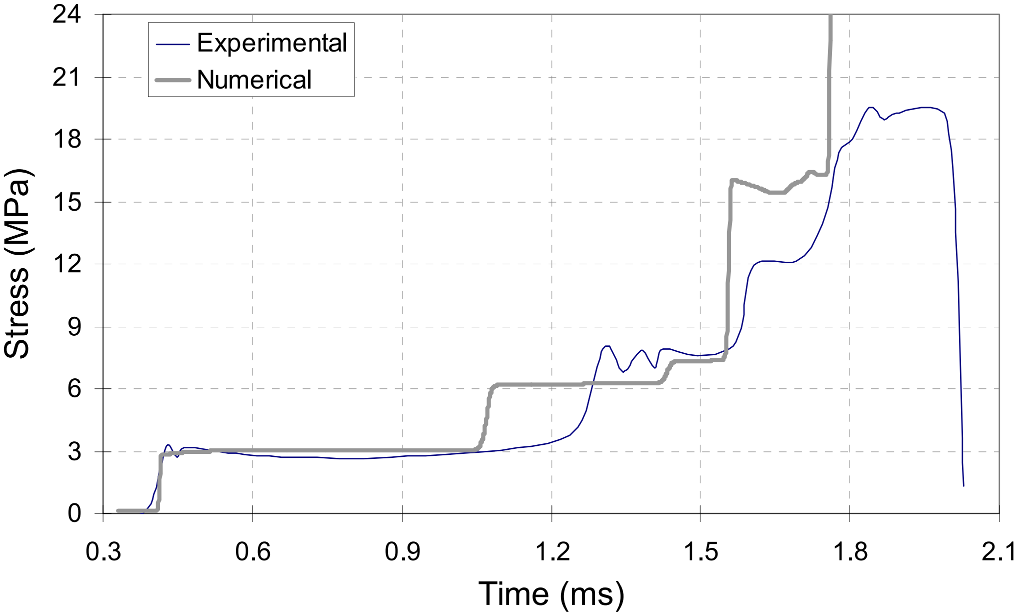

Figure 4.20: Transmitted stress history for the foam specimen impacted with a 1.46 kg projectile traveling at 52.6 m/s.

4.7.2. Foam Bar Subjected to a Blast

An air blast is generated by a sudden release of energy (from explosive source) and is associated with an abrupt increase of pressure followed by a rapid decay of pressure. The blast pressure wave typically lasts for few milliseconds. The blast load is often treated as a triangular pulse in practice, characterized by the peak pressure p_b and duration t_b. Blast pressure waves with pressure amplitude, $p_b = 1.5\times10^7$pa and three different durations, $t_B = 2.5\times10^{-4}$ s, 2.0×10^{-4} s and 1.5×10^{-4} s, were considered for analysis (Figure 4.21). It should be noted that the blast pressure waves, with the same amplitude and different durations are associated with different impulse. Finite volume analysis was performed considering foam with prescribed pressure history at the loaded end. The stress-strain response of the foam shown in Figure 4.1 was used in the numerical study. The applied pressure is expected to produce a compaction front in the foam bar. The propagation of the stress waves inside the foam bar is illustrated in Figures 4.22(a) and (b) for the incident blast pressure wave with $t_B = 2.5\times10^{-4}$ s. The stress induced in the foam bar at a successive instants of time starting at t = 0 s and ending at $t = 3.78\times10^{-4}$ s at time increments of 3.78×10^{-5} s are plotted in Figure 4.22(a) and starting at $t = 4.54\times10^{-4}$ s and ending at $t = 7.95\times10^{-4}$ s are plotted in Figure 4.22(b). The wave structure in the foam comprises of an elastic precursor followed by a compaction front. A decrease in the maximum stress associated with the compaction front is evident as the stress wave propagates in the foam. There is also a change in the shape of the stress pulse as it propagates in the foam. The amplitude of the compaction front decreases to a stress of amplitude equal to σ_{Po} as the compaction front propagates into the foam, resulting in a longer stress pulse. The stress transmitted to an elastic substrate from the foam for the three incident blast pressure waves is shown in Figure 4.21. Comparing with the applied blast pressure at the loaded end, there is clearly a decrease in the amplitude of the stress transmitted to a substrate when the blast wave arrives at the target end. This illustrates the benefit of using foam in attenuating the blast pressure amplitude; the amplitude of the stress pulse transmitted into the elastic substrate is significantly smaller than the applied blast pressure amplitude. There is significant dissipation produced by a compaction front associated with dynamic compaction which is associated with the area enclosed by the shock cord (Raleigh line in the stress-strain curve) as is illustrated in Figure 4.23. It is interesting to note that there is no change in the transmitted impulse associated with the stress wave after attenuation. The results indicate that while the foam will attenuate the stress amplitude of the incident blast pressure wave, it does not change the total momentum transferred to the substrate.

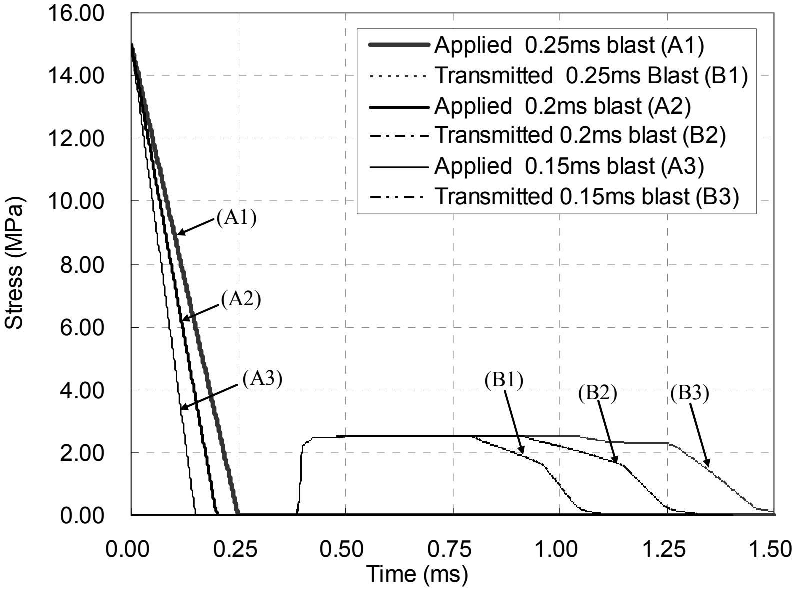

Figure 4.21: Time history of the applied blast pressure and transmitted stress.

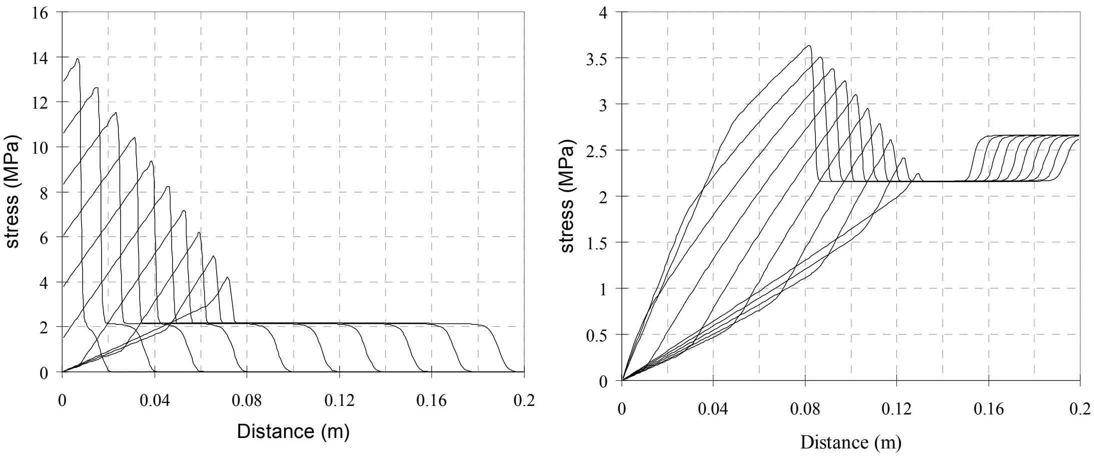

(a) (b)

Figure 4.22: Stress induced in the foam bar at a successive time between (a) t=0~0.378ms and (b) t=0.454~0.795ms.

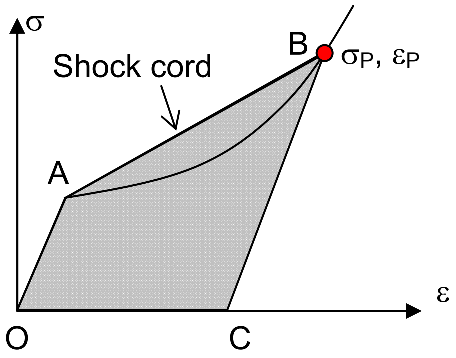

Figure 4.23: Energy dissipation associated with shock compaction in the foam.

The results presented here show that foam can be used for attenuating the incident blast pressure wave. The dissipation of energy achieved at the expense of irreversible compaction of the microstructure of foam would result in an attenuation of the amplitude of the stress wave produced in the foam. The results of the analysis indicate that brittle and metallic foams can be used for mitigating the stress amplitude of applied transient loading.

The characteristics of the foam can be tailored to achieve the required level of protection for a given incident blast.

4.8. Summary and Conclusions

A numerical procedure for predicting the dynamic compaction of brittle and metallic foams due to the propagation of finite disturbance associated with shock-type characteristics was developed. These characteristics describe the motion of an interface in reference to the initial undeformed specimen which separates crushed and uncrushed dells during a process of a cascading cell-crushing similar to a domino effect. The major difference between the present shock-type behavior and a classical shock wave is the permanent deformation of the crushed cells which is irreversible in the sense that the application of an extensive load will not bring the material back to its initial state whereas the passage of an expansion fan through a compressed by a moving shock wave gas can reduce the pressure back to its initial level.

A finite volume implementation of the hyperbolic conservation equations in a Lagrangian frame of reference has been developed which is capable of predicting the propagation of a precursor elastic wave and a compaction front in the form of a finite disturbance associated with a shock-type structure. For the first time exact Riemann condition were implemented in these formulations to predict the physics of the elastic and compaction waves propagating in foam materials undergoing dynamic compression.

It was found that the Second-Order TVD version of WAF scheme based on the exact solution of the local Riemann problem gives accurate solution for the propagation of both waves and leads to irreversible dynamic compaction of brittle and metallic Foams.

The numerical scheme was evaluated through comparisons with theoretical data obtained from closed form solutions of test cases with simple loading.

The experiment of Nemat-Nasser et al. (2007) was simulated by using the present model with very satisfactory results.

Finally the effects of blast loading on foams were simulated. The numerical results suggest that the foam is able to transform an intensive blast loading into a flat rectangular shaped loading. An attenuation of transmitted stress was predicted which is associated with compaction of the foam.

Chapter 5: Dynamic Compaction of Cement Foam Subjected to Blast Load: Experimental Investigation and Theoretical Development

5.1. Introduction

Foams possess excellent energy-absorbing properties and are widely used as protective materials in applications such as improving crash worthiness [Tan et al. 2005a, Gibson and Ashby 1999]. The successful use of these materials in mitigating impacts has drawn the attention of structural community towards the development of blast mitigation strategies. Structural elements made of concrete or masonry, are especially susceptible when subjected to a blast loading of high amplitude. The stress wave induced by the blast loading may cause severe material damage resulting from crushing, cracking or spalling, before there is any noticeable displacement of the structural element. It is believed that foam when placed in the path of an incoming blast pressure wave would alter the blast wave characteristics and reduce the stress transferred to the structural element. Blast mitigation using foam is an emerging field and there is limited data on the blast response of foams. The available information in the literature is sparse and not very consistent. Some experimental evidence and results from numerical simulations suggest the possibility of stress enhancement, rather than mitigation, in the substrate material when foam is placed in front.

The pressure enhancement by foams was first reported by Monti [1970]. Monti's work focused on the strength of a planar the shock wave reflected off the front face of a flexible porous material but it was shown that the transferred pressure at back wall could exceed the pressure obtained without the porous material. These findings were later confirmed by experimental studies on the interaction of shock waves with very low density flexible polymeric foams; from polyurethane foam [Ben-Dor 1994 and Gvozdeva 1985**]** and using open-celled polymeric foams [Skews 1991 and 1993]. The polymeric foams used in these experiments typically had very high porosities (in the range of 90% and higher) and were able to rebound after the loading was removed. Pressure gauges placed at the back end of the foam sample were used to record the transmitted pressure through the foam. The transmitted pressure compared to the reflected pressure with no foam present showed a significant pressure enhancement. The experimental observation of Skews [1991] was later supported by the numerical simulation by Baer [1992] and Olim [1994].

The head-on collision of a planar shock wave with an open-celled, rigid porous material was investigated experimentally by Levy et al. [1993]. Experiments with the use of metallic (Alumina matrix) and brittle (Silicon Carbide matrix) foams were confined to studying the response at shock pressure amplitudes which do not produce significant deformation of the solid skeleton. This study was limited to understanding the change in the characteristics of the pressure wave upon transmission through the porous matrix. In a recent study, similar results were also obtained using aluminum foams of high porosity which were subjected to air shock [Wahid et al. 2010]. From an experimental program where the magnitude of the shock produced insignificant deformation of the porous material, it was shown that the transmitted stress to an elastic substrate exceeds the stress magnitude obtained from direct shock wave incidence on the substrate.

The available experimental evidence clearly indicates that both flexible polymeric and rigid aluminum foams produce pressure enhancement when subjected to shock loading. It should be noted that all the results in the literature were obtained for shock loading where a shock front is followed by constant pressure. Such loading is associated with an infinite impulse and energy input. Loading associated with a blast pressure wave, however, has a decaying profile, which follows the sudden pressure rise produced by the shock front. Blast pressure loading is of finite duration associated with a finite impulse input. Therefore, extension of the findings from shock loading to the case of transient loadings with finite impulse is not yet clear. Limited results on stress amplification by soft foams for blast loading are available. In a study on the thoracic visceral injury from blast loading, Cooper et. al. [1991], found that the transmitted overpressure from air to the anechoic water chamber is enhanced significantly by a foam layer. Experimental results on animals showed an increase in the severity of lung injury when foam was used as a protective layer. The results indicated that a soft foam layer attached to armor may produce a higher level of damage in the protected object.

The results for metallic and brittle foams, which undergo irreversible compaction, subjected to transient loading of finite impulse are also not clear. The experimental results on the use of metallic foams obtained from studies involving impact have shown the benefit of using foam in providing energy dissipation [Tan et al. 2005a and b, Reid and Peng 1997]. It should however be noted that there is a fundamental difference in the nature of loading associated with impact and blast pressure. In an impact, the energy delivered to a solid substrate by a projectile travelling at a given velocity, is a fixed value but the stress transmitted at the interface can vary depending on the materials in contact. Whereas, for blast, the loading history produced by an incident blast wave at different solid substrates is always the same (neglecting the effect of the fluid solid interaction) but, the energy transferred to the solid substrate varies depending upon the stiffness of the substrate (larger for softer material) [Subramaniam et al. 2009, Nian et al. 2010].

Experiments involving blast loading with the use of metallic and brittle foams have been confined to studying the interaction at blast pressure amplitudes which do not produce any significant deformation of the solid skeleton [Standley et al. 2002, Levy et al. 1993, Levy et al. 1995, Ben-Dor et al. 1994]. These studies were limited to understanding the change in the characteristics of the pressure wave upon transmission through the porous matrix. Experimental results on the blast response of aluminum foam panels, which undergo compaction were presented by Hanssen et al. [2002]. Foam panels were attached to the front face of a target steel plate. The steel plate in turn was attached to a pendulum. The blast pressure wave obtained from an explosive charge was used. While the predictions of transmitted stress considering irreversible compaction of the material indicated a decrease in transmitted pressure to the face of the pendulum, these could not be verified since the applied blast pressure and the pressure transmitted to the substrate were not measured in the experiments. Further, the experiments showed that the addition of the foam panels increased the energy and impulse transferred to the pendulum. This counter-intuitive behavior was attributed to the geometric effect associated with the continuous change in the shape of the initially plane panel surface into a double-curved shape.

Therefore, both the successful use in mitigating impact using foams which undergo irreversible compaction [Tan et al. 2005a and b, Reid and Peng 1997] and the available information on the pressure enhancement caused by shock loading in rigid foams and highly porous flexible foams which rebound [Monti 1970, Ben-Dor 1994, Gvozdeva 1985**,** Skews 1991 and 1993, Baer 1992 and Olim 1994] do not provide sufficient indication about the application of foam in mitigating blast loading. The blast test results available in the literature [Cooper et. al. 1991 and Hanssen et al. 2002] are also not helpful since the stress transmitted from the foam to the solid substrate, which is critical to understand the behavior of foam in blast mitigation, were not measured. Careful experiments on blast response of foams obtained from experiments with well defined input blast pressure waves, which would lead to a fundamental understanding of the behavior of foam, are currently not available.

In this study, an experimental investigation of the one-dimensional dynamic response of cement foams subjected to blast pressure loading was conducted. A shock tube was used to generate controlled blast pressure loading of different amplitudes and durations. Instrumentations for measuring the blast pressure history applied at the front end (loaded end) of the foam and the stress transmitted to a solid substrate through the foam (transmitted stresses) were developed. Cement foams of different densities and different lengths were evaluated for different blast pressure loadings. The deformation of the cement foam bars after application of the blast pressure loading was also recorded. Finally, the experimental data was used to evaluate the predicted response obtained from numerical simulations.

5.2. Experimental Setup

A shock-tube with an instrumented short rod was developed for investigating the blast response of foams. A schematic sketch and a photograph of the test facility are shown in Figure 5.1. The shock tube was used to generate a blast pressure wave with the required amplitude and duration. A sample made of cement foam was attached in front of an instrumented short rod and subjected to blast pressure loading. The instrumented short rod was used to measure the transmitted stress from the foam. Pressure transducers were installed in the shock tube along the path of the blast pressure wave to measure the applied pressure. Experiments were performed to determine the following: (a) the transmitted stress to a solid substrate as a function of the applied blast pressure loading; and (b) the deformation of cement foams due to loading from the blast pressure wave.

5.2.1. Shock tube for generating blast pressure waves

The shock tube consists of a high pressure section (driver section) which is separated from the low pressure section (driven section) by a diaphragm. The shock tube has a circular cross-section and is entirely made of stainless steel. The driver section is 1.3 m in length and the inner and outer diameters are equal to 8.9 cm and 12.6 cm, respectively. The driver section is fitted with a screw driven piston at the back end, which allows for varying the length of the pressurized part of the driver section. The back flange of the driver section is fitted with a threaded rod through its center, which is attached to a steel cylinder with a diameter equal to 8.9 cm. Grease is applied in the gap between the steel cylinder and the inner surface of the driver section to allow smooth motion of the cylindrical piston and to seal any gaps between the inner surface of the driver section and the cylindrical piston. The driven section is 3.3 m in length and the inner and outer diameters are equal to 4.5 cm and 7.2 cm, respectively. Pressure ports are machined at different locations along the length of the driven section for mounting pressure transducers. Pressure transducers are placed flush with the inner surface of the tube. The driven section (4.5 cm diameter) is connected to the driver section (8.9 cm diameter) with a 20 cm long nozzle. The diameter decreased smoothly from 8.9 cm to 4.5 cm over the length of nozzle. The nozzle was used to accelerate and increase the Mach number of the flow.

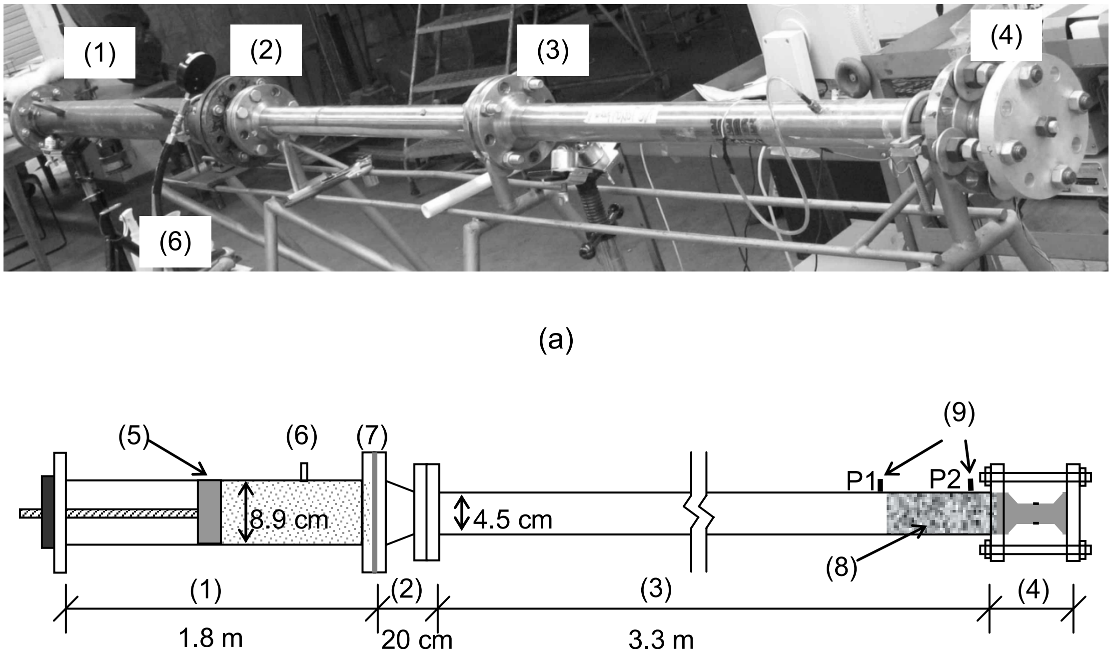

(a)

(b)

Figure 5.1: Shock tube test facility: (a) photo and (b) schematic diagram. 1) driver section; 2) nozzle; 3) driven section; 4) instrumented step rod; 5) screw-driven piston; 6) high-pressure gas inlet; 7) diaphragm; 8) specimen; 9) pressure transducers.

In a typical shock tube, the pressure wave is generated by the rupture of a diaphragm which is pressurized on one of its faces. The propagation of the different waves after the rupture is usually presented using an X-t diagram, as shown in Figure 5.2. In a typical shock tube arrangement, shock waves are generated by the sudden rupturing of a diaphragm as the pressure difference between the driver and the driven sections reaches a critical value. A compression wave generated by the sudden rupture travels downstream into the driven section and rapidly steepens to form a shock front. Simultaneously, a set of rarefaction (expansion) waves travel back into the driven section, reflect at the back end of the driven section as rarefaction waves and travel downstream in the same direction as the incident shock wave. According to Prandtl's relation, the sum of the particle velocity and local wave speed in the post shock flow is higher than the shock wave speed [Courant and Friedrichs 1999]. Thus, the sound speed at which the disturbance propagates in the post-shock flow is higher than the shock wave speed. When the reflected rarefaction waves, which travel faster than the shock front, catch up with the shock front, a blast pressure wave is generated. An incident blast wave consists of a leading shock front immediately followed by expansion waves, resulting in a decreasing pressures profile. The parameters, such as, the amplitude and the duration of the blast wave at the end of the driven section can be controlled by varying the lengths of the driver and the driven sections and the pressures inside each section. A computer program, which allows for predicting the pressure history of an incident blast wave at the target end of the shock tube has been developed.

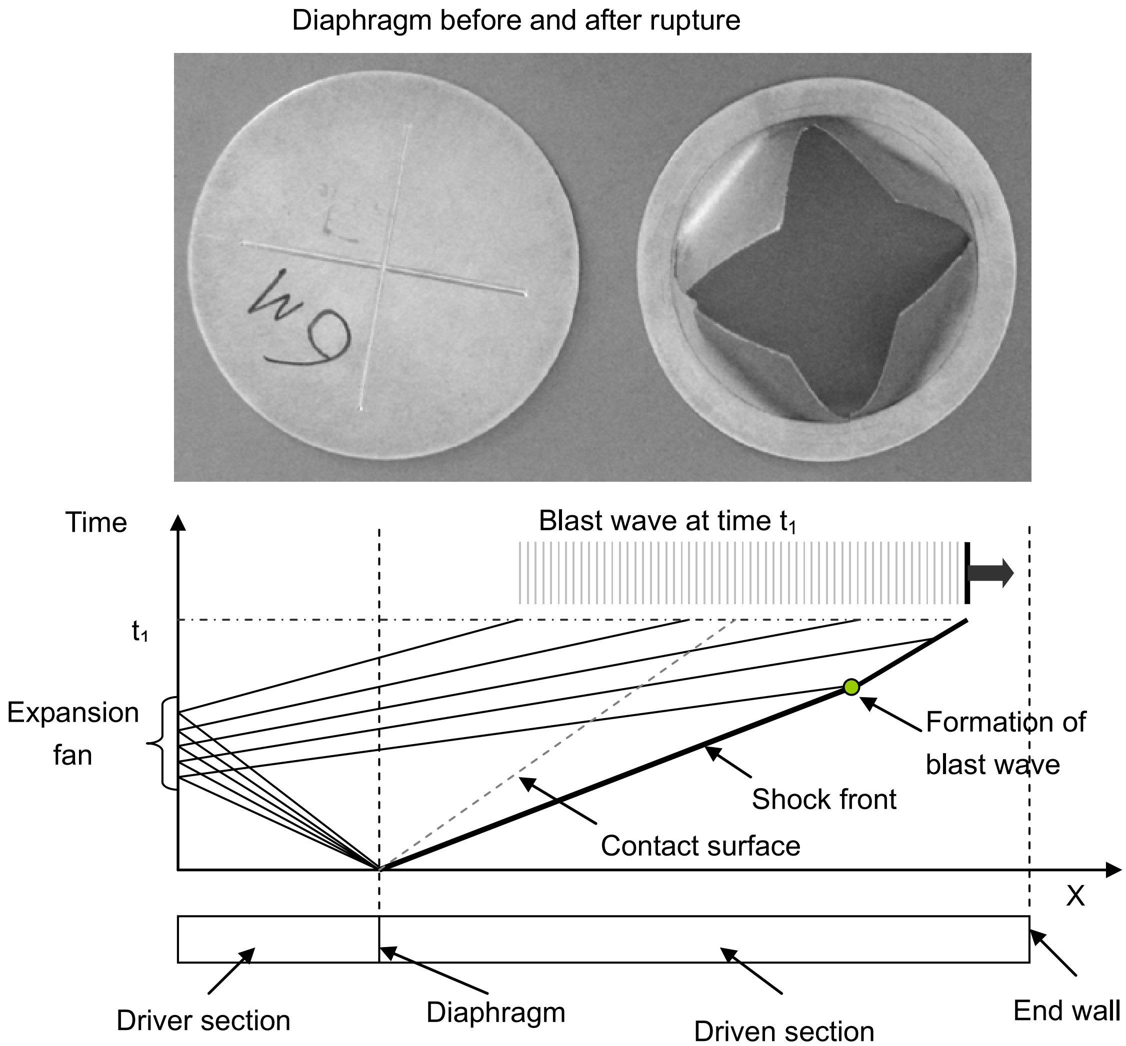

Figure 5.2: Formation of a blast pressure wave in the shock tube

Notches were machined on one of the faces of the diaphragm to ensure that it opened completely upon rupture. The initial pressure in the driver section at which the diaphragm ruptures can be controlled by varying the thickness of the diaphragm and the depth of the notch. Diaphragms made of Aluminum 6061-T6 with two perpendicular notches which intersect at the center, were used. The thickness of the diaphragm was equal to 1.6 mm and notches with different depths ranging from 0.8 to 1 mm were machined to obtain blast pressure waves with different amplitudes. Photographs of typical diaphragms before and after rupture are shown in Figure 5.2. The length of the driver section was adjusted by moving the piston within the driver section, to obtain the desired blast pressure characteristics. Compressed Helium was used for the high pressure gas in the driver section as it produces blast pressure waves of shorter duration when compared to air (or nitrogen). Pressure loading produced by the blast wave was measured using pressure transducers, placed close to the target end in the driver section of the shock tube. Different blast loads with pressure amplitudes ranging from 0.5 to 1.5 MPa and duration in the order of several ms were generated. It should be noted that the exact composition of the Helium-air mixture in the driver section is not needed to be determined since the blast impulse was obtained experimentally.

The shock tube facility provides an unprecedented platform to study and evaluate the blast response of materials. The ability to control the pressure associated with the blast waves allows for a fundamental evaluation of the blast response of foams and also the determination of the material properties under high rates of loading. Such a facility offers a significant advantage in conducting blast studies when compared with the conventional methods which employ uncontrolled blast source from an explosive charge. In addition, the use of a shock tube allows for evaluating the material behavior without the interfering effects of debris.

5.2.2. Setup for measuring transmitted stress

An instrumented short rod with a stepped diameter was used for measuring the transmitted stress. The strain measured from the surface of the rod was related to the stress applied on the face of the short rod. This is similar in principle as the technique to measure transmitted stress from transient loading in the conventional split Hopkinson pressure bar (SHPB) [Kaiser 1998]. A stepped rod, where the diameter of the rod at the location of strain measurement is reduced, provides a higher sensitivity (hence better signal to noise ratio) in measurements [Tan et al. 2005a]. A short rod was used to overcome the limitation of length in the conventional Hopkinson pressure bar arrangement. In the conventional setup, the length of the pressure bar determines the useful duration of the signal. The maximum duration of the applied stress is limited by the time for reflection of the transmitted wave from the back end of the rod. For recording blast pressure signals with durations on the order of 10 ms, the length of the rod required in such a setup would be excessive (on the order of tens of meters) and hence, impractical.

In the short stepped rod, multiple reflections of stress waves form both ends and at the edges would occur within the duration of an applied stress pulse and the stress at a given location would be the result of superposition of the applied stress pulse and the reflected waves. The reflected waves would produce oscillations in the measured stress on a time scale associated with the time of travel for the waves over the length of rod. For a short rod, the time scale associated with the oscillations can be made significantly smaller than the time scale associated with the applied loading. In this case, the applied pressure can be separated by filtering the high frequency variations associated with the wave reflections.

In the experimental setup, the overall length of the instrumented short rod was selected such that the time scale associated with the oscillations was on the order of 10-100 μs, while the blast pressure duration was in the range of 10 ms. The diameter of instrumented short rod was decreased from 44.5 mm at the loaded end to 19.2 mm at the measuring locations. The validity of using measured strain from the short instrumented short rod by separating the contributions of the oscillations produced by reflections was confirmed using numerical simulation. In addition, the instrumented rod was calibrated against applied blast pressure signals. The transmitted stress recorded by the instrumented short rod when a blast wave is directly applied on the face of the rod was used for this purpose.

A schematic sketch of the instrumented short rod is shown in Figure 5.3. The instrumented short rod can freely slide inside the driver section of the shock tube and is fixed to a large aluminum plate at the other end. The aluminum plate is connected to the end flange of the shock tube using four threaded bolts. The sample to be tested rests against the face of the short rod. Four strain gages are placed 90 degrees apart around the perimeter in the middle of the short rod. To reduce the influence of the bending effect, misalignment of the fixture and unsymmetric loading, the average of the four strain gages was recorded.

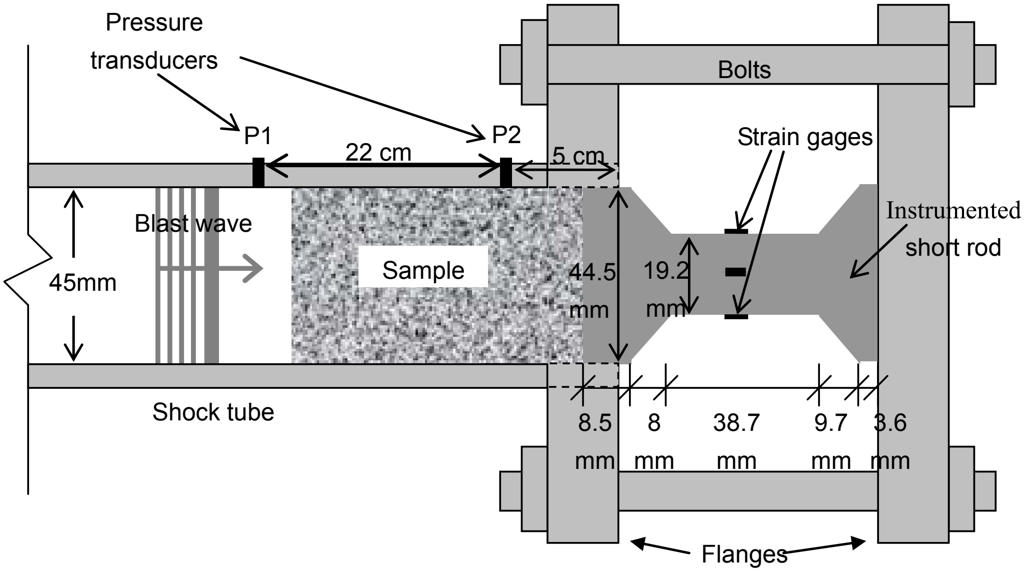

(a)

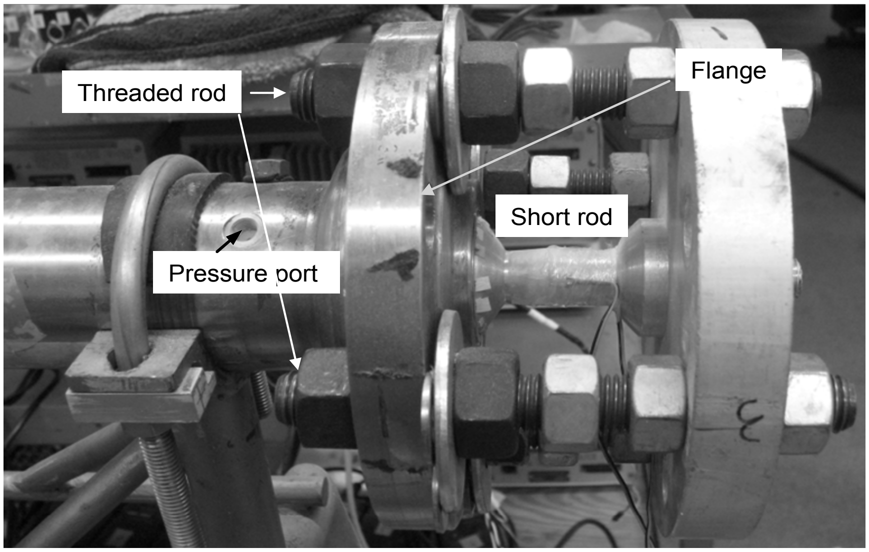

(b)

Figure 5.3: (a) Schematics and (b) photo of instrumented short rod.

5.2.3. Sensors and Instrumentation

The sensors include pressure transducers and strain gages. The instrumentation comprises of data acquisition system(s) for digitizing pressure and strain signals, amplifiers, filters, and power supplies for operating pressure transducers and strain gages. The data acquisition system for collecting the strain and pressure measurements consists of four NI-PCI-6120 A/D boards which are integrated into a PC and additional circuitry to synchronize the A/D boards. The sampling frequency was set to 625 kHz. Low-noise voltage pre-amplifiers with continuously adjustable gain (EG&G PARC pre-amplifier/filter, Model 5113) were used for signal conditioning before the signal is sent to A/D boards. For both the pressure and strain gage signals, the LF(low frequency) roll off was set to FLAT and the HF (high frequency) roll off was set to 6 dB/octave. For the pressure sensors the input was set to differential with AC coupling and a 10 s time constant, while for the strain gages the input was set to Single-ended with AC coupling and 10 s time constant.

Semi-conductor strain gauges were used because of the small physical size (active length : width :thickness = 0.84 mm : 0.2 mm : 0.01 mm), which makes close to point measurements of strain possible. The strain gauges are mounted on a flexible insulated circuit with versatile solder pads for easy installation. Additionally, these gauges offer significant advantages over conventional foil gauges, such as, high sensitivity (50 to 75 times greater than foil gages), high frequency response (can be used for transient and high frequency phenomena), overall accuracy (better than ±0.10%), and moderately temperature sensitivity.

A constant current, battery-operated power supply circuitry was used to provide the excitation to the strain gauges (each strain gauge receives a 0.6 mA current). Figure 5.4 shows a schematic of the circuitry for powering the strain gauge. A constant current circuit was used because it is most effective for dynamic strain measurement. In a dynamic measurement, only the time varying component of the output (V_{OUT}) produced by a change in the resistance of the strain gage (R_g) needs to be measured. Effects such as changes in lead resistance due to temperature variations would be rejected. Using this configuration, temperature drifts become nearly negligible [Dongen, 2007].

XCL-072 Kulite differential pressure sensor was used in the experiments for measuring the variation of air pressure, and to obtain the time history of the applied pressure. The sensor has a diameter of 0.81 mm and a natural frequency of 240 kHz. A circuitry operated by a constant-current, power supply was used for exciting the pressure sensors.

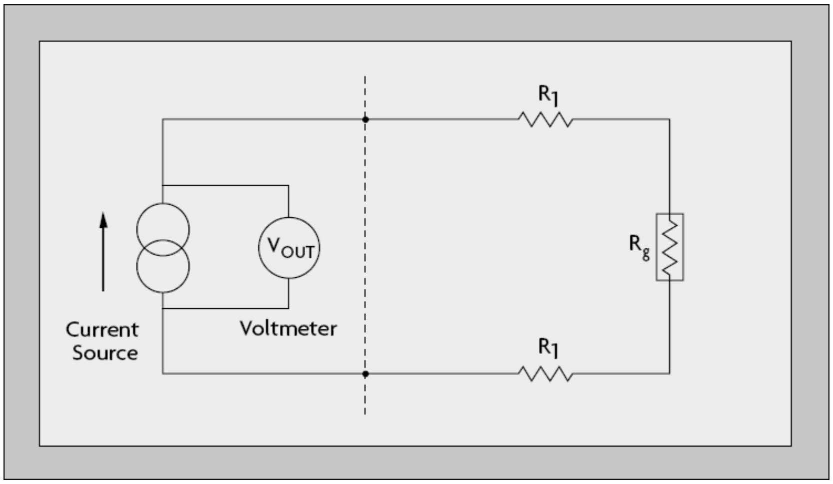

Figure 5.4: Schematics of a constant current circuit (Cited from [www.micron-piezo.com/store/backedgage.aspx])

5.3. Measurement procedure for applied blast pressure and transmitted stress

The cement foam sample was attached to the instrumented rod using a quick setting epoxy. In order to reduce friction between the outer surface of the foam sample and the wall of the shock tube, the foam was wrapped with two sheets of Teflon paper. A low viscosity oil (viscosity = 1 cps) was placed in the gap between the Teflon paper and the wall of the shock tube. This was done to ensure lateral confinement to the sample during the compaction induced by the blast loading and to ensure a one-dimensional state of motion of the foam. The pressure sensor was used as to trigger the data acquisition.

Prior to putting the sample in the shock tube a ruler with markings spaced at 0.25 in. (6.4 mm) was marked on the surface using a permanent marker. All samples were photographed before and after the test. The overall change in length of sample after the test was recorded. In addition, the permanent strain was determined locally between the markings of the ruler.

5.3.1. Cement Foam

The foam used in this study has a cementitious matrix and a cellular structure consisting of large entrained porosity in the form of uniformly distributed air cells. The air cells are introduced by mixing a stable, voluminous, micro-bubbled foam into cement paste. The porosity of the mix is varied by controlling the volume of foam mixed into the cement paste. After setting, when the cement paste gains strength, the cementitious matrix develops a cellular structure. The bubbles in the foam form disconnected pore space resulting in zero permeability.

Cement foams used in this study were made using cement paste with a water to cement ratio (by weight) equal to 0.55. The cement paste was prepared by mixing cement and water in a paddle mixer. Polypropylene fibers (Stealth® e3 micro-reinforcement, classification D700/800) were also added to the cement paste. Approximately, 10 grams of fibers was used for each 5 kg of cement paste. The foam was generated with a foam generator (shown in Figure 5.5) using a commercially available foaming agent. MEARLCRETE® FOAM LIQUID produced by Cellular Concrete LLC which is an aqueous concentrate of a surface-active Polypeptide-Alkylene Polyol condensate, specially formulated to yield tough, stable, voluminous micro bubbled foam. The foaming agent was diluted in water at the recommended dosage and mixed with air in the foam generator. The foam was then hand mixed with the cement paste and cement foams with two different wet cast densities equal to 432 and 528 kg/m^3 were produced by varying the volume of foam added to the cement paste. Cylindrical samples with diameter equal to 44 mm were prepared using acrylic molds. The inner surface of the mold was lined with a Teflon paper. The paste with the entrained foam was poured into the mold in layers and gently tapped on the sides to ensure proper placement. After 7 days, the foams were demolded and left to dry in the laboratory environment (maintained at 23 ^{o}C and 50% RH). The dry densities of the foam after 7 days were equal to 384 and 480 kg/m^3.

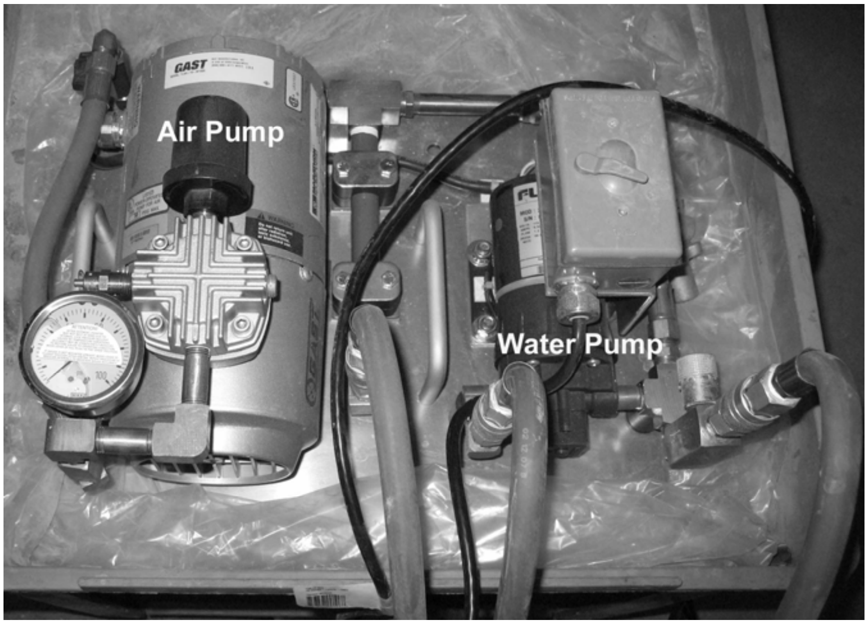

Figure 5.5: Lab Foam generator

A photograph of the cellular microstructure of a typical cement foam sample showing the dispersion of air cells is shown in Figure 5.6. After 28 days of age (following casting) the quasi-static load response of the foams were obtained. The load response of the foam was obtained under conditions of one-dimensional strain. Tests were performed by placing the foams inside an acrylic tube with inner and outer diameters equal to 44.5 and 50.8 mm, respectively. The cement foam was wrapped with two sheets of Teflon before placing it inside the tube. A low viscosity oil was placed in the gap between the Teflon sheet and the inner wall of the acrylic tube. This was done to provide lateral confinement to the foam during compaction and to ensure a one-dimensional state of motion. The load was applied to the foam using a steel cylinder which could slide inside the acrylic tube. During the deformation, engineering strain was computed as the relative displacement between the two ends of the foam divided by the original length of the foam.

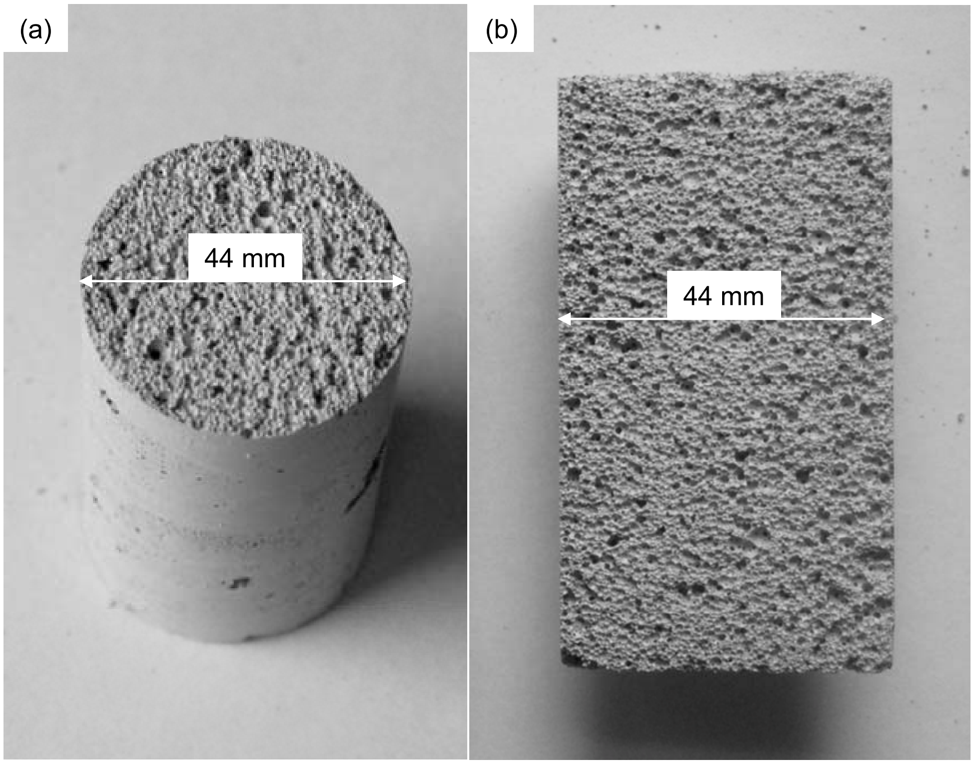

Figure 5.6: Photographs of the cement foam sample (a) cross-section and (b) a section along longitudinal axis

Typical quasi static load response of the foams is shown in Figure 5.7. In the initial linear elastic region the material follows Hooke's law. The concave response is associated with the collapse of the internal structure and subsequent densification. The cell collapse is associated with brittle crushing of the cell walls [Gibson and Ashby 1999 pp. 203]. It should be noted that while engineering strain is calculated using the overall shortening of the entire length of foam, the local deformation in the material is non-uniform in the concave part of the load-envelope.

Static stress-strain curves of cement foams were fitted using the following function with the parameters given in Table 5.1.

$$\sigma = \begin{cases} \sigma_p + E(\varepsilon - \varepsilon_p) & \varepsilon \le \varepsilon_p \\ \sigma_{po} - AE(1-\varepsilon_{po})^{\alpha} + AE(1-\varepsilon)^{-\alpha} & \varepsilon > \varepsilon_p \end{cases} \tag{5.1}$$

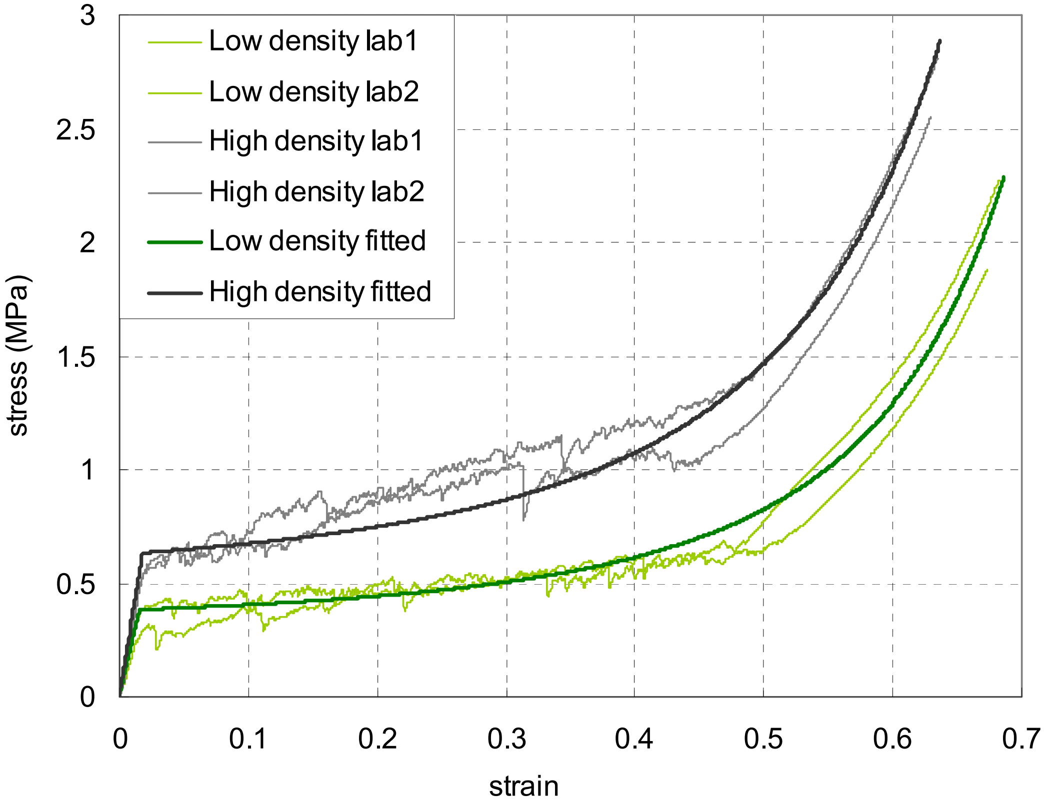

Figure 5.7: Static stress-strain curves of cement foams of different densities.

Table 5.1: Parameters used for the fitted curves in Figure 5.7

Density (kg/m^3)	E (MPa)	A	ε_{po}	σ_{po} (MPa)	α
384 (±4%)	24 (±9%)	1/350 (±35%)	0.016 (±12%)	0.384 (±12%)	2.9 (10%)
480 (±3%)	35 (±5%)	1/250 (±25%)	0.018 (±6%)	0.63 (±6%)	2.8 (10%)

5.3.2. Validation of the measurement procedure

The response of the instrumented short rod under a triangular pulse (representing blast loading) was simulated using the dynamic finite element analysis capability available in LS-DYNA. The purpose of this exercise is to validate the procedure for obtaining the applied pressure history using the measured strains from the short rod. A finite element model of a quarter of the short rod was developed and meshed using Ansys^{TM} (Version 10) as shown in Figure 5.8. The axis of the short rod was aligned with the Z-axis, while the X and the Y axes coincided with the planes of symmetry. A triangular forcing function with a initial peak value equal to 10 N and duration equal to 2 ms was applied on the all the nodes on the left face (with a normal in the Z-direction). The forcing function results in a triangular pressure pulse of p_o = 7.46 MPa and t_B = 2 ms on the narrow segment of the short rod (with a diameter equal to 19.2 mm) as shown in Figure 5.9. The other boundary conditions are such that the displacement of the cross section in XZ-plane was fixed in Y direction, the displacement of the cross-section in the YZ-plane was fixed in X direction and the displacement of the face at the right end was fixed in Z direction. The material properties of Aluminum alloy used for the short rod were $\rho = 2700\ \mathrm{kg/m^3}$, E = $69\mathrm{x}10^3$ MPa and Poisson's ratio = 0.3. The Solid 174, eight node quadrilateral element was used. The time step is determined as the time for the stress wave to across the smallest element factored by a 'Time step scale factor', which is set to be 0.9 for stability reason. This gives the time step in the analysis to be 0.15 μs. The dynamic analysis was performed using LS-DYNA solver incorporated in Ansys^{TM} (Version 10) package. LS-DYNA is a nonlinear transient dynamic finite element analysis (FEA) program. The main solution methodology is based on explicit time integration [LS-DYNA theory manual 2006].

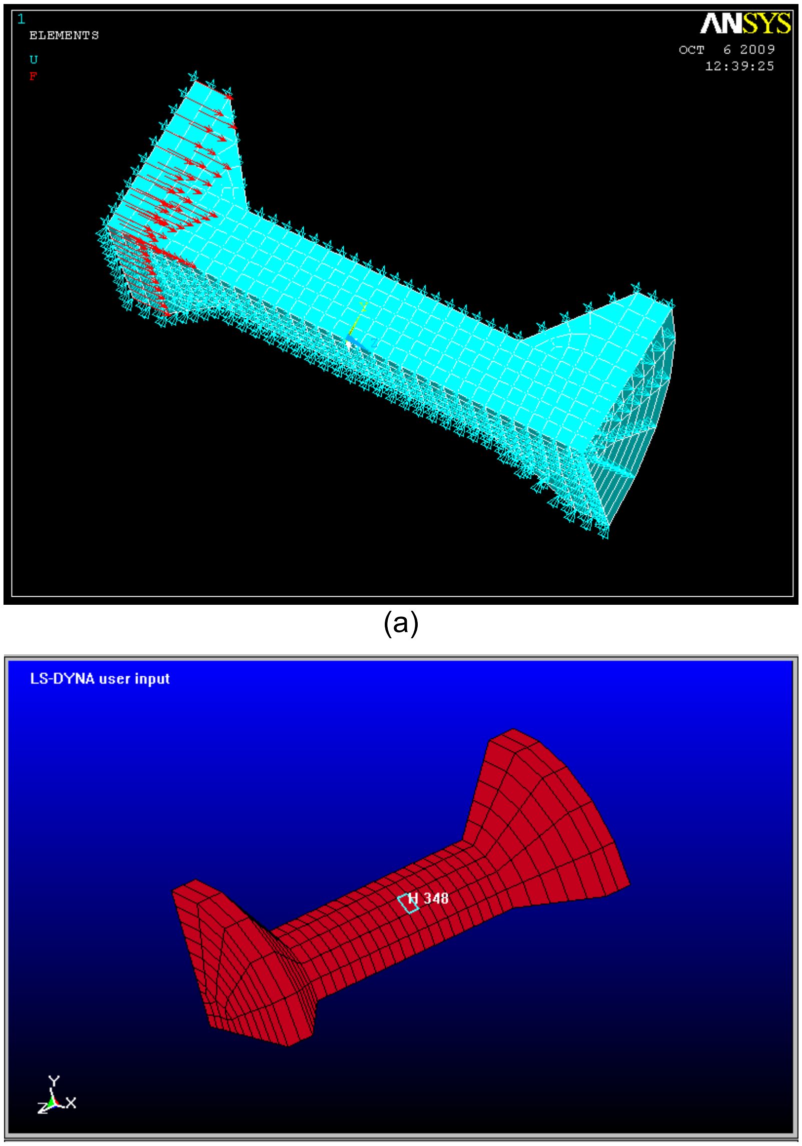

(a)

(b)

Figure 5.8: (a) Ansys and (b) Dyna model of the short rod.

The results of the analysis were post-processed using LS-PrePost^{TM}. The stress history of one element located on the surface of the rod, at the location corresponding to the location of the strain gauge on the specimen, is shown in Figure 5.8 (b). The stress response obtained from the dynamic analysis is shown in figure 9 (a). The applied pressure history is also shown in the figure for comparison. It can be seen that the stress at the specific location due to the applied triangular pulse shows a high frequency oscillatory response which is superimposed over a low frequency response with a triangular variation in time. It can also be seen that the initial stress rise produced by the wave propagation produces stress amplitude which is double of the actual applied stress. Clearly the oscillations are due to the multiple reflections of the elastic wave in the short rod, which produce a stress variation around the applied triangular pulse. The dominant period of the high frequency signal is approximately 66.6 μs. The time period obtained from the numerical analysis compares favorably with the time estimated from a simple one-dimensional stress wave calculation over the length of the rod (equal to 68.5 mm) considering fixed-free conditions at the two ends. The time for one complete cycle for a compression wave can be estimated considering reflection at the fixed end (reflected as a compression wave) followed by a phase change produced by the reflection at the free end and the subsequent round trip over the full length of the rod, for the tension wave. Considering 1-D stress compression wave speed equal to 5055 m/s, this time period can be calculated as 54.2 μs. The low frequency response recovered from the overall response using a low-pass, moving average filter over a time window equal to 66.6 μs is also shown in Figure 5.9 (a). As is seen form Figure 5.9(a), the filtered response form the short rod compares favorably with the applied stress history. A close up view of the applied stress, the unfiltered stress and the filtered stress signals immediately following the rise is shown in Figure 5.9(b). It can be seen that the actual zero rising time of the onset of the applied triangular pulse has become 33 μs for the filtered signal. This is due to the use of the low-pass, moving average filter over a time window equal to 66.6 μs on the unfiltered signal. Therefore, the dynamic finite element analysis shows that a good sensitivity can be achieved with the use of the short rod as shown in Figure 5.3.

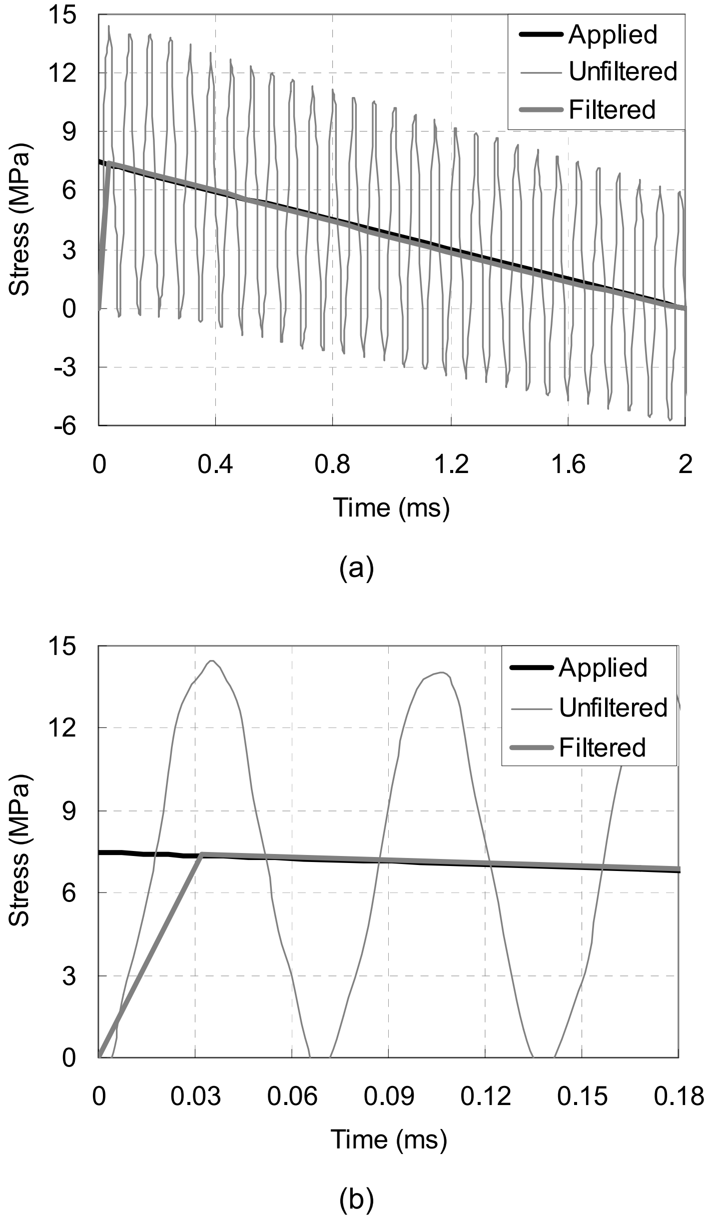

Figure 5.9: Stress history at a fixed location of the short rod due to a triangular pulse. (Applied: applied stress at the loaded end; Unfiltered: unfiltered original stress response at the measured point; Filtered: filtered stress.)

The linear response of the short rod is illustrated considering triangular inputs with two different amplitudes as shown in Figure 5.10. In Figure 5.10 “unfiltered 1 and filtered

1" are the same results shown in Figure 5.9 and "unfiltered 2 and filtered 2" are obtained when the applied load on left face in Figure 5.8 is doubled. As shown in Figure 5.10 the signal obtained at the measure point on the short rod scales linearly as the increase of applied stress.

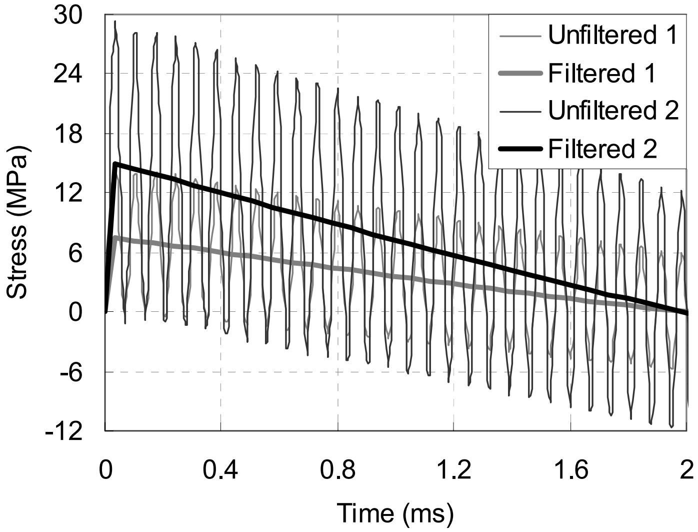

Figure 5.10: Stress history at a point on the short rod due to two triangular pulses.

5.3.3. Calibration of the instrumented short rod

It should be noted that for the instrumented short rod, the exact relationship between the recorded strain and the stress at a given location would depend upon factors such as the gage factor of the strain gage, the material constants and the geometry of the rod. Considering linear elastic behavior and linear gage response, all these factors would result in a constant scaling factor for relating measured strain with stress at the location. In addition, the exact relationship between the applied stress on the face of the instrumented short rod and the measured stress at a given location on the rod depends upon the geometry and the elastic constants of the rod. Since the measured stress is linearly related to the applied pressure, this results in an additional scaling factor, which relates the measured and applied stresses. The combined effect of the geometric, material and instrumentation related factors would result in a calibration factor for relating the measured strain to the applied pressure, which can be determined experimentally. The stress measurement system was calibrated using a blast pressure input applied directly to the instrumented short rod. The pressure measured by the pressure gauges located adjacent to the front end of the instrumented short rod (P_2 as shown in Figure 5.3) corresponds to the applied stress input. The strain gauge output was calibrated against the applied pressure. The measured strain can therefore be converted to applied stress using the calibration factor.

The calibration of the instrumented short rod is shown in Figure 5.11. The blast pressure loading applied on the face of the instrumented rod is shown in Figure 5.11(a). The applied blast pressure is due to the reflection of an incident blast wave at the face of the instrumented short rod and recorded using the pressure transducer P_2, located at a distance of 45 mm from the face. Figure 5.11 (b) shows the original unfiltered signals obtained from the strain gages attached to the short rod, in voltages. The high frequency oscillations associated with the wave reflections are clearly evident in the measured response (shown in the inset). The time period associated with the oscillations is measured to be 64 μs, which agrees favorably with the value obtained from the numerical analysis. The low-frequency component of the original signal was obtained using a low-pass averaging filter with a time period equal to 64 μs and is also present in Figure 5.11(b). The calibration factor for the instrumented short rod was then obtained by matching the magnitude of the filtered voltage from the instrumented short rod with that of the applied stress obtained from the pressure gauge. The calibration factor was applied to the filtered voltage signal to give the stress history measured by the instrumented short rod and shown in comparison to the applied pressure history in Figure 5.11(a).. A good comparison between two time histories is observed in Figures 5.11 (a). The calibration using a real blast pressure wave shows that the measurement procedure provides an accurate estimate of the applied pressure history and the initial shock front is adequately resolved.

Comparisons between the calibrated stress signals from the instrumented short rod and the applied pressure for different blast pressure loads is shown in Figures 5.12 (a) and (b). The calibration constant determined from the results in Figure 5.10(a) was applied to the cases shown in Figures 5.12(a) and (b). The direct blast pressure measurements provide a validation for that the applied stress measurement using the calibrated strain measurements obtained from the short stepped rod.

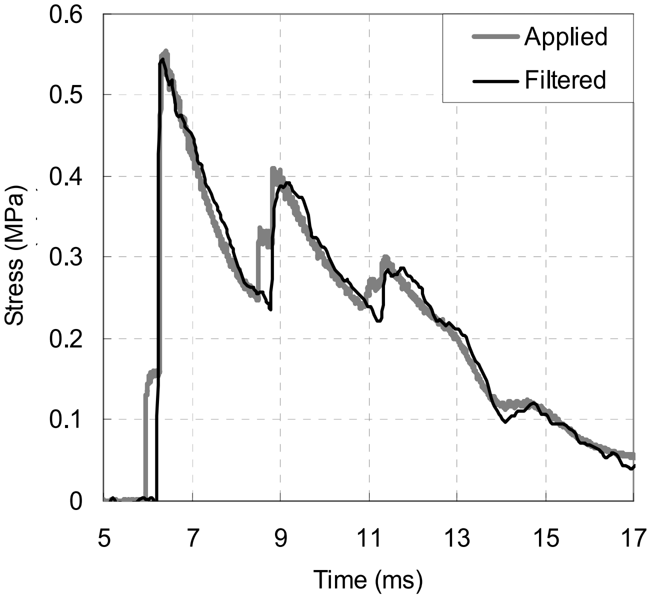

(a)

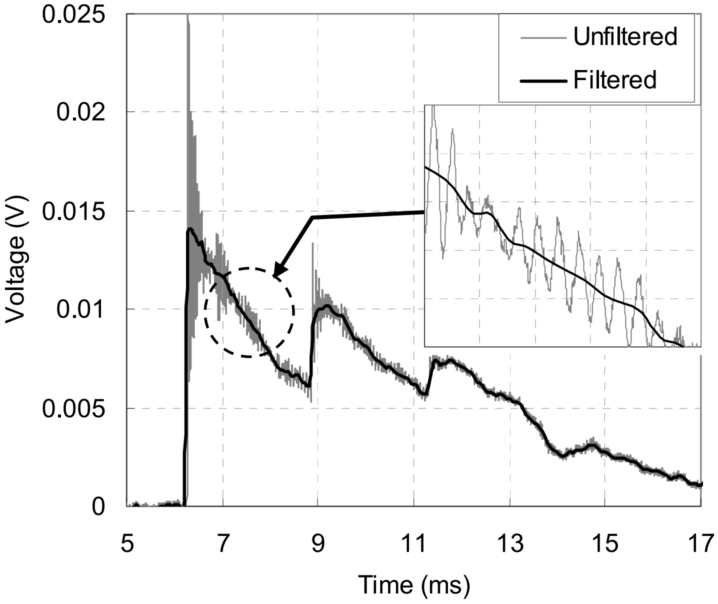

(b)

Figure 5.11: Stress history from the instrumented short rod for a directly applied blast. (a) Applied pressure and calibrated filtered stress, (b) unfiltered and filtered voltage.

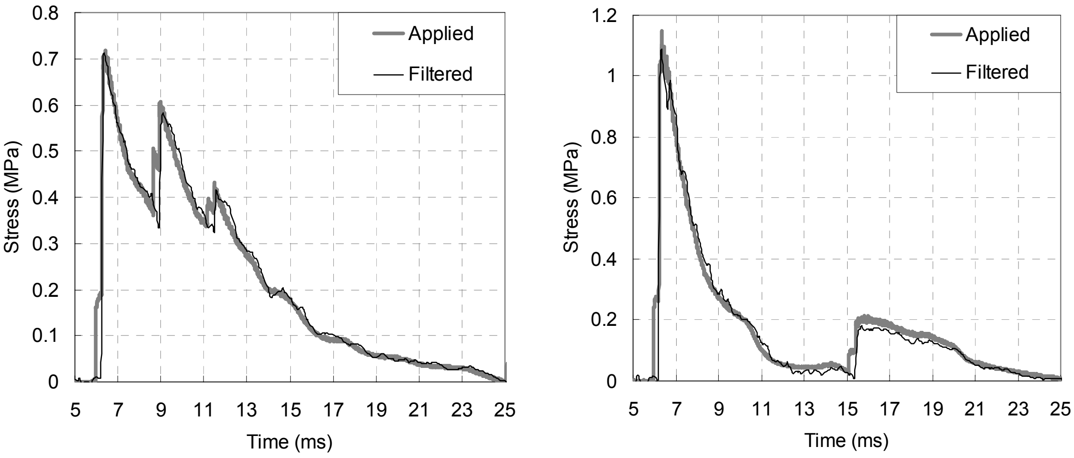

(a) (b)

Figure 5.12: (a) and (b): applied pressure and the calibrated filtered stress for different blast loadings.

5.4. Experimental Results with Cement Foam

Results of the experimental test program are presented in this section. A cylindrical sample made of cement foam was attached to the front face of the instrumented short rod as shown in Figures 5.2 and 5.3. A typical experimental result showing the comparison between the applied blast pressure and the transmitted stress is shown in Figure 5.13 (a). In the experiment an incident blast wave was generated heading downstream towards the foam sample. The time history of the applied stress due to the normal reflection of incident blast waves was recorded by the pressure gauge P_1 at the loaded end of the foam sample and is plotted as the dark curve. The transmitted stress was recorded by the instrumented short rod calibrated using the method stated above and is plotted as the light curve. It can be seen that there is clearly a benefit of using cement foam. The applied stress with a higher peak stress is transformed to a transmitted stress with a lower peak stress. In the experiment, the cement foam was compacted by the applied blast load. The compaction of cement foam provides a dissipative mechanism to the blast wave and hence attenuates its strength as the blast wave travels in the cement foam.

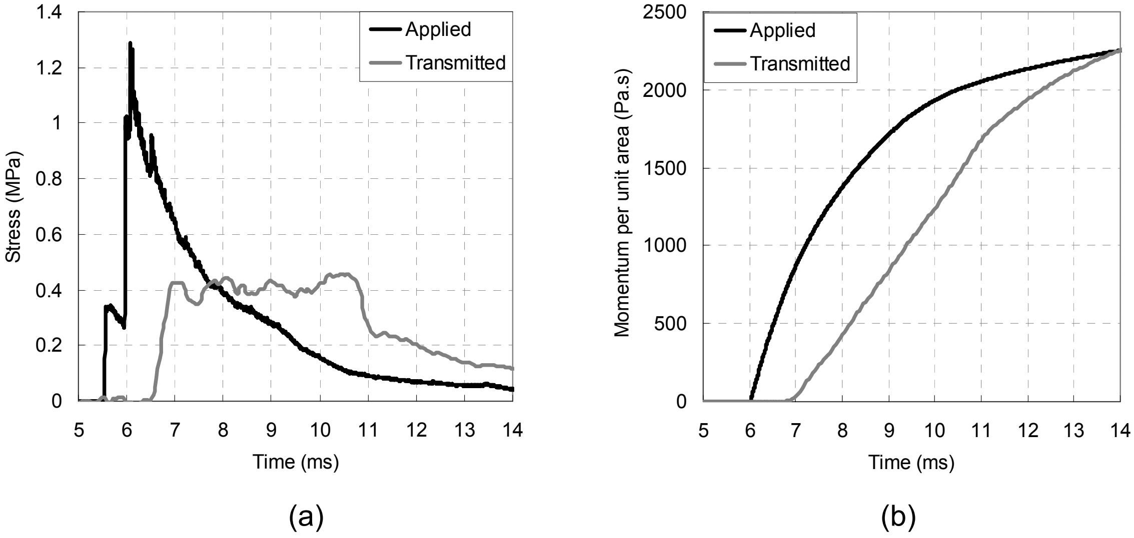

Figure 5.13: Typical response of cement foam under blast loadings: (a) applied pressure and transmitted stress and (b) the impulse of applied pressure and transmitted stress.

The shock tube confines the lateral expansion of the cylinder foam sample during its compaction, which generates a friction between the inner wall of the shock wall and the foam sample. The friction would reduce the stress transmitted to the short rod and may be contribute to attenuation of the stress amplitude. In order to minimize the influence of friction, the samples were wrapped with two sheets of Teflon and a low viscosity oil was placed in the gap between the Teflon sheets. An indirect measure of the friction is made by comparing the impulse obtained from the applied and transmitted stress histories as shown in Figure 5.13 (b). The impulse is a measure of the momentum transfer and is obtained by integrating the stress history over time. The difference between the applied and the transmitted impulses during the loading procedure corresponds to the momentum in the compacted foam. It can be seen that the impulse of the applied blast pressure near the end of the applied pressure history compares very favorably with impulse of the transmitted stress, which provides confirmation that the influence of friction on the deformation response of the cement foam is negligible.

5.4.1. Foam samples of different lengths subjected to the same blast loading

The results showing the applied and transmitted stress for 384 kg/m^3 and 480 kg/m^3 density foams are given in Figures 5.14 (a) and 5.14 (b), respectively. For each density, samples of varying length were subjected to blast pressure loadings of similar amplitudes and durations. In all tests, the applied blast pressure amplitudes are comparable and nominally equal to 1.3 MPa, which is greater than the crushing stress of the foam; σ_{po} is equal to 0.384 MPa and 0.66 MPa for foams with densities 384 and 480 kg/m^3, respectively. For the 384 kg/m^3 density foam, samples with three different lengths, L = 230, 152 and 102 mm (designated as long, mid and short in Figure 5.14 (a)) were used in the test program. For the 480 kg/m^3 density foam, foam samples of lengths equal to, L = 178, 127 and 76 mm (designated as long, mid and short Figures 5.14 (b)) were used in the test program. From the results for both cement foams, it is immediately obvious that the transmitted stress depends upon the length of foam samples. Considering the response from the samples of the largest length for foam samples of both densities, the applied blast pressure loading is transmitted as a stress pulse of rectangular shape characterized by a constant level of stress of a magnitude smaller than the applied pressure. The rectangular pulse has amplitude approximately equal to, but slightly higher than the crushing strength of the foam. As the length is decreased, there is an increase in the magnitude of stress, which follows the initial constant transmitted stress. The increase in the transmitted stress is very significant in the samples with shortest length; the transmitted stress amplitude is higher than the applied blast pressure amplitude producing stress enhancement for this case.

The results indicate that when the length of the foam samples is sufficiently long there is a complete attenuation of the applied blast pressure to a level, which is slightly higher than the crushing strength of the foam. The length of the foam required to attenuate a given blast signal depends upon the crushing strength of the foam. On decreasing the length, there is an increase in the amplitude of transmitted stress. This suggests that there is a critical length of the foam (L_{cr}), which depends upon its crushing strength, that is required to completely attenuate the applied blast pressure loading. When the length of sample is less than L_{cr}, the transmitted stress amplitude exceeds the crushing strength of the foam. For the applied blast pressure loading, L_{cr} for the 384 kg/m^3 foam is smaller than 230 mm but larger than 152 mm. Similarly, for the 480 kg/m^3 foam, L_{cr} is smaller than 178 mm but larger than 127 mm.

When the length of the foam is significantly smaller than $L_{cr,}$ there could be a stress enhancement, where the transmitted stress with the foam is higher than the stress directly applied by the blast pressure loading. This suggests that there is a minimum threshold on the length of the foam (L_{th}), below which there is a stress enhancement. For the applied blast pressure loading, L_{th} for the 384 kg/m^3 foam is in the range {230 mm, 152 mm} and for the 480 kg/m^3 foam in the range {178 mm, 127 mm}.

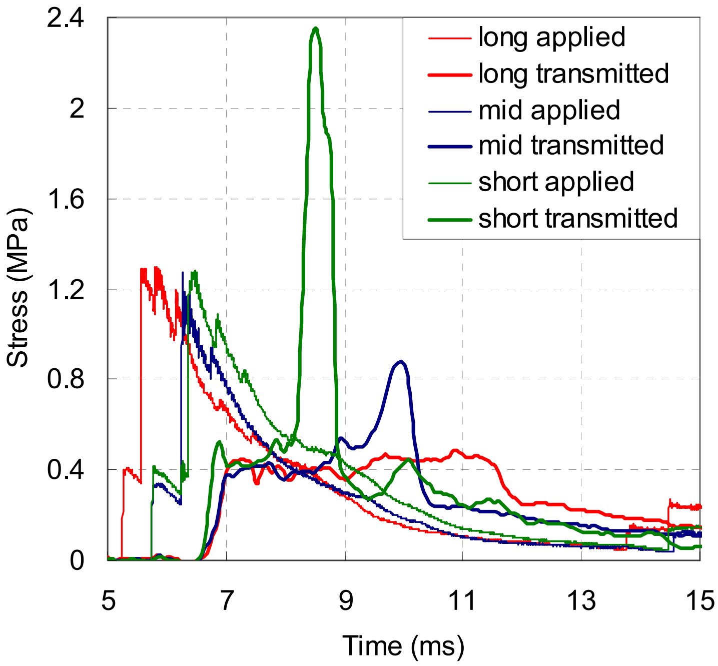

(a)

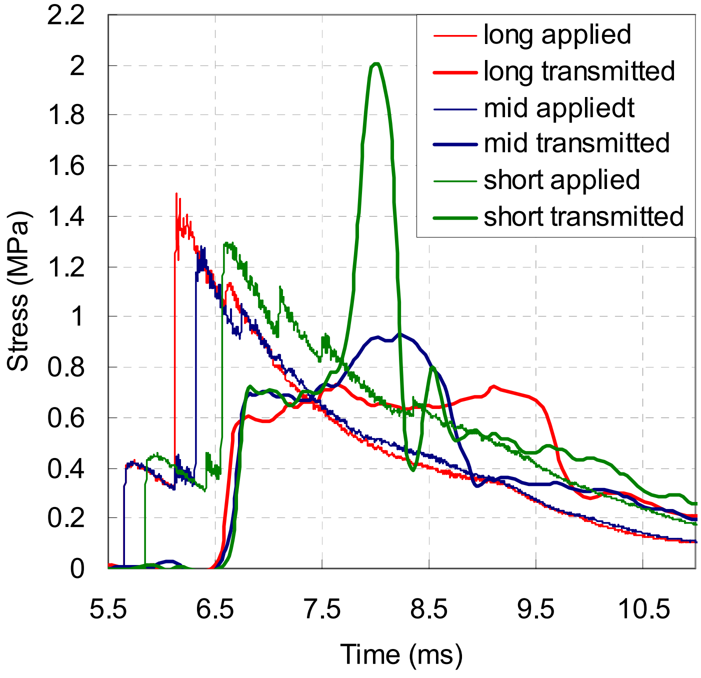

(b)

Figure 5.14: Applied blast pressure versus transmitted stress under similar blast for three samples lengths (long, mid and short) and two densities: (a) 384 and (b) 480 kg/m^3.

5.4.2. Analysis of Compacted Foam

Irreversible volumetric contraction was observed in all samples subjected to blast pressure loading. There was compaction of the material along the length of the sample, which was produced by the crushing of the cells. The length of the material compacted however, varied with the initial length of the sample. In samples of length larger than L_{cr}, compaction and crushing of cells was observed in material at the loaded end and at transmission end. Some material in the middle was found to be relatively intact. In samples with length smaller than L_{cr}, compaction and crushing of cells was observed over the entire length of the foam samples.

Typical photographs of foam samples before and after testing are shown in Figures 5.15 and 5.17, respectively for the 184 mm and the 76 mm samples made with the 384 kg/m^3 density foam. For each sample, two opposite faces are photographed. In Figure 5.15, the initial length, L=184 mm and the applied blast pressure amplitude, p_o = 1 MPa. In Figure 5.17, the initial length, L=76 mm and the applied blast pressure amplitude, p_o = 1.2 MPa. The engineering strain of the compacted foam along the length of the sample was obtained using the distance between two adjacent markings in the compacted material and is shown in Figures 5.16 and 5.18. In figure16 (184 mm long foam sample), it is observed that at the loaded end 80 mm foam is compacted with an irreversible strain equal to 0.45, at the target end 60 mm foam is compacted and has an irreversible strain approximately equal to 0.3 and the region between the two compacted portions remains relatively un-deformed. The result indicates that 184 mm is sufficient to attenuate the applied blast wave and it is larger than L_{cr} for the applied blast loading. In Figure 5.18 (76 mm cement foam), it is observed that at the entire foam is compacted and the average irreversible strain reaches up to 0.6. Therefore, the 76 mm does not provide sufficient length required to fully attenuate the applied blast pressure loading and is hence smaller than L_{cr}.

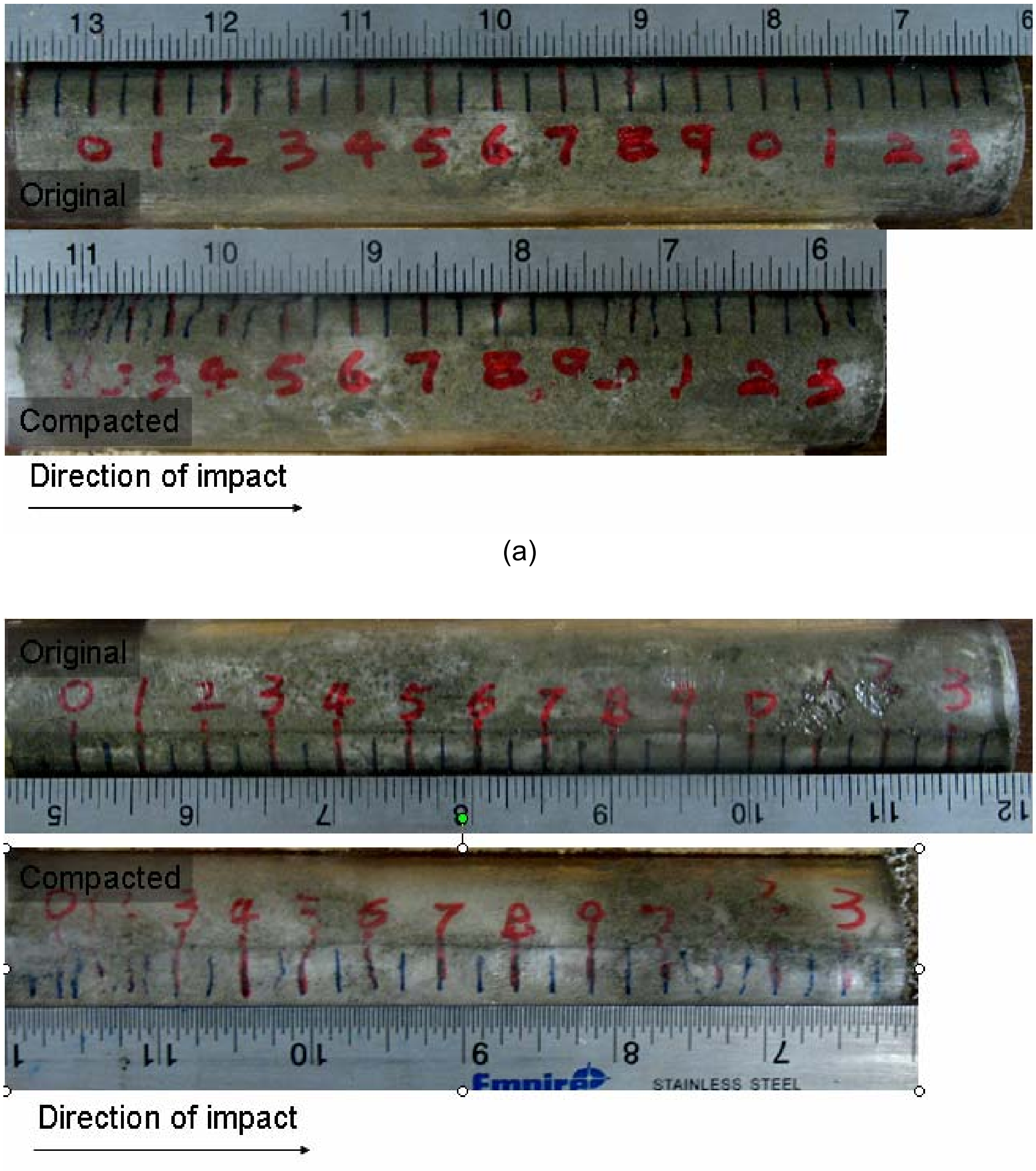

(a)

(b)

Figure 5.15: Deformation of L = 184 mm sample made with the 384 kg/m^3 cement foam before and after compaction (L > L_{cr} case), (a) face 1 and (b) face 2.

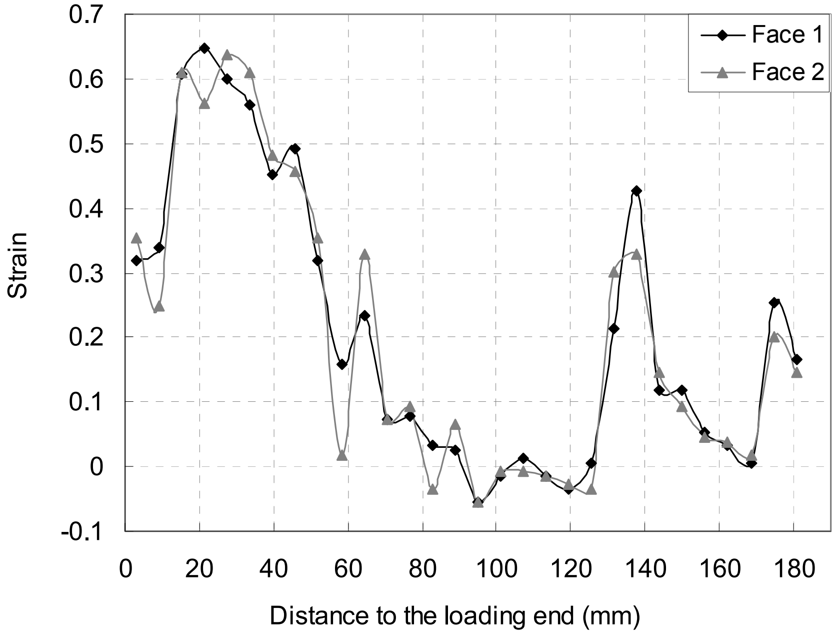

Figure 5.16: Engineering strain after compaction measured from Figure 5.15.

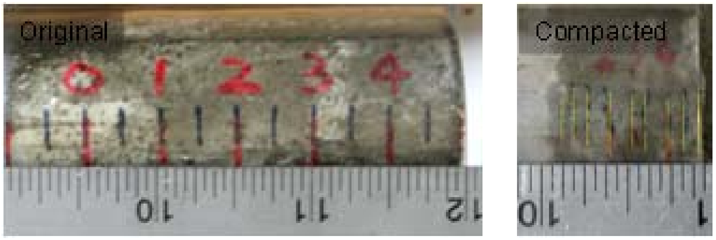

(a)

(b)

Figure 5.17: Deformation of L = 76 mm sample made with the 384 kg/m^3 cement foam before and after compaction (L < L_{cr} case), (a) face 1 and (b) face 2.

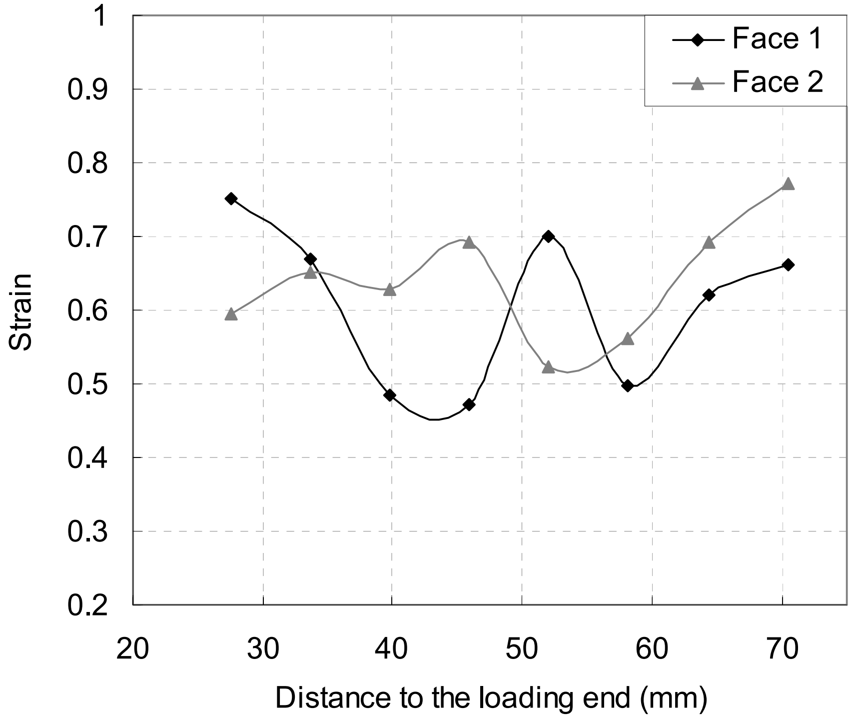

Figure 5.18: Engineering strain after compaction measured from Figure 5.17.

5.4.3. Transmitted stress for different blast when L > L_{cr}

To study the effect of cement foam in mitigating different blast loads, cement foams were tested using blast pressure loads with different pressure amplitudes. Figure 5.19 (a) and (b) shows the experimental results of the applied blast pressure and transmitted stress for three different blast pressure amplitudes (high, mid and low) for cement foams with densities equal to 384 and 480 kg/m^3, respectively. In all tests, sufficiently long length of the foam was used to ensure that it exceeded L_{cr}. This was confirmed by the photographic evidence of the foams after the tests. In Figure 5.19 (a), L = 230, 203 and 165 mm were used for high, mid and low level blasts, respectively. In Figure 5.19 (b), L = 178, 152 and 115 mm were used for high, mid and low level blasts, respectively. The applied blast pressure histories are transmitted without stress enhancement in all cases. In all cases, the transmitted stress history has a prominent rectangular part followed by a decaying profile. Following the initial plateau, the transmitted stress exhibits a sudden drop and then has a decreasing profile similar to the applied stress history. The amplitudes of the rectangular pulses are nominally higher, but close to the crushing strengths of the cement foam (σ_{po}=0.384 MPa for 384 kg/m^3 cement form and σ_{po} = 0.63 MPa for 480 kg/m^3 cement form), regardless of the applied blast pressure amplitude. The duration of the transmitted triangular pulse, on the other hand, increases with an increase in the applied blast pressure amplitude. In all cases the duration of the applied blast pressure wave is approximately equal. There is thus a decrease in the impulse of the applied blast pressure loading when the pressure amplitude is decreased. The results from the transmitted stress history indicate that the impulse transferred to the solid substrate is not affected by the presence of cement foam. Figure 5.19 (c) and (d) show the comparison of the time history of the applied blast pressure and transmitted stress for Figures 5.19 (a) and (b), respectively. The impulse (or the momentum) is the time integration of the corresponding pressure/stress curves in Figures 5.19 (a) and (b). It is noted that the first rise in the applied blast pressure is induced by the incident blast wave and thereby is excluded for the calculation of momentum.

The cement foam of $L > L_{cr}$ when placed in front of a solid substrate can reduce the peak stress of the applied blast pressure (experienced when no cement foam is present) to a level corresponding to the crushing strength of the foam. Therefore, there is a potential for using foams for preventing damage to the solid substrate resulting form high amplitude stress wave propagation.

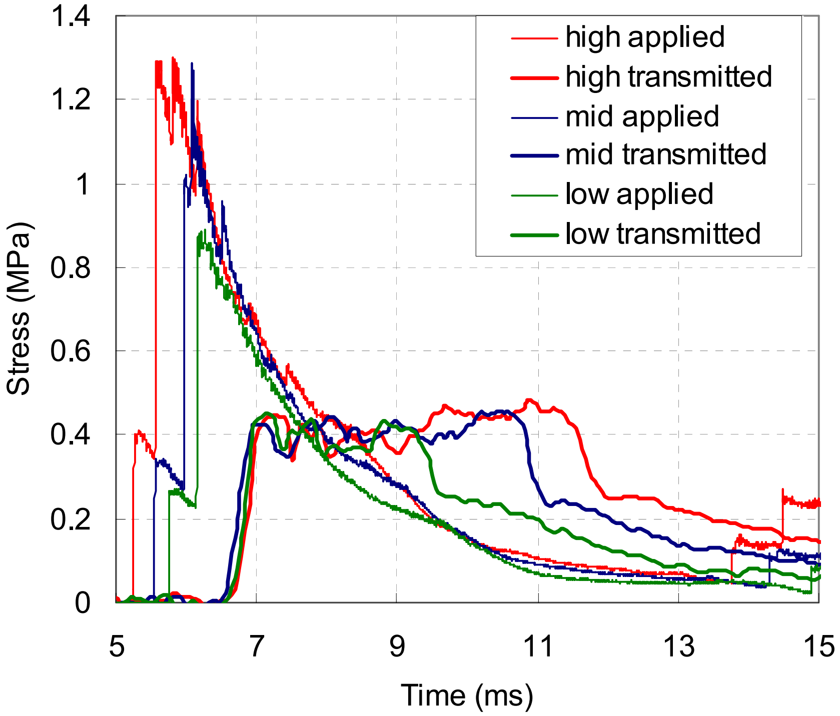

1.4
1.2
1
0.8
0.6
0.4
0.2
0
Stress (MPa)
5
7
9
11
13
15
Time (ms)
high applied
high transmitted
mid applied
mid transmitted
low applied
low transmitted

(a)

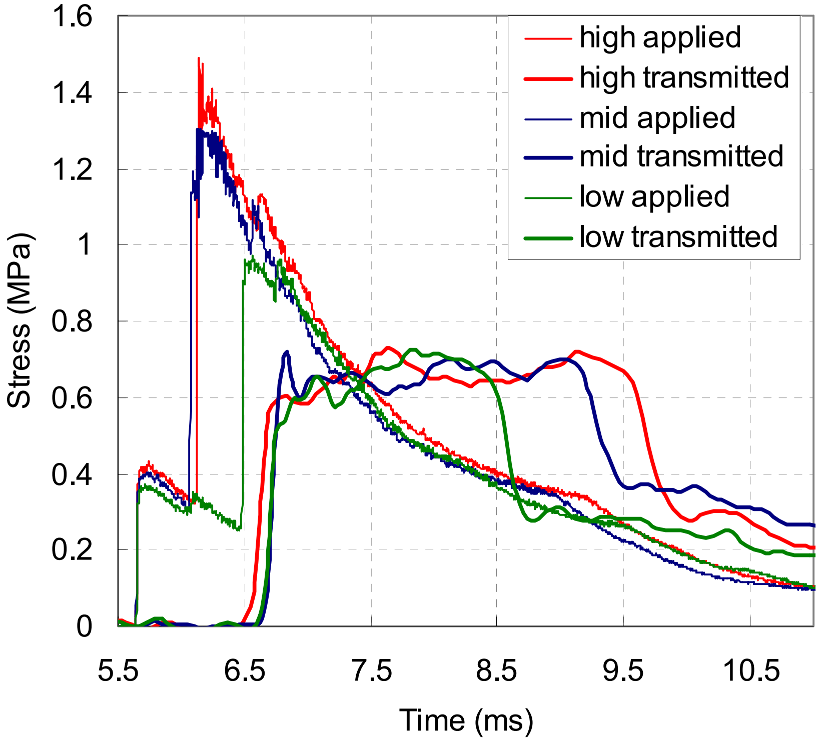

1.6
1.4
1.2
1
0.8
0.6
0.4
0.2
0
Stress (MPa)
5.5
6.5
7.5
8.5
9.5
10.5
Time (ms)
high applied
high transmitted
mid applied
mid transmitted
low applied
low transmitted

(b)

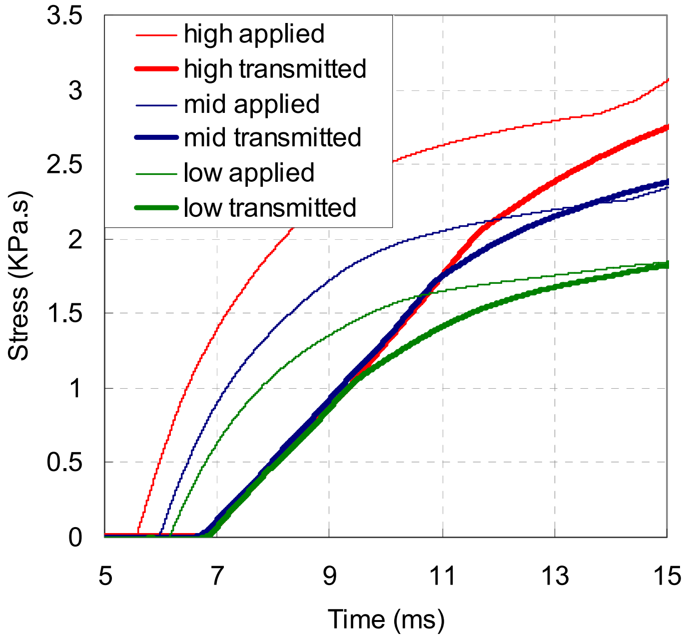

(c)

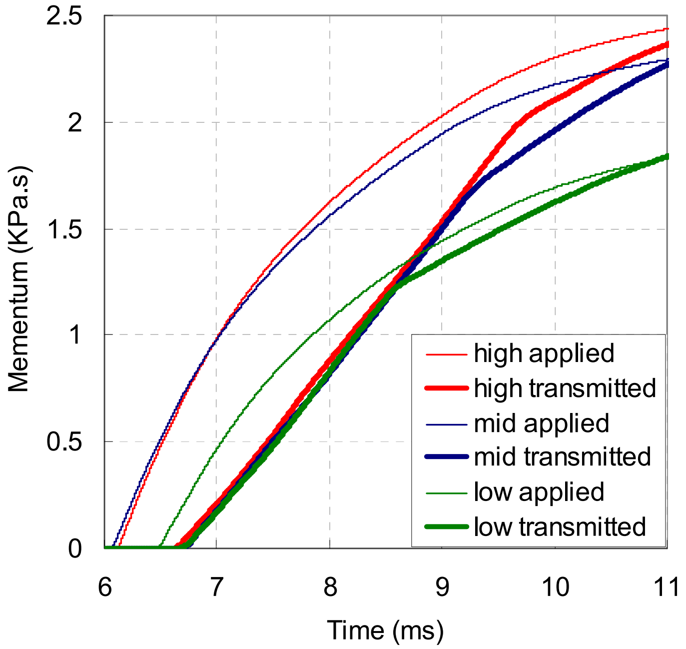

(d)

Figure 5.19: Blast pressure versus transmitted stress under high, mid, and low blasts and for (a) 384 and (b) 480 kg/m^3 foams and the corresponding momentums (c) and (d).

5.5. Numerical Simulation

In this section, the experimental results are compared with the prediction of the transmitted stress obtained using both the exact Riemann-based finite volume formulation considering the actual stress-strain curve of the foam and the RPPL idealization of the actual stress-strain curve of the foam. The experimental data is used to validate the results from both methods. Using the RPPL idealization allows for evaluating the transmitted stress analytically without resorting to numerical schemes. While the RPPL model cannot be used to predict the transmitted stress when $L<L_{cr}$, the L_{cr} can be determined analytically for a given blast pressure input and foam characteristics. Therefore, once the RPPL idealization for the foam behavior is established and validated, it can be used to determine the length of foam required for a given threat level (where the blast pressure characteristics are prescribed). Determining L_{cr} using the exact Riemann based finite volume formulation for a given blast pressure input requires an iterative procedure where the performance of different lengths have to be evaluated for a given blast input and is therefore computationally intensive. Hence, this method is not suitable for developing practical applications. The finite volume formulation can however be used to develop a complete understanding of the dynamic response of the foam as a function of its length and the stress amplification for length shorter than L_{cr}.

5.5.1. The Exact Riemann Solver Based Finite Volume Scheme

The dynamic response of foam subjected to the given blast pressure loading is obtained using the exact Riemann solver-based finite volume scheme developed in previous chapter. In the numerical simulation, the 1-D foam bar is fixed at the target end and the blast pressure history obtained form the experiment is applied on the loaded end. The stress-strain curve of foam is given by Equation 5.1 and the parameters, E, ε_{po} (and the corresponding σ_{po}), A and α required to fit the stress-strain response of the foam given in Table 5.1 were used. The average values of the parameters for foams of the different densities were used in all numerical simulations. The foam bar is discretized in to 100 cells and CLF=0.6 were typically used in all the numerical simulations.

Comparisons between the transmitted stress obtained experimentally and the transmitted stress obtained using the exact Riemann based finite volume method for the cases corresponding to $L>L_{cr}$ and $L<L_{cr}$ are shown in Figures 5.20 and 5.21, respectively. For $L> L_{cr}$, it can be seen that for both 384 and 480 kg/m^3 density foams, the finite volume formulation predicts a slight stress rise following the initial plateau, when the length of the foam in the numerical formulation is taken exactly equal to the actual length used in the experiment. While there appears to be a slight rise in the stress at the end of the plateau, it cannot be delineated clearly from the variation in the experimentally measured stress signal for the 384 kg/m^3 foam. The amplitude of the initial plateau in the transmitted stress however compares favorably in both cases. Results of numerical simulation considering a slightly longer length than used in the experiment are also shown in Figures 5.20(a) and 5.21(a). It can be seen that in both cases, while the numerical simulations do not show any increase at the end of the plateau, the duration of the stress plateau is longer than observed in the experiments. Also, when the longer length of the foam is used, there is a slight delay in the arrival of the first elastic wave when compared with the experiments.

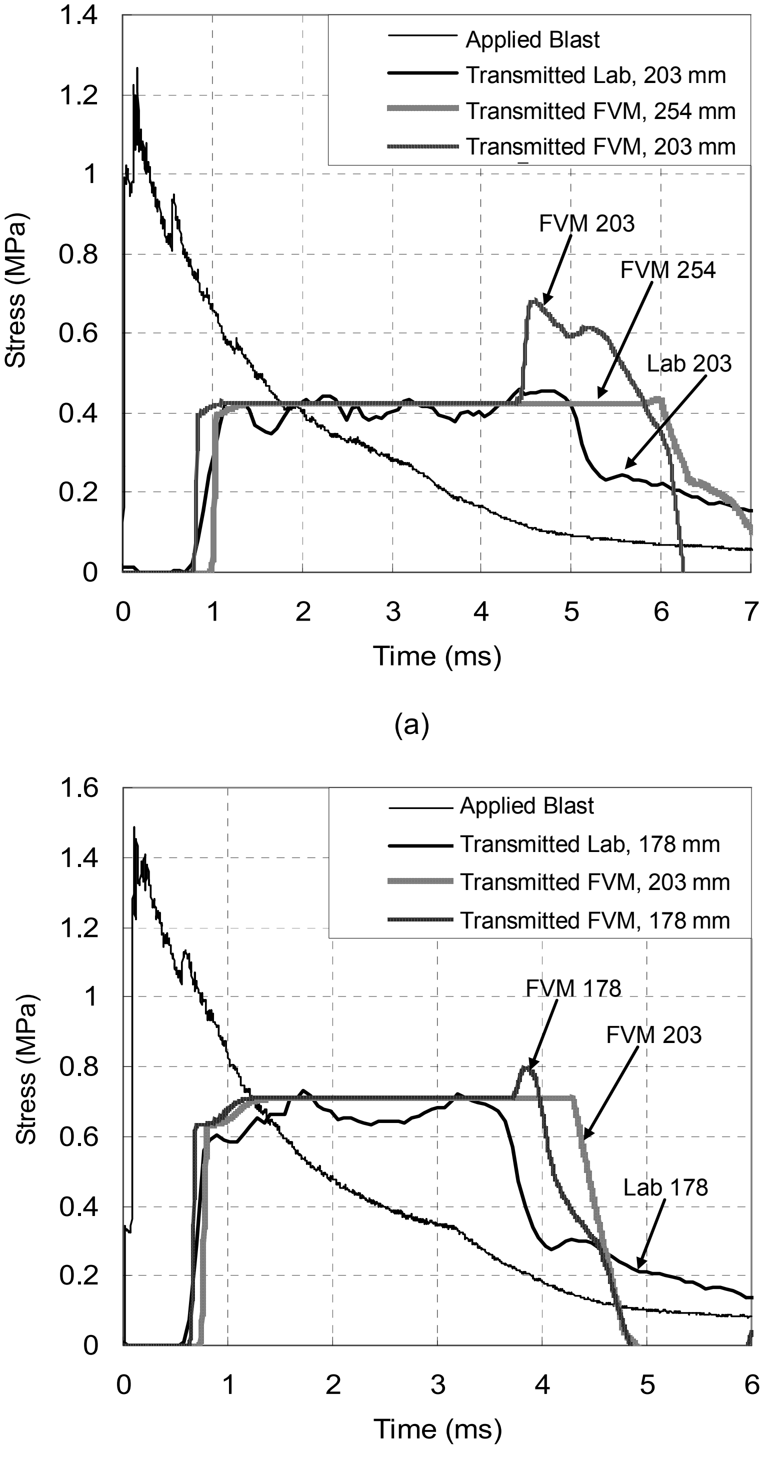

(a)

(b)

Figure 5.20 Prediction of transmitted stress using exact Finite Volume Formulation and comparison to experimental results for $L>L_{cr}$. (a) 384 and (b) 480 kg/m^3.

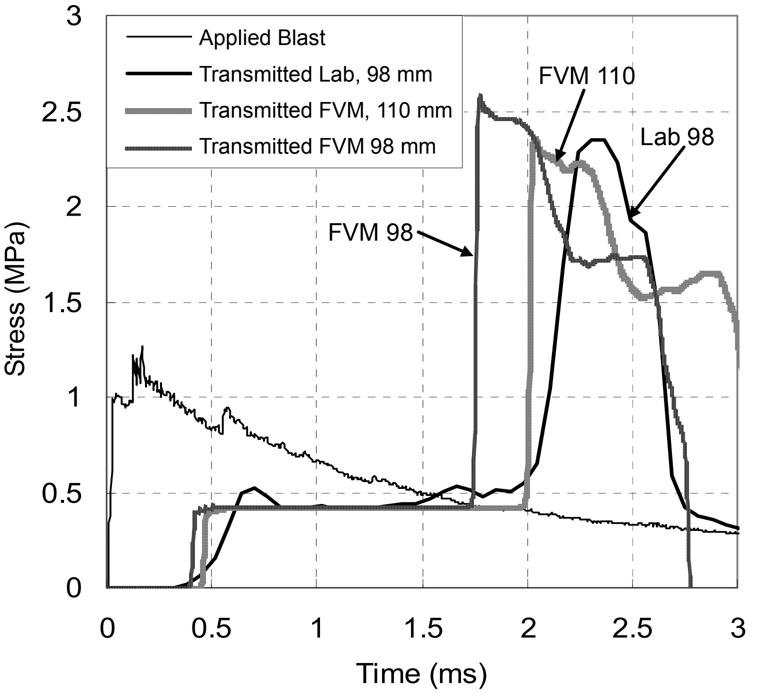

(a)

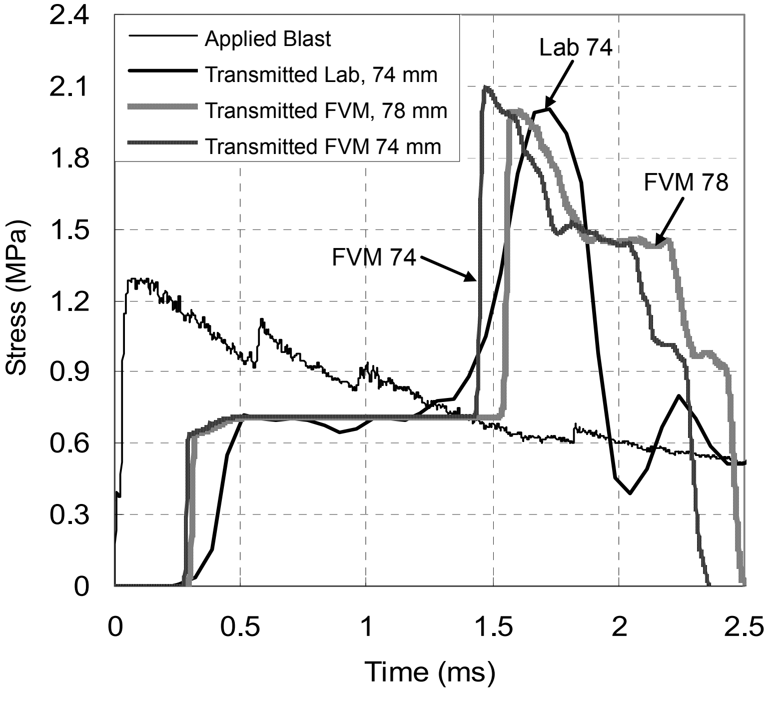

(b)

Figure 5.21 Prediction of transmitted stress using Finite Volume Formulation and comparison to experimental results for L<Lcr. (a) 384 and (b) 480 kg/m3 cement foams.

Good agreement between the numerical simulation and the experimental measurement are also obtained for the case when $L<L_{cr}$ (Figure 5.21 (a) and (b)). The numerical simulation clearly captures the pressure enhancement due to the cement foam. The numerical simulation predicts an abrupt increase in the transmitted stress to σ_{Po} of the foam (0.43 MPa for Figure 5.21 (a) and 0.71 MPa for Figure 5.21 (b)) followed by a constant plateau. Following the constant transmitted stress, which lasts for approximately 1.5 ms and 1.25 ms for the 384 and 480 kg/m^3 foams, respectively, an increase in the transmitted stress to a value higher than the applied blast pressure is predicted. The prediction from the numerical scheme, when the length of the foam is taken exactly equal to the value used in experiments indicates a slightly higher rise than the stress enhancement obtained experimentally. Numerical analyses were also performed considering larger lengths of foam, which provide better comparison with the magnitude of the stress enhancement.

The slight over-prediction of the finite volume simulations can be attributed to the variation in the material properties. It has previously been shown that there is a noticeable difference in the quasi-static stress-strain response of the foam samples (made from the same batch and variation between batches). This is particularly true for the concave part of the stress-strain response. This produces a range in the values of the parameters used to fit the concave part of the stress-strain response. In the numerical simulations, however, the average values obtained from several specimens were used. While the initial elastic modulus and the crushing strength determine the speed of the initial elastic wave and the plateau stress, respectively, the concave part of the stress strain curve plays a significant role in determining the attenuation of the shock wave associated with the plastic crushing of cells. Therefore, variation in the concave part of the stress response significantly influences the length of the foam required for completely attenuating a given blast pressure wave. Differences in the actual concave stress-strain response and the average value could lead to differences in the amplitude of the transmitted stress, if it is not completely attenuated.

A comparison of strain after compaction predicted by the finite volume calculation and the experimental values are given in Figure 5.22 for the 384 kg/m^3 foam when (a) $L>L_{cr}$ and (b) $L<L_{cr}$. In both cases, the experimental values plotted in the figures are the average values measured from the opposite faces of a specimen as shown in Figure 5.16 and 18, respectively.

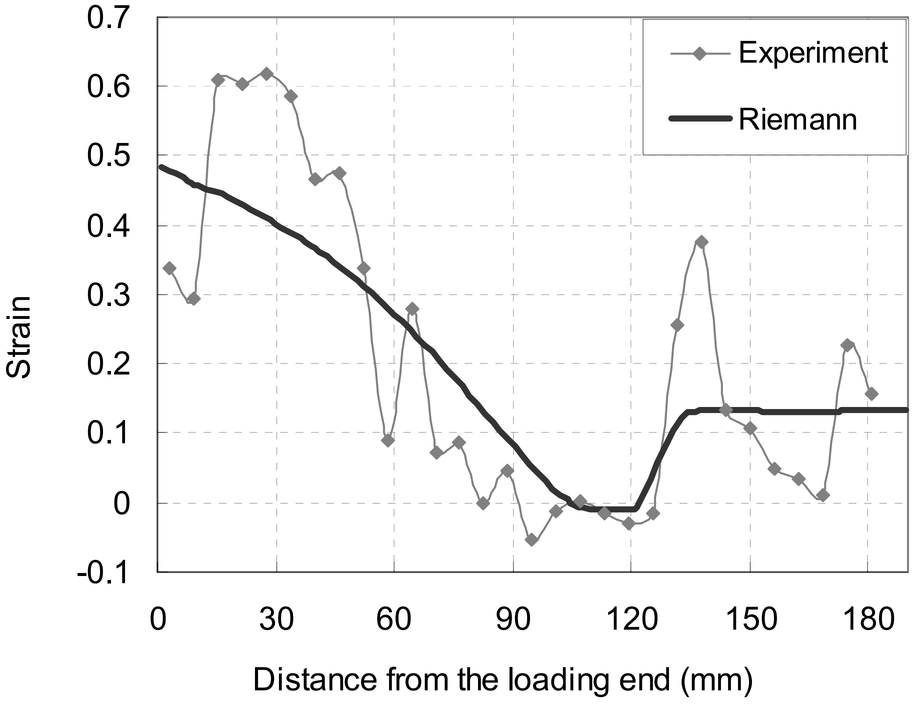

(a)

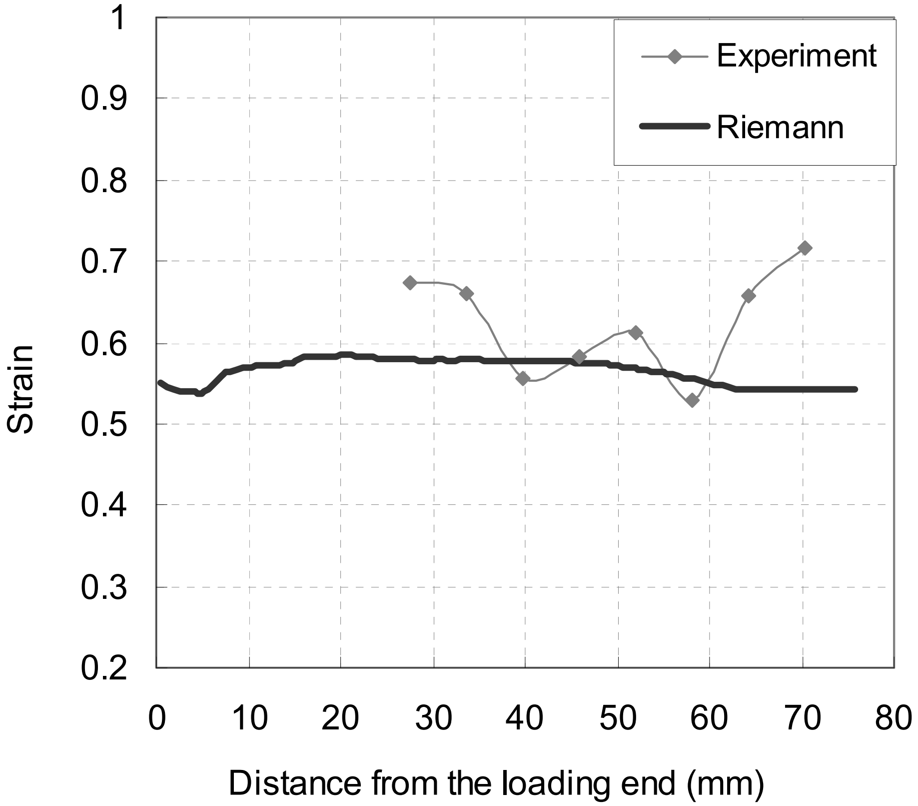

(b)

Figure 5.22: Comparison of strain after compaction (numerical and experimental) for cases (a) L > L_{cr} and (b) L < L_{cr}

For the foam with density equal to 384 kg/m^3, the strain and stress in the foam as a function of time are shown in Figures 5.23 and 5.24, respectively for L>L_{cr} and L<L_{cr}. The results in Figure 5.23 (L>L_{cr}) are for the case when the initial length of the foam is equal to 184 mm, which allows for complete attenuation of the applied blast pressure wave. In the X-t plots, t=0 corresponds to the incidence of the blast pressure wave on the foam. The X coordinate refers to locations along the initial, undeformed foam. The X-t plots clearly show the initial increase in stress produced by the elastic wave which produces a very small change in strain as it travels along the length of the foam. The applied blast pressure amplitude produces an increase in stress at the loaded end, which increases beyond the σ_{Po} of the foam. This produces a compaction front, which as it travels down the foam decreases in amplitude. The second wave travels slower than the initial elastic wave and produces large strain in the material. The elastic wave upon reflection at the fixed end produces an increase in stress, and it generates a wave travelling in the opposite direction, which produces strains larger than ε_{Po} in its wake. The stress amplitude of the reflected wave also decreases as it travels in the foam. From the strain contours, it is apparent that there is portion of the material between 100 mm and 120 mm, which remains elastic. The material on either side, however, would have inelastic permanent deformation associated with compaction.

The evolution of the strain and stress in foam of density 384kg/m^3 when the initial length L=76 mm is shown in Figure 5.24. The stress contours indicate the emergence of an elastic wave, which is followed by the compaction front from the loaded end. Multiple reflections of both waves are evident in the contour plots. The reflection of the waves at the fixed end produces an increase in the stress amplitude of the wave, which travels in the opposite direction. The reflections at the free end produce a change in the phase of the stress wave. The strain contours indicate an increase in the strain with every reflection at the fixed end. Further, the strain along the entire length of the foam after multiple reflections indicates that the entire material has been loaded beyond ε_{Po}. The entire length of the foam exhibits permanent deformation associated with compaction of the material.

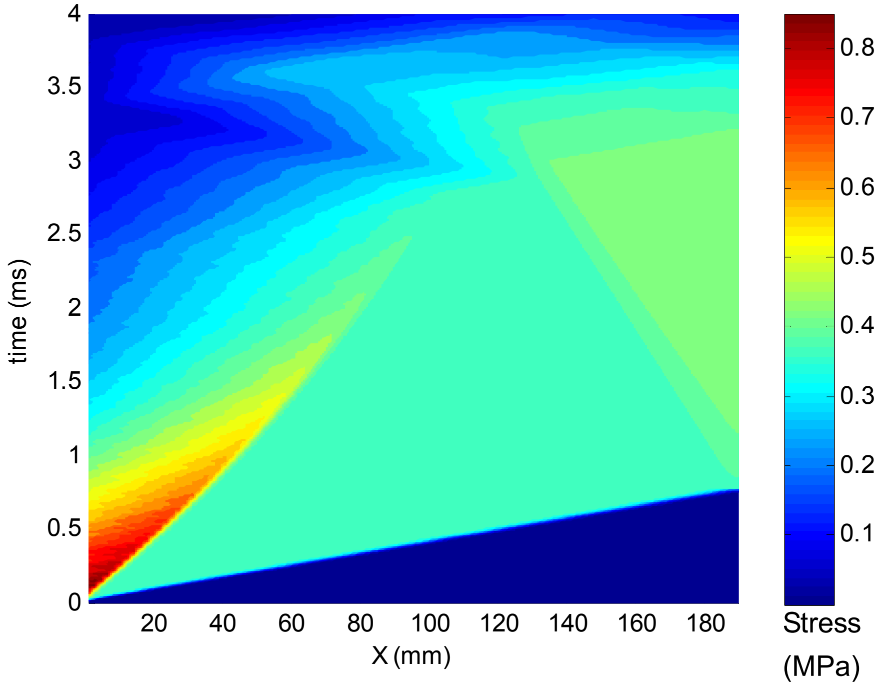

(a)

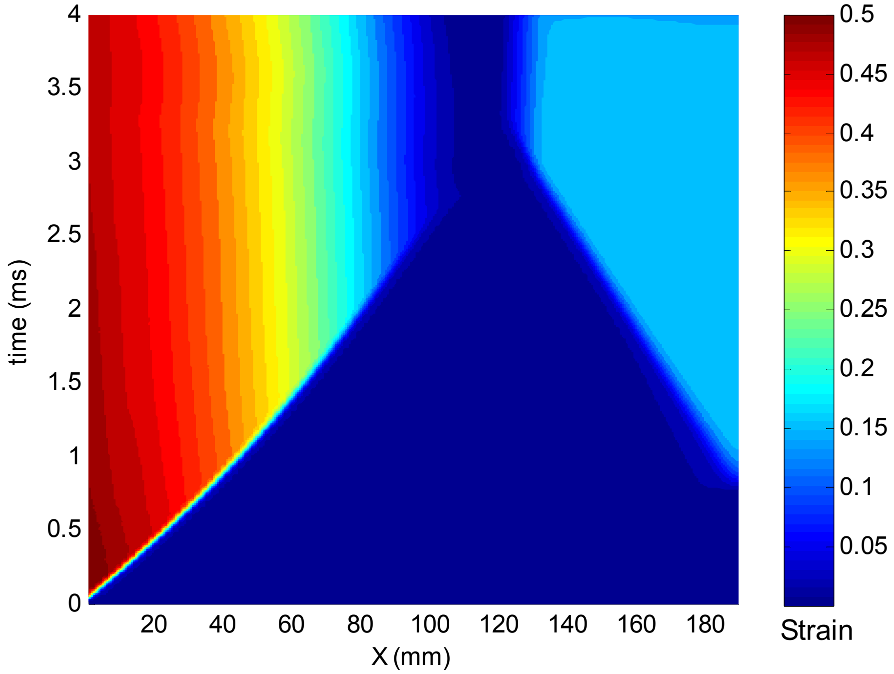

(b)

Figure 5.23: (a) Stress contour plot (stress unit: MPa) and (b) Strain contour plot for L>L_{cr} corresponding to Figure 5.22 (a).

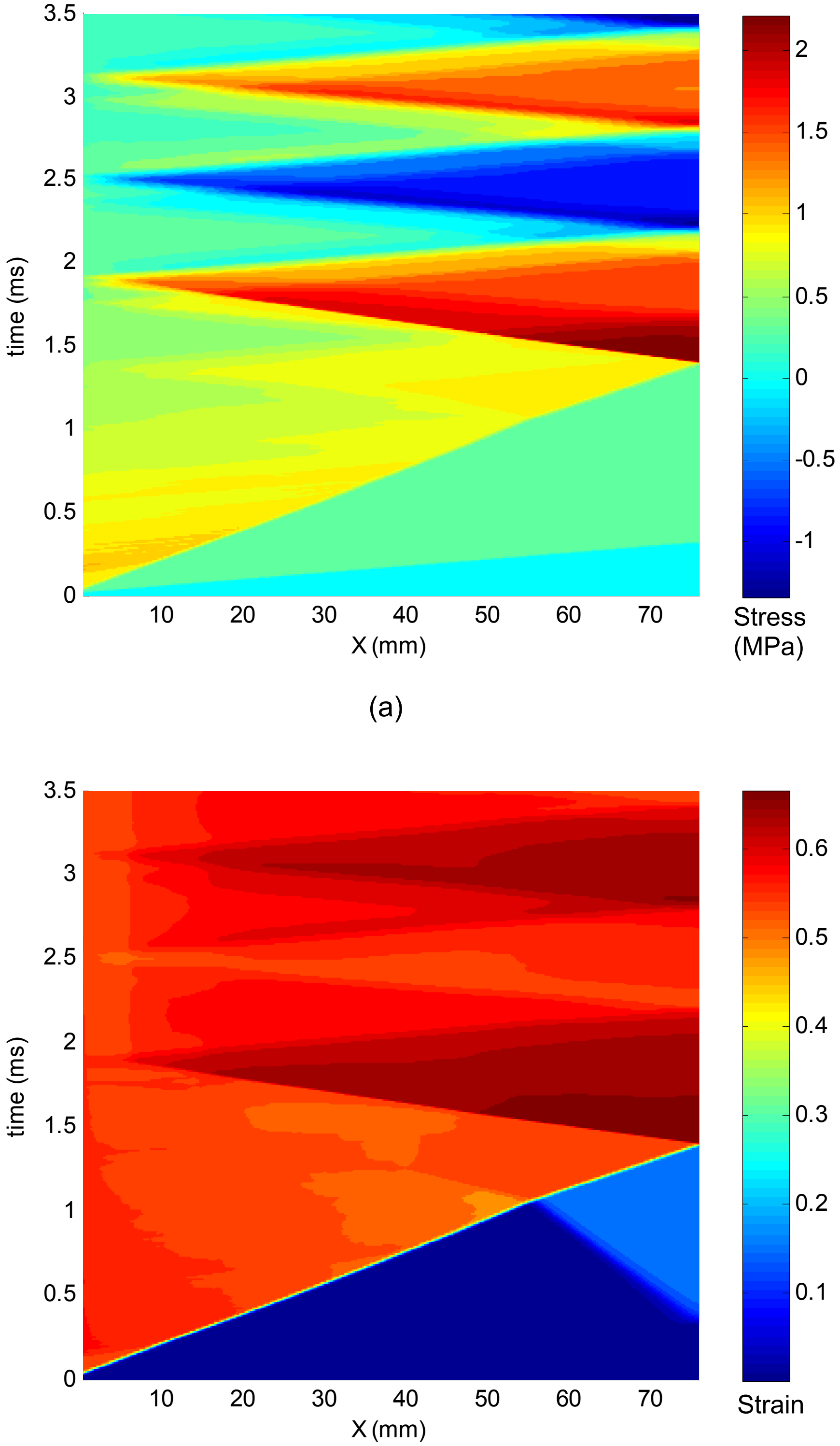

(a)

(b)

Figure 5.24: (a) Stress contour plot (stress unit: MPa) and (b) Strain contour plot for $L < L_{cr}$ corresponding to Figure 5.22 (b).

5.5.2. Prediction using the RPPL Idealization

When the actual strain-stress curve is idealized using the RPPL model, simplified solution procedures can be developed for predicting the dynamic response of the cement foam under blast loads. The procedure for determining the L_{cr} and transmitted stress for given foam was presented in Chapter 3.

The material response is idealized as a rigid, perfectly-plastic, locking (RPPL). Developing the RPPL idealization for the actual material response requires two key parameters, the densification strain (ε_D) and the crushing stress (σ_{po}). The densification strain ε_D, for the foams was estimated using the empirical formula provided by Ashby and Gibson (1999, p. 208)

$$\varepsilon_D = 1 - 1.4\left(\frac{\rho_f}{\rho_s}\right) \tag{5.1}$$

where ρ_f is the density of foam and ρ_s is the density of the base material. The density of the base material, which is a cement paste, is calculated knowing the proportion of the water to cement by weight (w/c ratio) and the specific gravity of cement (ρ_{cement})

$$\rho_s = \frac{1 + w/c}{\dfrac{1}{\rho_{cement}} + \dfrac{w}{c}} \tag{5.2}$$

where ρ_{cement} is the specific gravity of cement. Since the w/c ratio of the cement paste and the ρ_{cement} are equal to 0.55 and 3.2, respectively, ρ_s is equal to 1800 kg/m^3. Using Equation 5.1, ε_D is calculated to be equal to 0.70 and 0.63 for cement foams with $\rho_f = 384$ kg/m^3 and $\rho_f = 480$ kg/m^3, respectively. A comparison between the actual stress strain response and the RPPL idealization is shown in Figure 5.25.

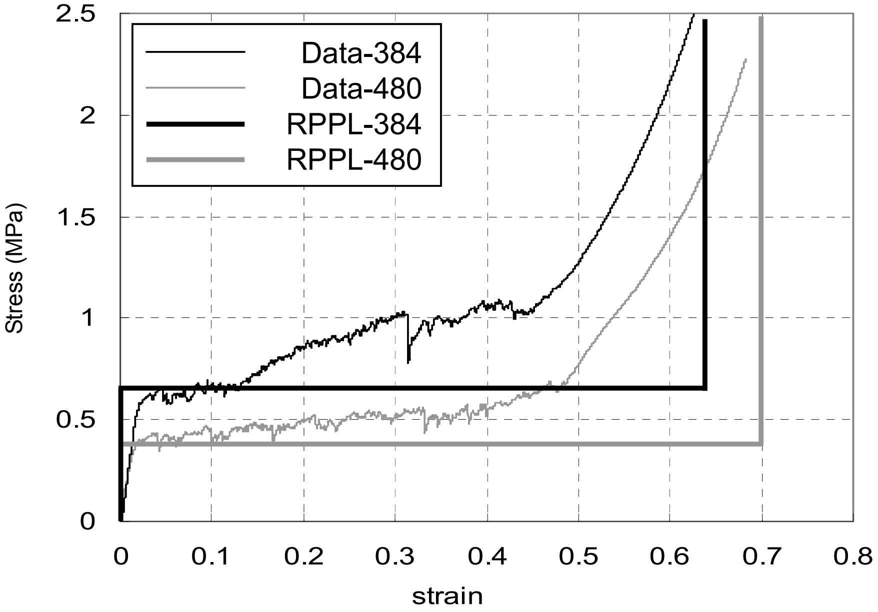

Figure 5.25: Actual stress-strain response and the RPPL idealization.

The experimental results for the case when $L > L_{cr}$ are compared with the predictions obtained using the RPPL model (see chapter 3 for details) in Figure 5.26. The foam transfers the applied blast pressure loading into a rectangular pulse with the amplitude equal to the crushing strength of the cement foam. The duration of the transmitted pulse, also known as the critical time T_c (defined in chapter 3), is determined using Equation 3.11. The duration of the transmitted stress using the shock model matches favorably with the experimental results. The critical length predicted by the RPPL model for the blast pressure input shown in Figures 5.26 (a) and (b) can be calculated using Equation 3.7 or 3.8 and are equal to 130 mm and 102 mm, respectively for the 384 kg/m^3 and the 485 kg/m^3 foams. The critical lengths of the foam obtained from the experiments were respectively equal to 203 mm and 178 mm. The shorter critical length is predicted using the RPPL idealization can be attributed to the inherent stiffer response of the RPPL model and the approximation in the ε_D. In the RPPL model, the initial elastic stiffness and the gradual increase in the stiffness in and the concave parts of the stress-strain curve are idealized as rigid with infinite stiffness. This results in an artificial increase in stiffness of the material and hence a smaller predicted critical length. It should be noted that the value of ε_D used in the RPPL model were obtained using the empirical formula proposed by Ashby and Gibson (1999, p. 208), which was calibrated using data from metal foams. As per the prediction of Equation 5.1, the cement foam with 384 kg/m^3 density, once compacted, reaches the densification strain equal to 0.7. From Figure 5.16, considering the distribution of strain along the length of the cement foam after compaction, the strain in the densified foam is equal to 0.4. When $\varepsilon_D = 0.4$ is used $L_{cr} = 170$ mm is obtained, which provides a better comparison with the L = 203 mm obtained from the experiments.

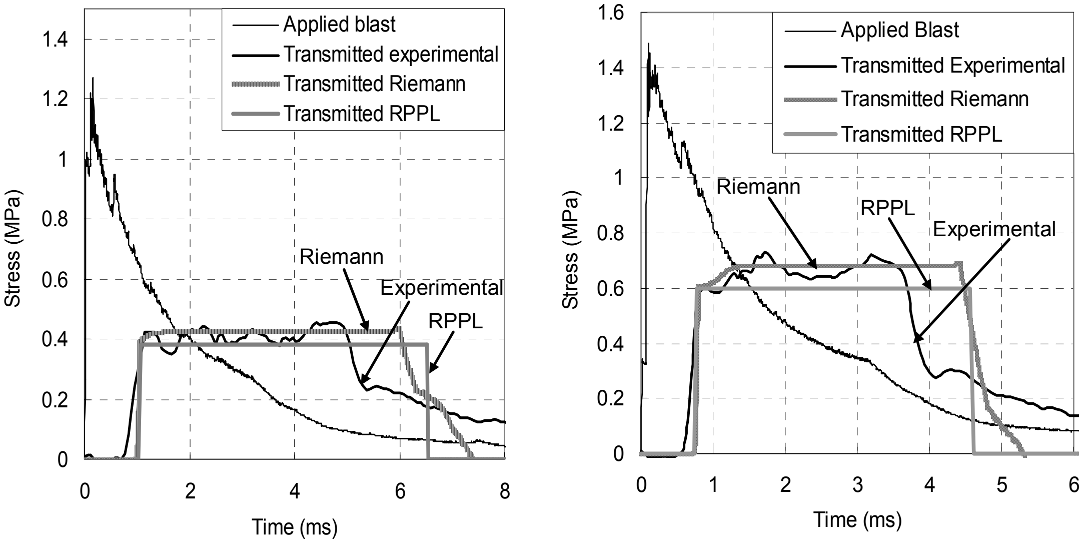

(a) (b)

Figure 5.26: Prediction of transmitted stress using the shock model and comparison to experimental results for L > Lcr: (a) 384 kg/m^3 and (b) 480 kg/m^3.

5.6. Discussion

The results of the experimental investigation and the numerical simulations clearly show that for each applied blast pressure loading, there exits a critical length of cement foam, L_{cr}, which depends upon the cement foam density. When $L > L_{cr}$, the blast load applied to the foam bar is transformed into a rectangular stress pulse at the target end. The magnitude of the transmitted stress is equal to the crushing strength of cement foam, σ_{po}, which is less than the peak blast pressure P_o, and therefore the cement foam reduces the peak stress delivered to the solid substrate to be protected. Both numerical methods, i.e. the finite volume method based on the exact Riemann formulation considering the actual stress-strain response of the foam and the the RPPL-model, provide accurate predictions of the transmitted stress through the foam bar. When $L < L_{cr}$, a stress enhancement, where a second jump in the magnitude of the transmitted stress following the initial rectangular shaped stress pulse is observed. The exact Riemann based finite volume method accurately predicts the history of the transmitted stress obtained after compaction of the foam. The RPPL model cannot be used in this case. In the following, the characteristics of the transmitted stress through the foam bar are discussed for $L>L_{cr}$ and $L<L_{cr}$.

5.6.1. The Transmitted Stress through Foam Bar when $L > L_{cr}$

The propagation of stress wave, which is generated by a blast load, inside a foam bar is clearly shown in Figures 5.23 and 5.24. The wave structure in the foam consists of an elastic precursor followed by a compaction front, which is immediately followed by a set of unloading wave. The reflection of elastic precursor at the right boundary produces the first rise in stress at the transmitted end, which is followed by constant stress amplitude. As the compaction front travels downstream, its amplitude decreases continuously, and eventually diminishes when its amplitude decrease to σ_{po}. The compaction front diminishes before the compaction wave reaches the transmitted end (right end) and causes no further reflection at the right end. Therefore, for the case corresponding to $L > L_{cr}$ the transmitted stress exhibits a rectangular shaped pulse with no further rise in stress.

The amplitude of the transmitted stress is calculated considering the reflection of an elastic precursor at a rigid fixed boundary. Figures 5.27 (a) and (b) show the waves and states in the foam immediately before and after the reflection of the elastic precursor at a rigid fixed boundary. In Figure 5.27 (a), the pre-wave state is denoted using subscript "1" and the post-wave state is denoted using subscript "2". State "2" corresponds to the initial critical stress (or the crushing strength), σ_{po}. The states are changed across the elastic precursor, which is a right running linear elastic wave. The particle velocity, v_2 is calculated using Equation 4.4 (the wave equation of the right running linear elastic wave) with the subscript R = 1 and R* = 2, which results in

$$v_2 = \frac{\sigma_{po}}{a_E \rho_o} \tag{5.3}$$

The elastic precursor reflects back as a compaction front and changes the pre-wave state "2" to post-wave state "3". $v_3 = 0$ because the right boundary is stationary. The stress immediately following the reflection, σ_3, which is the amplitude of the rectangular pulse, can be solved using Equation 4.10 (the wave equation of the left running compaction front) with the subscript L=2 and L*=3, given as

$$\Delta\sigma = \sqrt{\frac{\Delta\sigma / \Delta\varepsilon}{E}}\,\sigma_{po} \tag{5.4a}$$

where

$$\Delta\sigma = \sigma_3 - \sigma_{po} \quad \text{and} \quad \Delta\varepsilon = \varepsilon_3 - \varepsilon_{po} \tag{5.4b}$$

are the changes in stress and strain across the compaction front, respectively. σ_3 can be obtained from Equation 5.4. However, since ε is a function of σ (given by the stress-strain relation for the envelope curve), this results in a nonlinear algebraic equation. In the following, a simplified solution is developed to estimate the change in stress across the compaction front.

The numerator in Equation 5.4a, given by $\Delta\sigma/\Delta\varepsilon$, is the slope of the secant line connecting points "2" and "3" as shown in Figure 5.28. Considering the experimental data and the solution from the numerical simulations (Figure 5.20), it can be seen that there is a very small change in amplitude from σ_{po}, following reflection. Therefore, it can be assumed that the slope of the strain-stress curve does not change much with in the range (σ_{po}, σ_3). $\Delta\sigma/\Delta\varepsilon$ can be approximately taken equal to the slope of tangent at ε_{Po}.

$$\frac{\Delta\sigma}{\Delta\varepsilon} \approx \frac{d\sigma}{\Delta\varepsilon}\bigg|_{\varepsilon=\varepsilon_{po}} = AE\alpha\left(1-\varepsilon_{po}\right)^{-\alpha-1} \tag{5.5}$$

Substituting Equation 5.5 in Equation 5.4, Δσ can be obtained as

$$\Delta\sigma = \sqrt{\frac{A\alpha}{\left(1-\varepsilon_{po}\right)^{\alpha+1}}}\sigma_{po} \tag{5.6}$$

With the values given in Table 5.1, the amplitudes of the rectangular pulses in Figures 5.20 (a) and (b) are computed to be 0.420 MPa and 0.699 MPa, respectively for the cases corresponding to Figures 5.20 (a) and (b). These values compare favorably with the values of 0.425 MPa and 0.71 MPa obtained from the numerical simulation using exact Riemann based finite volume method.

It should be noted that the amplitude (σ_3) of the reflected stress wave is only determined by the properties of foam and is independent of applied stress. For typical foams, the slope of the strain-stress curve at the initiation of the concave response is much smaller than the initial elastic modulus, E. Therefore according to Equation 5.4, the $\Delta\sigma$ is small compared to σ_{po}. In other words, since A is a small value (1/350 for the 384 kg/m^3 foam and 1/250 for the 480 kg/m^3 foam), $\Delta\sigma$ obtained from Equation 5.6 is small compared to σ_{po}. The ratio $\Delta\sigma/\sigma_{po}$ are approximately equal to 10% for both cement foams. In the RPPL model, the change of stress $\Delta\sigma$ due to the reflection of the elastic precursor is omitted and the amplitude of the transmitted rectangular pulse is assumed to be the crushing strength of the cement foam σ_{po}. Since $\Delta\sigma$ is small compared to σ_{po}, the RPPL model also gives a favorable solution when L>L$_{cr}$.

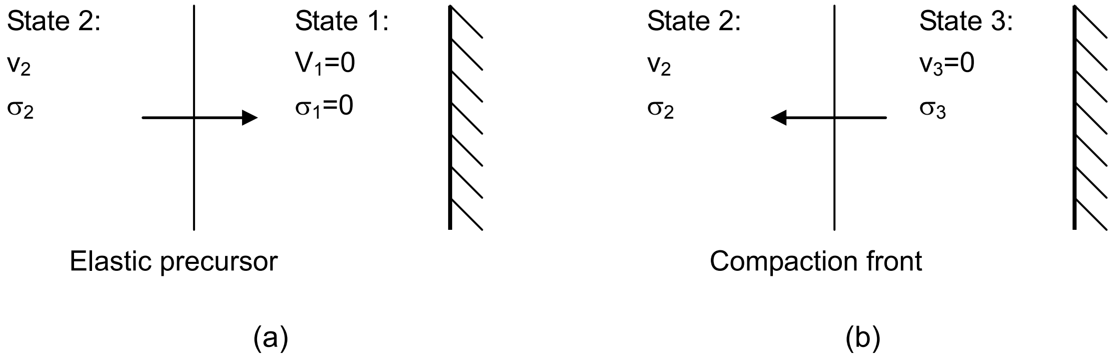

Figure 5.27: Pre- and post-wave state across a (a) elastic precursor (before reflection) and (b) compaction front (after reflection).

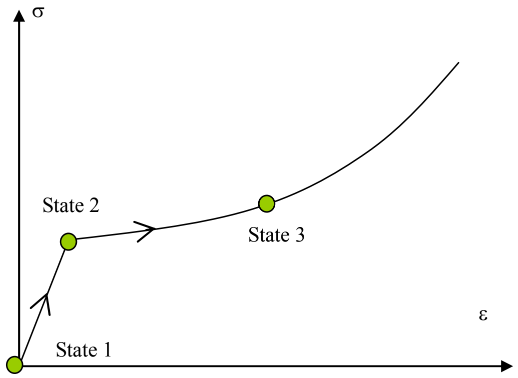

Figure 5.28: States of cement foam before and after the reflection of an elastic precursor.

5.6.2. Critical Length L_{cr} and Stress Enhancement when $L < L_{cr}$

When $L < L_{cr}$, there is an increase in the transmitted stress which could lead to enhancement above the applied blast pressure as the length is decreased. This is undesired for the purpose of blast mitigation. In the following, the numerical test with 110 mm foam bar in Figure 5.21 (a) is repeated to determine the reason for the stress enhancement. The stress induced in the foam bar at successive instants of time before the reflection of the compaction front is plotted in Figure 5.29. These results are obtained from the finite volume simulation using the exact Riemann solution developed in the previous chapter and the applied blast pressure shown in Figure 5.21 (a). In Figure 5.29 (a), the right running elastic precursor is followed by a compaction front. In Figure 5.29 (b), after reflection at the right boundary, the elastic precursor becomes a compaction front travelling in the opposite direction. Meanwhile the compaction front continues to travel to the right, its strength reducing with distance travelled. In Figure 5.29 (c), the right running compaction front is first strengthened after the reflection with the left running compaction front and its amplitude then continues to decrease due to attenuation produced by compaction of material. In Figure 5.29 (c), the last curve for $t = t_2 = 1338.7$ μs corresponds to the instant before the compaction front reflects at the right boundary. It is evident that although the compaction front has been reduced in amplitude as it traveled through the foam, its amplitude is around 1 MPa, which is significantly higher than the crushing strength of the foam. In comparison, for the case of $L > L_{cr}$ the compaction front completely diminishes before reaching the right boundary. It is the reflection of this compaction front that produces the stress enhancement.

The reflected stress produced by the right running compaction front at the right boundary can be calculated using wave relations. At the instant t_2, before the compaction front reflects at the right boundary, the state of the cement foam behind the compaction front is given as, σ_2=1.0 MPa; ε_2=0.55; v_2=23.5 m/s (measured from Figure 5.29 (c)). Referring to Figure 5.27 (b), state “2” is now the pre-wave state and “3” is the post-wave state of the reflected compaction front. The two states are related by the wave equation of the left running compaction front (Equation 4.10, with the subscript L=2, L*=3 and with v_3=0) given as

$$\Delta\sigma\Delta\varepsilon = v_2^2\rho_o \tag{5.7}$$

where

$$\Delta\sigma = \sigma_3 - \sigma_2 \tag{5.7a}$$

$$\Delta\varepsilon = \varepsilon_3 - \varepsilon_2 \tag{5.7b}$$

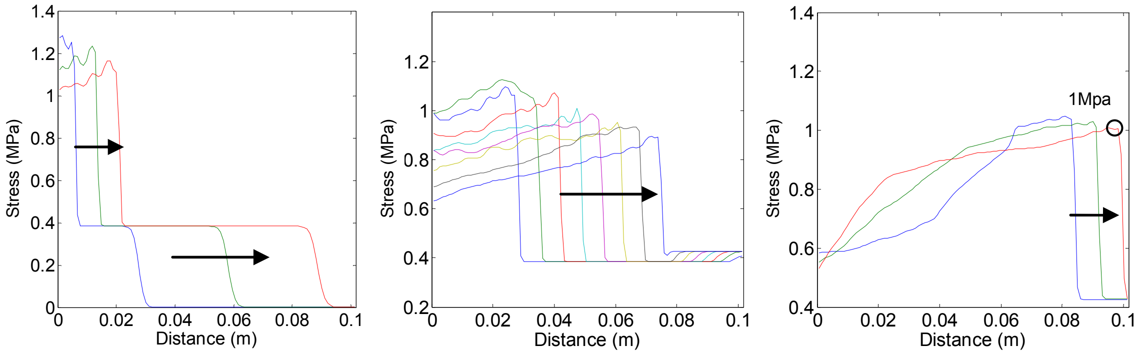

(a) (b) (c)

Figure 5.29: Stress in foam at a successive time between (a) t=119.5 ~363.3 μs; (b) t=485.2~1338.7 μs; (c) t=1485.0~1728.8 μs.

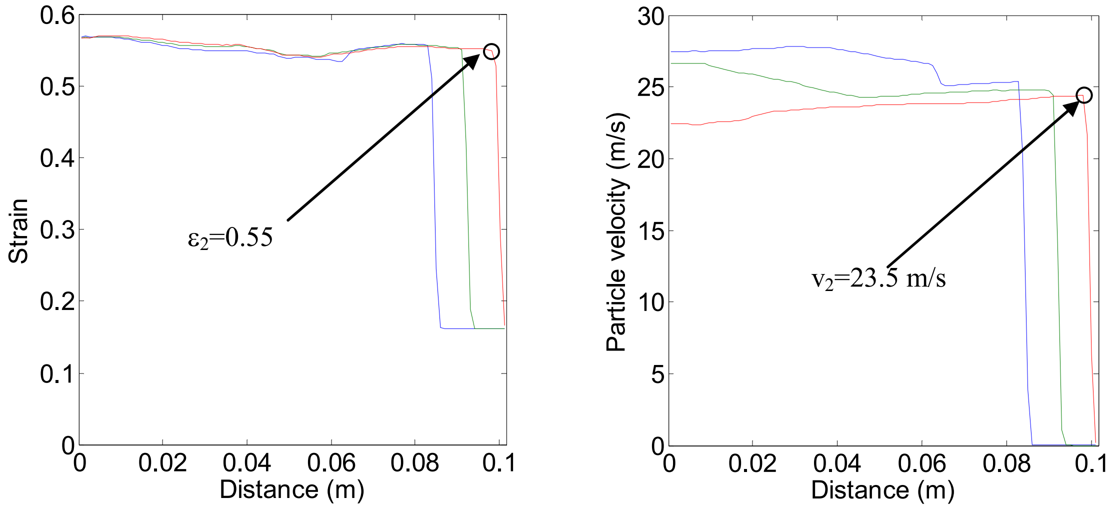

(a) (b)

Figure 5.30: (a) Strain and (b) particle velocity at a successive time between t=1485.0~1728.8 μs.

σ_3 and ε_3 are related by the stress strain relation of the foam given in Equation 5.1 for $\varepsilon_3 > \varepsilon_p$. For the given data σ_3, is calculated to be 2.46 MPa, which compares favorably with the measured peak transmitted stress of 2.38 MPa (in Figure 5.21 (a)). Equation 5.7 also implies that the overpressure $\Delta\sigma$ associated with the reflection, or the pressure enhancement, is related to the particle velocity v_2 induced by the incident compaction front produced by the applied blast load. It is therefore concluded that when **$L<L_{cr}$**, the compaction front does not diminishe before reaching the right boundary, which causes the part of cement foam adjacent to the boundary to impact at a velocity equal to the post-wave velocity on the boundary. The impact of the compacted foam, which travels like a projectile, results in the stress enhancement. The projectile effect is prominent as the length of foam sample decreases and so does the stress enhancement.

5.7. Conclusions

In this chapter the dynamic response of cementitious foams subjected to blast pressure loading is investigated experimentally. Two numerical methods, the exact Riemann based finite volume method and the RPPL model, are calibrated with the experimental results. Based on the results the following conclusions are drawn:

1. For foam with a given crushing strength, there exits a critical length Lcr, which is required to completely attenuate an applied blast pressure wave.
2. When the length of the foam, $L>L_{cr}$, the blast load applied at the loaded end of the foam bar is transferred as a rectangular shaped stress pulse at the target end. The magnitude of the transferred stress is nominally close, but slightly higher than the crushing strength of cement foam, σ_{po}. The impulse of the transmitted stress pulse is equal to the impulse of the applied blast pressure wave.
3. When $L<L_{cr}$, a second jump of transmitted stress following the initial rectangular shaped stress pulse, is observed. The enhancement of stress following the initial

plateau increases on decreasing the length. On decreasing the length of the foam, the stress enhancement exceeds the applied blast pressure amplitude.

4. The values of L_{cr} obtained from the RPPL idealization of the stress-strain curve of foam compare favorably with the experimental values. For $L>L_{cr}$, the RPPL model also gives accurate predictions of the transmitted stress through the foam and the densification strain in the material.

5. The exact Riemann based finite volume method gives accurate predictions of the transmitted stress through the foam bar for both $L<L_{cr}$ and $L>L_{cr}$.

6. When the applied blast pressure amplitude is higher than the crushing strength of the foam, the wave structure in the foam consists of an elastic precursor followed by a compaction front, which is immediately followed by a set of unloading wave. The predicted wave structure obtained from the exact Riemann based finite volume method compares favorably with the experimental observation. The first rise and subsequent plateau of the transmitted stress is generated by the reflection of elastic precursor at the boundary. The amplitude of the stress plateau is solely determined by the stress-strain response of foam and is independent of the blast load. The amplitude is theoretically higher than the crushing strength of foam, σ_{po} by an amount equal to the overpressure associated with the reflection of the elastic precursor at the boundary. The overpressure is negligible for foam type material which exhibit a nearly horizontal stress-strain response at the initiation of densification.

7. When $L>L_{cr}$, the compaction front diminishes before reaching the solid substrate and the transmitted stress is associated with the reflection of the elastic precursor. No amplification of stress is observed in this case.
8. When $L<L_{cr}$, the stress enhancement is produced by the reflection of the compaction front at the boundary.

Chapter 6: Design Guidelines for Foam Cladded Structure

6.1. Introduction

Blast mitigation strategies rely on a combination of passive methods such as offsets and other measures such as structural hardening. The first step in designing an effective strategy is to mitigate the effects of the blast by creating offsets. Usually, design of a facility is based on a perceived threat level (a specific bomb or source of explosion at a given standoff distance). Guidelines for performing threat assessment have been developed by FEMA (FEMA 2003). The fundamental goal of developing structural protective and hardening strategies is to improve the probability of survival of the facility for the given threat level. Protective strategies, such as the use of foam claddings and structural hardening measures are only effective when other preventative measures (such as detection, deterrence etc.) have failed and the threat is projected onto the facility over a distance permitted by protective measures such as barriers, which ensure a prescribed offset. In developing protective and other structural measures, designers work with a prescribed threat level. In order to develop design criteria from a projected threat, it is important to consider the response of the structural element under the imposed loading and the nature of resulting damage in the material.

The response of a structural element subjected to loading from an applied blast loading, evolves over time (Figure 1.2). In the short time scale, immediately following the incidence of the leading shock in the applied blast loading, stress waves are generated in the material. The stress waves travel at velocities which are in the order of a few thousand meters per second and produce a very rapid stress change associated with the motion of particles in the medium. When the stress waves reach the boundaries of the structural element or intersect each other, reflected stress waves are generated. The reflection of stress waves may produce higher stresses or a change in phase of the stress (compression changes to tension) in the material. A large stress associated with the stress wave resulting from a blast of large amplitude may result in a significant material damage associated with cracking, scabbing or spalling in the materials with low tensile strength. Structural elements made of reinforced concrete or brick masonry (brittle material) are particularly susceptible to such damage mechanisms. Material damage due to stress wave propagation, in the very short time scales, is less likely in steel structures because of the high yield stress in both compression and tension.

The response of a structural element following blast wave incidence evolves with time. Driven by the blast loading, the structural element starts to deflect and develop a deflected profile. The time associated with structural motion is in the order of the natural period of the entire structural element. Within this time frame, multiple reflections of stress waves and the accompanied stress changes occur before the deflection of structural element becomes significant. The maximum stress resulting from deflection of the structural element is localized at the some critical locations along the length of the structural element, usually associated with locations of high load effects such as bending moment. These locations depend upon the boundary conditions and any other constraints imposed on the structural elements. Localized damage in the form of plastic hinges or compression zones form at these critical locations and may lead to the final collapse of the structural element with increasing deflection due to continued loading.

Considering the two time scales in the blast response of a structural element, damage in the material can occur in the very short time scale due to stress wave propagation, in the longer time scale from the structural motion, or, a combination of both. The failure of the structural element happens when the damage in the material reaches a critical level. The relative importance of the damage at the different time scales to the structural response and failure depends upon several factors such as the pressure amplitude of the applied blast loading, the magnitude of the stress wave produced in the material to the strength of the material, the duration of the applied blast loading and the time period of vibration of the structural element. The choice of the procedure for blast analysis of a structure therefore requires consideration of the two time scales.

In conventional analysis, the response of the structures subjected to blast loads is determined using equivalent single or multi degree of freedom system. The characteristics of the equivalent system such as mass, stiffness and damping coefficient are derived from the vibrational characteristics of the structural element. The simplest representation consists of deriving an equivalent single degree of freedom (SDOF) system where the force-displacement function and damping coefficient are all converted from the original structure based on an assumed deformed shape of the structure, usually obtained form the static response. The damage in the material is a result of the deformation of the structure and damage due to stress-wave propagation is ignored. A displacement-based criterion based on a threshold value of structural displacement can be prescribed to evaluate the level of distress. This approach would therefore be suitable when the stress wave amplitude is lower than the threshold stress which would produce damage in the material or in materials with very high threshold for material damage such as steel. Steel exhibits elastic behavior, and hence no material damage up to its yield stress. The yield stress of structural steel is typically 240 MPa and higher, which is significantly higher than blast pressure amplitudes of concern. Blast with pressure amplitudes which are insignificant compared to the yield stress of steel could however produce significant loading considering the exposed area of the structural element, which in turn could produce significant deflection. Therefore, in steel structures, the stress wave created by most realistic blasts would not generate immediate damage in the material in the short time scale and the structure response would be elastic until localized damage associated with plastic hinges develops. The vibrational characteristics of the structure would therefore not be influenced by the short-time scale.

In cases where the damage is associated with structural motion, the vibrational response of the structure can be predicted using a non-linear load-displacement response which accounts for the localized non-linear behavior. Using a critical deflection parameter, y_c, the combinations of blast pressure amplitude and duration, which produce failure are plotted using the pressure-impulse (p-i) diagram. In this approach, which has been adopted in many design codes, the failure of structure is only controlled by the maximum deflection and the damage due to the stress wave propagation is ignored.

In structures made of quasi-brittle materials, such as concrete and masonry, which have a very low tensile strength, there is high probability of damage associated with wave propagation. The failure in this case is affected by both mechanisms. This can be illustrated considering the response of a reinforced concrete beam subjected to blast pressure loading. It has been shown that severe spalling and the associated loss of section is observed at the short time scales associated with wave propagation before noticeable structural deflection. The degraded element continues to deflect under applied pressure loading and eventually breaks down when significant deflection has been observed (Figure 6.1 [YI 2009]). The degraded structure exhibits significant damage in the material across its length before the beam starts deflecting and therefore its response in the large time scale should have different characteristics from those of the original structure if modeled using equivalent SDOF obtained from static response. Material degradation in the short time scale may cause the final failure to happen before the degraded structure reaches the critical deflection defined by the static response. Such a structure, when subject to a strong blast wave, may even fail due to excessive material damage produced by the high amplitude stress wave generated in the material. If the material damage due to stress waves in the short time scale is very severe it will cause the structure to fail before the deflection of the entire structure starts to develop. The damage produced by wave propagation would be distributed along the length of the structure as opposed to localized damage produced by structural motion. In either case, direct failure or degradation of structure, the effect of stress wave in the short time needs to be considered carefully in the analysis of brittle structure subjected to blast loads. Approaches such as the classical equivalent SDOF approach that only consider the deflection in the large time scale are not suitable for such cases. The possible loss of structural capacity resulting from the cracking or spalling would alter the equivalent parameters based on the original structure, but it is not considered in this approach. The failure of the structure, as is adopted in the development p-i diagram widely used in the blast design, is only controlled by a prescribed critical deflection y_c. This approach does not acknowledge any material damage in the short time scale associated with wave propagation, which can occur before the motion of the structure commences.

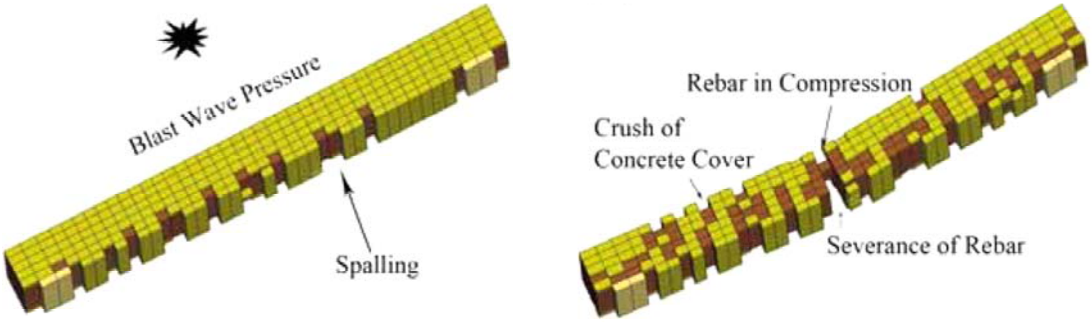

(a) (b)

Figure 6.1 (a) spalling due to stress wave reflection at back face at a short time scale and (b) final structural failure associate large deflection at a long time scale [YI 2009].

When structural elements made of brittle material are required to resist blast loads of high amplitudes, damage induced by stress wave effects needs to be reduced or prevented in the development of any blast mitigation strategy. Foam is proposed to be use in the blast mitigation for such a purpose. Based on the discussion of pervious chapters, foam is effective in reducing the transmitted stress in the structural element if its length is greater than the required critical length, L_{cr}. Use of foam for blast mitigation has been studied before. However, most of the previous work has focused on developing guidelines for the use of foam in blast mitigation using a single degree of freedom system which uses a displacement based criterion [Ma and Ye 2007; Ye and Ma 2007]. The effect of foam in reducing the structural deflection in the large time scale by comparing iso-damage curves for structures with and without foam were studied using the conventional p-i diagram. Only the damage controlled by the maximum structural motion is considered in this approach and the magnitude of the transmitted stress wave, σ_o, is not explicitly considered.

Clear guidelines for using foam in the protective design again blast loading have not been established.

This chapter aims to develop a design guideline for using foam in a protective strategy for a prescribed level of projected threat from a blast. It is proposed that the use of foam in the blast mitigation is to protect the structural elements made of quasi-brittle material, such as reinforced, un-reinforced concrete or masonry. The proposed design approach includes a two step process and considers damage mechanisms in two time scales associated with stress wave propagation and structural motion. In the short time scale, the role of the cement foam is to reduce the magnitude of the stress wave in the structural element by attenuating the blast wave and therefore reducing the possible material damage. In the long time scale, the maximum deflection of protected structure needs to be checked using a p-i diagram. Because the foam changes the characteristics of the applied blast pressure wave into a rectangular pulse, which is applied on the structure, an approach to check the maximum deflection using the p-i diagram for rectangular pulse is developed. Finally a design example is presented and the effect of foam in increasing the resistance of a structural element against blast loads in both time scales is clearly illustrated on a p-i diagram.

6.2. Development of Design Procedure

In this section, guidelines for the use of foam in a protective strategy, for a structural element against a projected threat of a prescribed level considering both stress and displacement criteria, are developed. It is implicitly assumed that the projected threat level for developing the desired level of protection is available. The objective of developing the guidelines for the use of foam is to minimize the damage in the material from the projected threat on the structural element. In the proposed procedure, damage in both time scales are considered. Considering two criteria, a two-step approach is proposed. The first step is to ensure that the structure meets the stress criteria and the second step provides a method to check the deflection criteria. This two step procedure is illustrated in Figure 6.2.

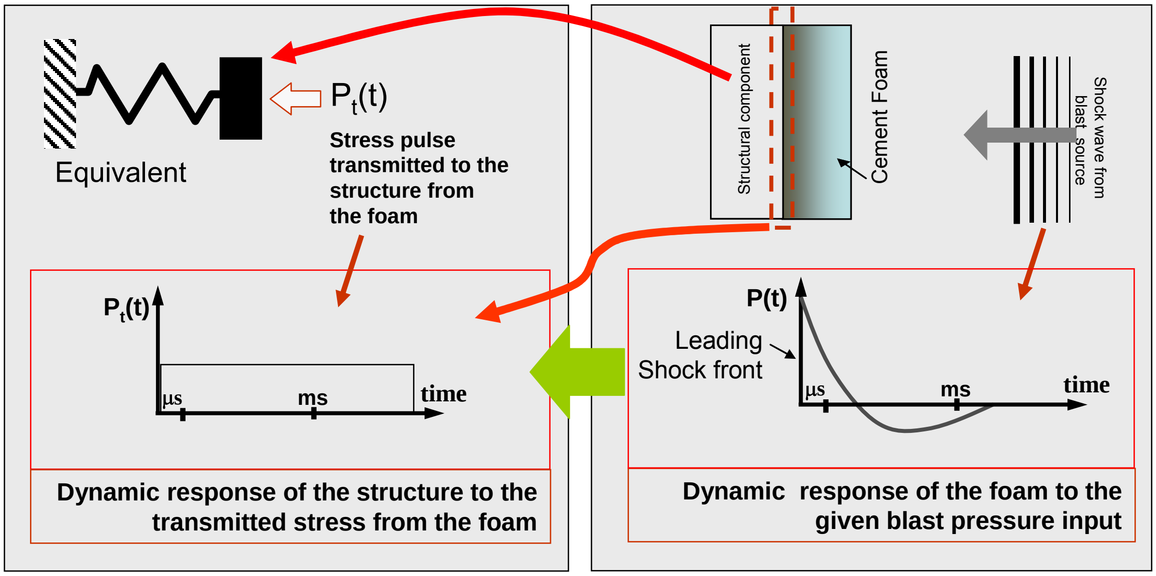

Figure 6.2: Schematic representation of the two step process.

6.2.1 Control the Stress (Stress Criteria)

In this step, the properties of foam, which would reduce the level of transmitted stress in the material to an acceptable level, are determined. The role of the foam is to reduce material damage in the short time frame associated with the wave propagation in the material. Based on the findings in pervious chapters the foam transforms the applied blast pressure history into a rectangular stress pulse of a constant magnitude equal to its crushing strength, σ_{po}. To ensure the transmitted stress is lower than the allowable stress of the protected element, σ_{po} should be determined such that,

$$\sigma_{po} = k_\sigma \sigma_{as} \qquad (k_\sigma<1) \tag{6.1}$$

where σ_{as} is the allowable stress of the structural element made of brittle material, such as concrete and masonry and $k_\sigma<1$ is a safety factor. The other properties of cement foam, the densification strain, ε_D and density ρ_f are functions of σ_{po} and thus be determined.

For a projected blast threat of a prescribed magnitude and duration, there exits a critical length L_{cr} for a given foam, which would fully attenuate the blast wave; L_{cr} is the minimum length of foam required to fully transform the applied blast pressure history to a rectangular pulse. In foam-cladded structures, it is important to choose a length larger than L_{cr} in order limit the intensity of transmitted stress wave to the structural element. It has previously been shown that the RPPL idealization for the stress-strain response of the foam provides accurate determination of the dynamic compaction response of foam for length larger that L_{cr} for the given applied blast pressure loading. With the foam parameter given, L_{cr} corresponding to a given blast load can also be determined analytically using the RPPL model. According to RPPL model, when foam is subjected to applied blast pressure loading, the compaction stops when the velocity of compacted foam becomes equal to zero. This condition has previously been derived in Chapter 3 (Equation 3.10), and it leads to a condition for the end of compaction, given as

$$M(T_c) = 0 \tag{6.2}$$

where $t = 0$ represents the time when blast pressure loading is applied on the foam and $t = T_c$ is the critical time corresponding to the end of compaction. At $t = T_c$, the displacement of the loaded end reaches its maximum value, u_{fc}, and the corresponding length of foam bar being compacted (measured from its original configuration) is L_{cr}. For foam of a given crushing strength, σ_{po}, L_{cr} is also the minimum length required for completely absorbing the impulse of a given incident applied blast loading.

When t < T_c, u_f is calculated using Equation 3.7. When $t > T_c$, $u_f = u_{fc}$ is a constant and is computed by setting t = T_c in Equation 3.7, where T_c is obtained from Equation 6.2. Also, $L_{cr} = u_{fc}/\varepsilon_D$ (according to Equation 3.1). L_{cr} can be obtained from Equation 3.7 with $t = T_c$ and is given as

$$L_{cr}^2 = \frac{2}{\rho_f \varepsilon_D} \int_0^{T_c} \int_0^{\eta} \left(p(\tau) - \sigma_{po}\right) d\tau d\eta \tag{6.3}$$

Lcr can be obtained if the applied pressure history p(t) is known.

A blast loading of triangular profile is considered

$$p(t) = \begin{cases} P_o\left(1 - \dfrac{t}{T_o}\right) & t \le T_o \\ 0 & t > T_o \end{cases} \tag{6.4}$$

where T_o and P_o are the duration and the amplitude of the applied blast loading, respectively. For the assumed blast pressure profile T_c is determined from Equation 6.2 and is given as

$$T_c = \begin{cases} 2T_o\left(1 - \dfrac{\sigma_{po}}{P_o}\right) & \dfrac{1}{2} < \dfrac{\sigma_{po}}{P_o} < 1 \\ \dfrac{T_o}{2}\dfrac{P_o}{\sigma_{po}} & \dfrac{\sigma_{po}}{P_o} \le \dfrac{1}{2} \end{cases} \tag{6.5}$$

Substituting Equations 6.4 and 6.5 in Equation 6.3, the critical length is obtained as

$$L_{cr} = \begin{cases} \dfrac{4}{\sqrt{3}} i_L \left(1 - \dfrac{1}{p_\sigma}\right)^{\frac{3}{2}} \left(\dfrac{1}{p_\sigma}\right)^{\frac{1}{2}} & 2 > p_\sigma > 1 \\ i_L \left(1 - \dfrac{4}{3p_\sigma}\right)^{\frac{1}{2}} & p_\sigma > 2 \end{cases} \tag{6.6}$$

where

$$p_\sigma = \frac{P_o}{\sigma_{po}} \tag{6.7}$$

and

$$i_L = \frac{i_o}{\sqrt{\rho_f \varepsilon_D \sigma_{po}}} \tag{6.8}$$

With the foam parameters obtained from last step, L_{cr} for given blast loadings (P_o, T_o) or equivalently (P_o, i_o) can be calculated from Equation 6.6. Equation 6.6 can be recast in the following form,

$$i_L = \begin{cases} \dfrac{\sqrt{3}}{4} L_{cr} \left(1 - \dfrac{1}{p_\sigma}\right)^{-\frac{3}{2}} p_\sigma^{\frac{1}{2}} & 2 \geq p_\sigma > 1 \\ L_{cr} \left(1 - \dfrac{4}{3p_\sigma}\right)^{-\frac{1}{2}} & p_\sigma > 2 \end{cases} \tag{6.9}$$

Equation 6.9 provides inter-relations between the applied blast pressure parameter, P_o and i_o and L_{cr} of the foam with a given σ_{po}. This can be plotted using the normalized parameters, p_σ and i_L as shown in Figure 6.3. Each value of L_{cr} defines, according to Equation 6.9, an iso-damage curve on the p_σ-i_L diagram. Any applied blast loading in the area below one curve (defined by one value of L_{cr}) can be completely attenuated by the foam. With the parameters of blast loadings (P_o, i_o) normalized by foam parameters, the p_σ-i_L diagram is unique for all foams. The p_σ-i_L diagram can now be used as a design aid in selecting the minimum length/thickness of foam for the prescribed projected blast loading defined by by blast pressure amplitude and duration, P_o and i_o (assumed to be known).

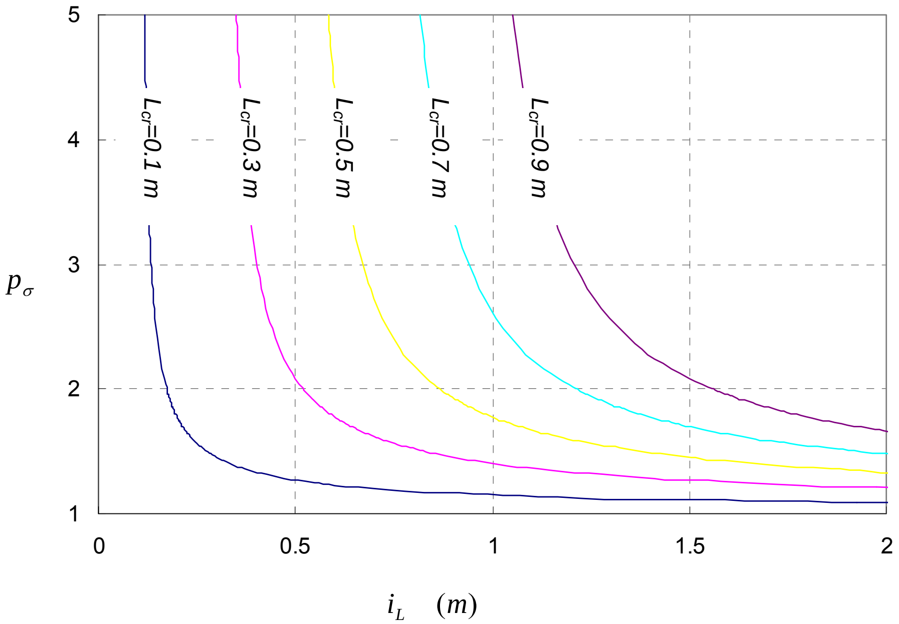

Figure 6.3: p_σ-i_L diagram for required foam length

The role of the foam in changing the applied blast pulse to a rectangular transmitted pulse can also be clearly illustrated by considering foam of length equal to L_{cr} for pressure inputs on the p_σ-i_L diagram as shown in Figure 6.4. The amplitude of the transmitted stress after foam compaction would be equal to the crushing strength of the foam, σ_{po}. The impulse of the transmitted stress remains the same as the impulse of the applied blast loading, i_o. The transmitted pulse is plotted on the p_σ-i_L plot as a straight line with constant p_σ value equal to 1.0 for all values of i_L. It should be noted that the transmitted rectangular pulse corresponding to $p_\sigma = 1.0$ is the same as the applied loading to the structure and should be used for evaluating its structural response.

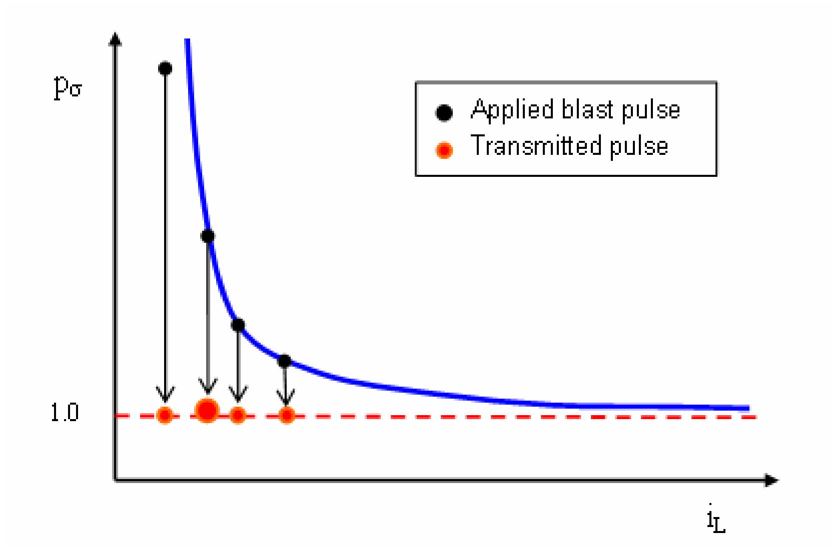

Figure 6.4: Representation of stress transmitted through the foam and applied on the cladded structures on the p -iL diagram.

6.2.2 The Deflection-based Evaluation of the Structural Response to Transmitted Stress (Deflection Criteria)

In a foam cladded structure, the motion produced by the transmitted rectangular stress pulse from the foam can produce damage and eventually lead to failure. The damage in the material resulting from structural motion would be localized at points of high load effect (such as a plastic hinge). Failure is often associated with critical value of a displacement measure such as maximum deflection (or some equivalent deflection parameter such as maximum angle of rotation). Combinations of pressure amplitude and impulse which would produce failure are conveniently represented using the conventional p-i framework with a threshold displacement-based failure criterion (pressure-impulse diagram).

Using a displacement-based failure criterion, the p-i diagram represents an iso-damage critical state in non-dimensional loading parameter coordinates where a characteristic curve separates the damaged and undamaged states [Li and Meng, 2002]. In this method, the actual structural motion caused by the distributed blast loading is described by a SDOF lumped spring mass system, also-called the equivalent system [Biggs 1964, Smith and Hetherington 1994 and TM5-1300], and the structural damage is controlled by the critical structural deflection, y_{max}, which is determined from the static response of the structural element to applied distributed loading. An equivalent system based on an anticipated mode of response has been widely accepted to be suitable for predicting the dynamic response of structures subjected to blast loads because of its efficiency and realistic representation of the structural behavior. The p-i diagram has been shown to be influenced by the shape of the blast pressure wave [Li and Meng, 2002].

When cement foam with length, $L > L_{cr}$ is used, the resultant loading acting on the structural element after the compaction of the foam is a rectangular pulse with magnitude equal to the crushing strength of the foam (according to RPPL). Considering the transmitted stress obtained from the foam, the p-i diagram for a structural element is developed for a rectangular stress input following the earlier development by Li and Meng [2002]. In the formulation, the damping effect is ignored for studying the structural response under a pulse load with short duration. The overall structural behavior is dominated by the elastic response. The equivalent SDOF structural model is described by the following equilibrium equation:

$$m\ddot{y} + ky = \sigma_{Po} f(t) \tag{6.10}$$

where m=equivalent lumped mass per unit area; k= equivalent structural stiffness per unit area; y=deflection and f(t)= pressure function given as

$$f(t) = \begin{cases} 1 & t < T_o \\ 0 & t \geq T_o \end{cases} \tag{6.11}$$

T_o is the duration of the rectangular pulse, which is related to the impulse, i_o ($T_o = i_o/\sigma_{po}$)

The initial conditions are:

$$y(t = 0) = 0 \tag{6.12a}$$

$$\dot{y}(t = 0) = 0 \tag{6.12b}$$

It has been shown that the relative maximum deflection of a structure is uniquely determined for a given loading shape as [Li and Meng, 2002],

$$\frac{y_{max}}{y_c} = g(p, i) \tag{6.13}$$

where y_{max} is the maximum displacement of the equivalent SDOF system, which is normalized by y_c=critical characteristic structural deflection of a structure associated with a given level of damage. p and i are two non-dimensional quantities, the peak applied pressure, σ_{po} and impulse, i_o, normalized by structural parameters and y_c given as

$$p = \frac{\sigma_{po}}{y_c k} \tag{6.14a}$$

$$i = \frac{i_o}{y_c \sqrt{mk}} = p\tau_o \tag{6.14b}$$

where

$$\tau = \frac{t}{\sqrt{m/k}} \tag{6.15a}$$

$$\tau_o = \frac{T_o}{\sqrt{m/k}} \tag{6.15b}$$

Each value of y_{max}/y_c corresponds to a certain structural damage level and defines, according to Equation 6.13, a critical iso-damage curve for the given damage level on the p-i diagram.

The solution of Equations 6.10 and 6.12 is given in many textbooks of structural dynamics (Biggs 1964). It is given in non-dimensional form as

$$\frac{y(\tau)}{y_c} = p\int_0^{\tau} f(\varsigma)\sin(\tau - \varsigma)d\varsigma \qquad (6.16)$$

y/y_c reaches the maximum value y_{max}/y_c at $\tau=\tau_m$ when $dy/dt=0$, i.e.

$$\sin\tau_m \int_0^{\tau_m} f(\varsigma)\sin\varsigma d\varsigma + \cos\tau_m \int_0^{\tau_m} f(\varsigma)\cos\varsigma d\varsigma = 0 \qquad (6.17)$$

τ_m is first solved for form Equation 6.17. The maximum non-dimensional deflection y_{max}/y_c is obtained by substituting $\tau=\tau_m$ in Equation 6.16. If $y_{max}/y_c=1$ is chosen, one iso-damage curve on p-i diagram corresponding to the damage level defined by y_c can be developed. The value of p on the p-i diagram is obtained as

$$p = \frac{1}{\int_0^{\tau_m} f(\varsigma)\sin(\tau_m - \varsigma)d\varsigma} \qquad (6.18)$$

For loading function f(t) defined in Equation 6.11, τ_m is given as,

$$\tau_m = \begin{cases} \pi & \tau_o \geq \pi \\ \dfrac{\pi + \tau_o}{2} & \tau_o < \pi \end{cases} \qquad (6.19)$$

Substituting Equation 6.19 in Equation 6.18, p is given as

$$p = \begin{cases} \dfrac{1}{2} & \tau_o \geq \pi \\ \dfrac{1}{2\sin\left(\dfrac{\tau_o}{2}\right)} & \tau_o < \pi \end{cases} \tag{6.20}$$

The value of i on the p-i diagram is computed using Equation 6.14b.

The p-i diagram for the rectangular shape is plotted in Figure 6.5. The stress amplitude and impulse of the transmitted pulse (σ_{po}, i_o) are normalized using Equations 6.14 a and b to obtain the corresponding values of (p, i) on the p-i diagram. If all points are under the iso-damage curve of a specified damage level the maximum deflection of the structure y_{max} is small than prescribed y_c, or equivalently the deflection criteria is satisfied. Otherwise the deflection criterion is violated. If the deflection criteria is not satisfied based on the p-i diagram the structural element needs to be hardened to increase stiffness or mass. Methods such as attaching FRP sheet at faces of structural elements can be adopted but it is not in the scope of the current dissertation study.

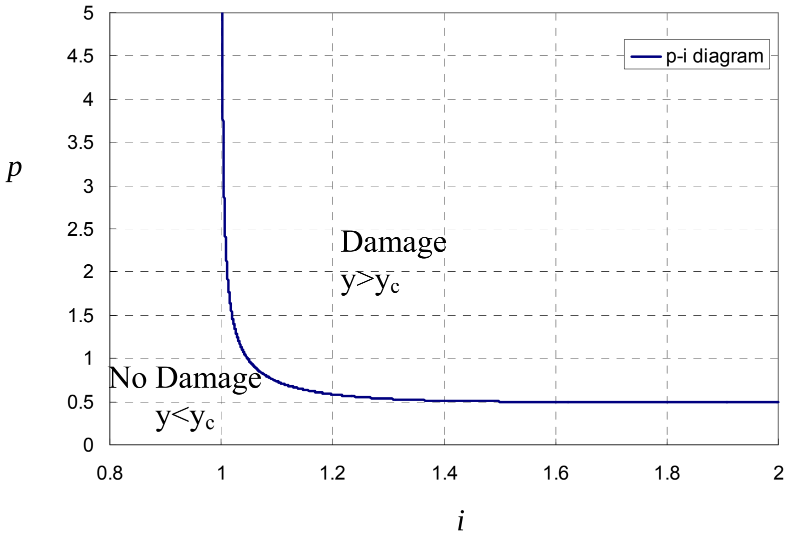

Figure 6.5 pressure-impulse diagram for rectangular pulse.

6.3. A Design Example

The use of the two-step procedure is now illustrated using an example of a reinforced concrete beam (Figure 6.6) subjected to blast loading. Properties of the concrete beam are summarized in Table 6.1. A detailed finite element analysis of the dynamic response and the failure mechanisms of this beam have been performed using DYNA and selected results of the simulation subject to blast loads at different time instants are shown in Figure 6.1 [Yi 2009]. Figure 6.1 (a) shows significant spalling of beam before the final complete failure of the beam (Figure 6.1 (b)) associated with crushing of the compression zone of concrete due to large deflection of beam. The spalling of concrete due to the stress wave reflection at the back face significantly degrades the load resistance of beam and leads to the final failure at large deflection. And therefore retrofitting the beam by attaching cement foam is considered to reduce the intensity of stress wave generated in the beam and suppress the spalling at the back face.

The beam is converted to an equivalent SDOF spring-mass system [Smith and Hetherington 1994 page 203] with k = 5.38e8 N.m/m^2 and m = 193.53 kg/m^2. The applied blast loading are assumed and are given in Table 6.2.

Calculations are performed for the above structure to withstand the five given blast loads according to the procedures outlined in section 6.2. In the first step the required length and crushing strength of foam are determined. The allowable stress of the reinforced concrete beam σ_{as} is assumed to be equal to the tensile stress of concrete (3.27 MPa). Choosing $k_\sigma = 1$, the crushing strength of the foam can be determined as $\sigma_{po} = \sigma_{as} = 3.27$Mpa. ε_D and ρ_f are related of σ_{po}. $\varepsilon_D = 0.5$ and $\rho_f = 60$ kg/m^3 are assumed.

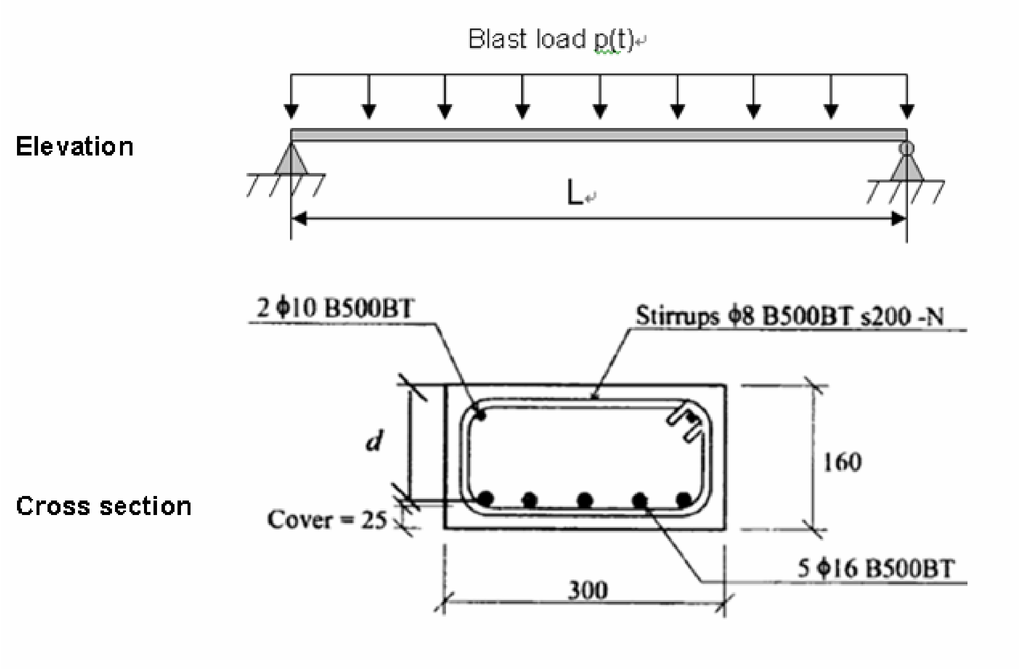

Figure 6.6: A simply supported beam under uniform blast loads [Yi 2009, page 99]

Table 6.1 Elastic properties of the Beam in Figure 6.6

Items	Values (Metric)
Length L	1500 mm
Width B	300 mm
Height H	160 mm
Elastic modulus E	26 Gpa
Density ρ	2400 kg/m^3
Compressive strength f_c'	27.6 Mpa
Tensile strength f_r	3.27 Mpa

Table 6.2: Identified blast pressure loads

Blast load	Peak pressure P_o (MPa)	Impulse per unit area i_o (kPa.s)
1	6	3.3
2	7.7	3
3	5	2.8
4	10	2.5
5	9	2.0

The given blast parameters are normalized according to Equations 6.7 and 6.8 and the results are given in Table 6.3. The normalized blast loads in Table 6.3 are plotted on the P_σ-i_L plot for the foam with the given characteristics as shown in Figure 6.7. From the graph, it is evident that the minimum length of foam required to completely attenuate the applied blast pressure loads is 0.2 m.

Table 6.3: Normalized blast loads according to Equations 6.7 and 6.8.

Blast load	p_σ (Equation 6.6)	i_L (Equation 6.7)
1	1. 835	0.333
2	2. 355	0. 303
3	1. 529	0. 282
4	3. 058	0. 253
5	2. 752	0. 202

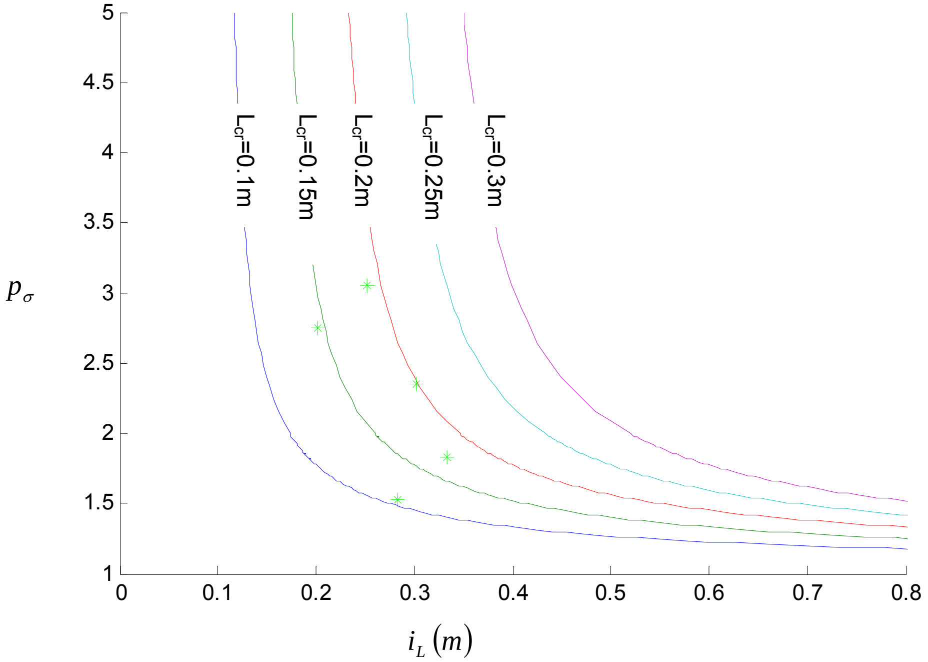

Figure 6.7: Applied blast loads plotted on the P_σ-i_l plot

The second step in the process consists of checking the displacement criterion. The p-i diagram of the structure assuming linear elastic response up to the critical displacement is shown in Figure 6.8. The critical displacement, y_c, which is taken as the initiation of failure was assumed to be equal to 10 mm. The characteristics of transmitted rectangular pulse are normalized according to Equations 6.14a and b and the results are given in Table 6.4. (p, i) values in Table 6.4 are also plotted in the p-i diagram for the structure(Figure 6.8). It is seen that all the (p,i) values are below the iso-damage curve for the structure, which implies that that the foam covered structure will perform satisfactorily for the given projected threat.

Table 6.4 normalized transmitted pulse according to Equations 6.14a and 6.14b.

Blast loads item	p (Equation 6.14a)	i (Equation 6.14a)
1	0.6078	1.0227
2	0.6078	0.9297
3	0.6078	0.8677
4	0.6078	0.7748
5	0.6078	0.6198

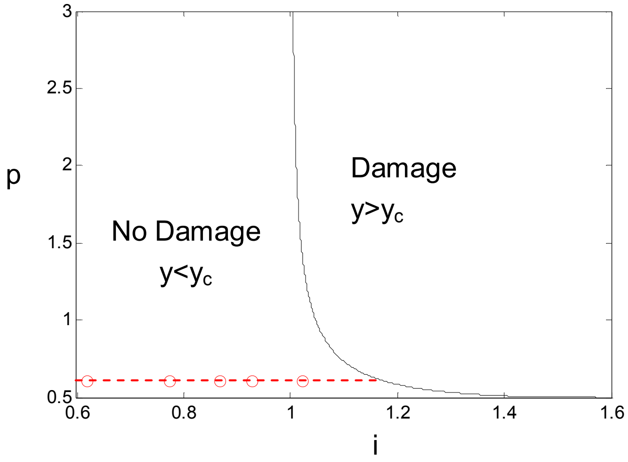

Figure 6.8: check the displacement criteria

6.4. Discussion

For a given structure, the p_σ-i_L diagram and p-i diagram can be plotted on one graph using the original impulse-pressure coordinates as shown in Figure 6.9. The purpose is to evaluate the effectiveness of foam in increasing the resistance of a structure again blast loads. In Figure 6.9, 'p-i transmitted' is the iso-damage curve for the transmitted rectangular pulse corresponding to the damage level defined by y_c=10mm. The 'p-i applied blast' curve is the iso-damage curve for triangular (original blast shape) corresponding to the damage level defined by y_c=10mm. The 'p-i for L = 0.2 m' curve is the iso-damage curve for L_{cr} = 0.2 m and the dotted line corresponds to the allowable stress in the material (which has been taken equal to σ_{po}). Comparing the p-i of the structure for the given triangular blast pressure with the allowable stress in the material it can be seen all combinations of pressure and impulse would produce significantly high stress in the material, which would produce significant material damage in the short-time scale. Thus the structure would be significantly degraded before structural motion develops. This would make the use of the single degree based on static load response and the resulting p-i diagram totally inaccurate.

The p-i diagram for the foam was obtained from the p_σ-i_L curve for foam with σ_{po} equal to 3.27 MPa and length equal to 20 mm. All values of p and i obtained from this curve, which correspond to applied blast pressure, would be transformed to rectangular pulse of stress amplitude equal to σ_{po}, the allowable stress. Therefore from a stress based criterion, the entire area under the p-i curve for L=0.2 m of the foam is safe. The foam transforms the original blast loads into a rectangular pulse with the magnitude equal to σ_{po}, which implies all the points under the ‘p-i for L = 0.2 m’ curve are shifted downward vertically onto the dotted line for checking of the deflection criteria. The p-i curve for a rectangular pulse is of significance for the displacement-based check. For the displacement criteria, it is observed on the figure the ‘p-i transmitted’ curve and the dotted line intersect at point A. To the left of point A, the ‘p-i transmitted’ curve is above the dotted line, meaning the displacement criteria is satisfied in this region. Since the transmitted stress is derived from the applied blast pressure through the foam, the area under ‘p-i for L = 0.2 m’ curve and to the left of point A is safe. Therefore with the foam, the area in the shaded part of the p-i diagram is now accessible while without the foam, only blast pressure amplitudes below the allowable stress are accessible.

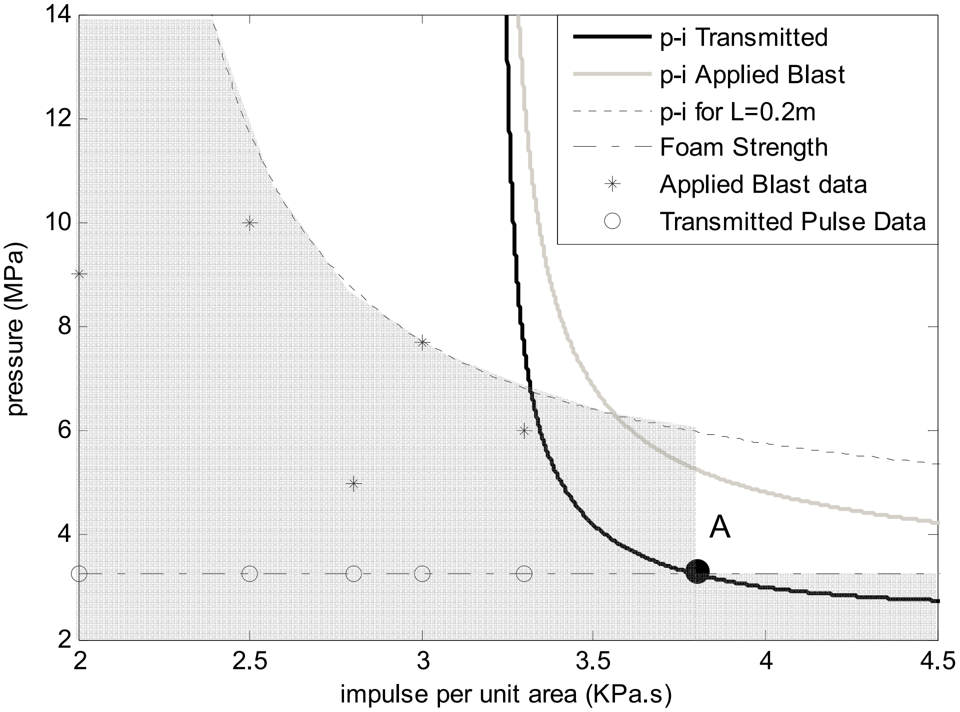

Figure 6.9: The effect of foam in the blast mitigation

If after decreasing the pressure, the impulse is too large, the structure could still fail in displacement. This is illustrated in Figure 6.10, where the allowable stress in the material determines the strength of the foam used in the application; using foam, the transmitted stress in the material could be decreased to the allowable stress. However, if the applied impulse is large, the pressure amplitude of a rectangular pulse which can be safely applied on the structure may be smaller than the transmitted stress. This is shown by the shaded area on the p-i diagram. In this situation there are two options available with the designer: (1) decrease the allowable stress; (2) increase the stiffness of the structure. The two cases are illustrated considering one, labeled O on the p-i diagram. At Point O, the stress amplitude of the transmitted pulse would not produce material damage in the short time scale associated with wave propagation. The stress amplitude, is however, higher than the value allowed by the iso-damage surface obtained from the displacement-based criterion for the given applied impulse.

The first option consists of decreasing the pressure amplitude of the transmitted pulse. Decreasing allowable stress in the material would limit the magnitude of the transmitted stress from the foam to a value which would be below the p-i diagram of the structure subjected to a rectangular pulse of the given impulse. This is shown by the line labeled I in Figure 6.10. A very low magnitude of transmitted stress can be achieved using a weak foam, with a low crushing strength. The length of foam required to ensure full attenuation the applied blast pressure loading (L_{cr}) may however be very large and ultimately impractical.

The second option consists of increasing the stiffness of the structure. The stiffness of the structure can be increased using external reinforcement such as bonded fiber reinforced (FRP) composite or steel laminates. In this situation, the stiffness of the structure (or the resistance offered by the structure to the displacement) is increased by the additional load carried by the external reinforcement. Therefore, the deflection of the structure for a given applied blast pressure loading decreases, resulting in an upward shift in the p-i iso-damage surface obtained using a displacement-based damage criterion (shown schematically as Line II in Figure 6.10). The level of stiffening can be designed such that the p-i diagram of the stiffened structure for a transmitted rectangular pulse would allow a rectangular stress pulse with a large impulse (Line II fro the stiffened structure passes through Point O).

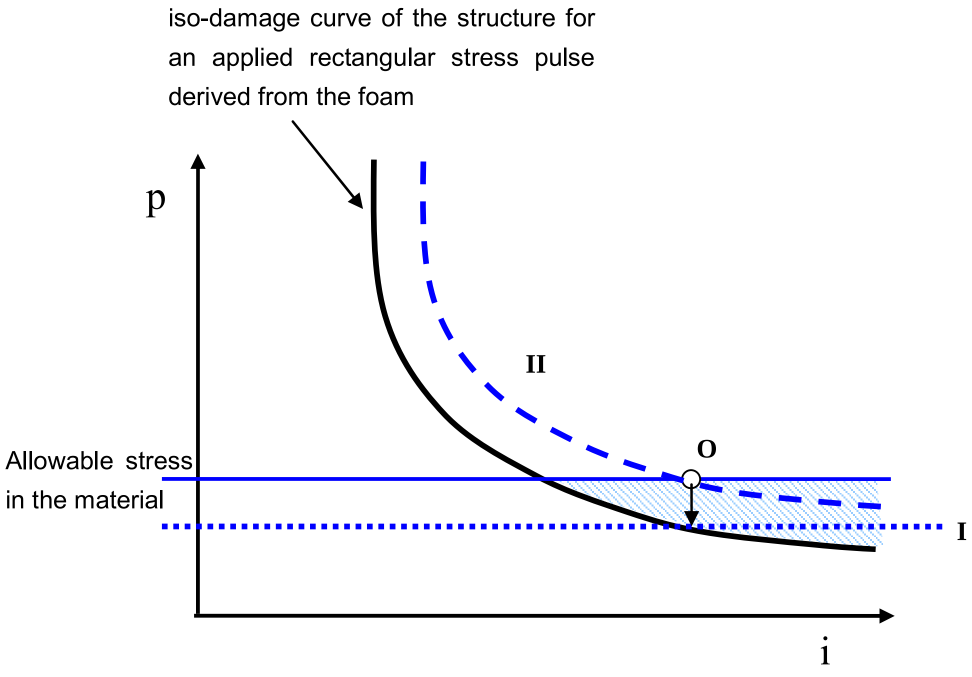

Figure 6.10: Schematic representation of the role of stiffness of the structure in the blast mitigation strategy.

6.4.1. Approach for using Blast Protection in a Blast Mitigation Strategy

Since blast evokes response associated with wave propagation and vibration motion, effective blast mitigation strategies should combine measures which are effective at the different time scales. Blast mitigation strategies should therefore combine protective material systems with strengthening measures. The use of the proposed protective material system comprising of low-strength cementitious material in a blast mitigation strategy for a structural component is shown in Figure 6.11. The strengthening system primarily provides additional out-of-plane structural reinforcement for deflection and is effective when the structural element starts to deflect. The low strength material, on the other hand, applied to the front face of the structural element controls the stress amplitude transmitted to the structure.

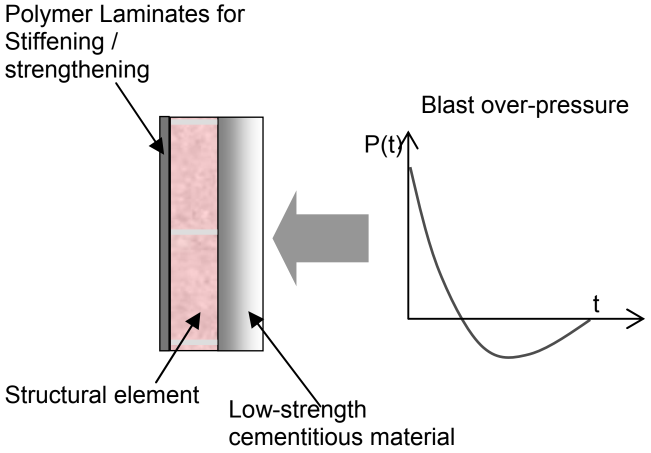

Figure 6.11: Schematic illustration of a blast mitigation strategy involving the combined use of protective material system and structural strengthening.

6.5. Conclusions

A design guideline is proposed for using foam cladding to protect the structural elements made of quasi-brittle material, such as reinforced, un-reinforced concrete or masonry, for a prescribed level of projected threat from a blast. The proposed design approach includes a two step process and considers damage mechanisms in two time scales associated with stress wave propagation and structural motion.

1. In the short time scale, the role of the cement foam is to reduce the magnitude of the stress wave in the structural element by attenuating the blast wave. An approach based on the p_σ-i_L diagram developed in this chapter is given for selecting the required length of a given foam to fully attenuate a blast wave of a prescribed magnitude and duration.
2. In the long time scale, the maximum deflection of foam-cladded structural elements needs to be checked. An approach for checking the maximum deflection is given by using the p-i diagram for transmitted rectangular pulses.
3. The benefit of foam in increasing the resistance of a structural element again blast loads in both time scales is clearly illustrated on the p-i diagram.

Bibliography:

ACI 229R-99, Controlled Low-Strength Materials, ACI Committee Report of Committee 229, American Concrete Institute, Farmington Hills, MI, 1999.

Army TM 5-1300/Navy NAVFAC P-397/Air Force AFR 88-22, Structures to Resist the Effects of Accidental Explosions, Washington, DC, 1990.

Baer M.R., A numerical study of shock wave reflections on low density foam, Shock Waves 1992, 2: 121–124.

Bear J. and Bachmat Y., Introduction to Modeling of Transport Phenomena in Porous Media, Kluwer Academic Publishers, 1990.

Bangash M.Y.H., Impact and explosion-analysis and design. Blackwell Scientific Publication, Oxford, 1993.

Ben-Dor G., Mazor G., Igra O., Sorek S. and Onodera H., Shock wave interaction with cellular materials, Part II: open cell foams: experimental and numerical results, Shock Waves 1994, 3:167–79.

Biot, M.A., Theory of propagation of elastic waves in fluid-saturated porous solid, Journal of the Acoustical Society of America 1956, 28: 168–191.

Blom F.J., Leyland, P., Analysis of fluid-structure interaction on moving airfoils by means of an improved ALE-method, AIAA Paper 1997, 97–1770.

Blom F.J., A monolithical fluid-structure interaction algorithm applied to the piston problem, Computer Methods in Applied Mechanics and Engineering 1998, 167: 369–391.

Briassulis G., Agui, J. and Andreopoulos Y., The structure of weakly compressible grid turbulence, Journal of Fluid Mechanics 2001, 432: 219–283.

Chen W., Zhang B. and Forrestal M.J., Split Hopkinson bar technique for low-impedance materials, Experimental Mechanics 1999, 39(2):81–85.

Chen W., Lu F. And Zhou B., Quartz-crystal-embedded split Hopkinson pressure bar for soft materials, Experimental Mechanics 2000, 40(1):1–6.

Conley C.H., and Gregory F.H., Vulnerability of Structural Panels to Blast Effects, proceedings of the 70th Shock & Vibration Symposium 1999, Albuquerque, NM, 15–19.

Conley C.H. and Gregory F.H., Modeling of Blast-Loaded Structural Panels, Proceedings of the 8th Annual U.S. Army Research Laboratory/United States Military Academy Technical Symposium 2000, West Point, NY, 221–235.

Cooper G.J., Townend D.J., Cater S.R. and Pearce B.P., The role of stress waves in thoracic visceral injury from blast loading: modification of stress transmission by foams and high-density materials, Journal of Biomechanics 1991, 24(5):273–85.

Courant R. and Friedrichs K.O., Supersonic flow and shock waves, Springer-Verlag, 1977.

Davidson J. S., Fisher J. W., Hammons M. I., Porter J. R. and Dinan R. J., Failure mechanisms of polymer-reinforced concrete masonry walls subjected to blast, ASCE Journal of Structural Engineering 2005, 131: 1194-1206.

Deshpande, V. and Fleck N., High strain rate compressive behaviour of aluminum alloy foams, International Journal of Impact Engineering 2000, 24 (3): 277–298.

Deshpande, V.S., Fleck, N.A., One-dimensional response of sandwich plates to underwater shock loading, Journal of the Mechanics and Physics of Solids 2005, 53: 2347–2383

Donea J., Giuliani S. and Halleux J.P., An arbitrary Lagrangian-Eulerian finite element method for transient dynamic fluid-structure interactions, Computer Methods in Applied Mechanics and Engineering 1982, 33: 689–723.

Dongen M.V., Shock Wave Science and Technology Reference Library, Vol.1, Springer, 2007.

Eamon C. D., Baylot J. T. and O'Daniel J. L., Modeling concrete masonry walls subjected to explosive loads, ASCE Journal of Engineering Mechanics 2004, 130(9): 1098-1106.

Farhat C. and Lin T.Y., A structure attached corotational fluid grid for transient aeroelastic computations, AIAA Journal 1993, 31(3), 597–599.

Fleck N.A. and Deshpande V.S., The resistance of clamped sandwich beams to shock loading, Journal of Applied Mechanics 2004, 71 (3): 386–401.

Gibson L.J. and Ashby M.F., Cellular Solids: Structure and Properties, Cambridge University Press, 1999.

Gong M., Mutual Interactions between Shock Waves and Structures, PhD Thesis, City University of New York, New York, NY, 2006.

Godunov, S. K., A Difference Scheme for Numerical Solution of Discontinuous Solution of Hydrodynamic Equations, Math. Sbornik 1959, 47: 271-306, translated US Joint Publ. Res. Service, JPRS 7226, 1969.

Guruprasad S. and Mukherjee A., Layered sacrificial claddings under blast loading, Part-I Analytical studies, International Journal of Impact Engineering 2000a, 24: 957–973.

Guruprasad S. and Mukherjee A., Layered sacrificial claddings under blast loading, Part-II Experimental studies, International Journal of Impact Engineering 2000b, 24: 975–984.

Gvozdeva L.G., Faresov Y.M. and Fokeev V.P., Interaction of air shock waves with porous compressible materials, Journal of Applied Mechanics and Technical Physics 1985, 26(3): 401–405.

Hamoush, S.A., McGinley, M.W., Mlakar, P., Scott, D., and Murray, K., Out-of-Plane Strengthening of Masonry Walls with Reinforced Composites, Journal of Composites for Construction 2001, 5(3): 139–145.

Hanssen A.G., Enstock L. and Langseth M., Close-range blast loading of aluminium foam panels, International Journal of Impact Engineering 2002, 27: 593–618.

Hallquist J.O., LS-DYNA Theoretical Manual, Livermore Software Technology Corporation, Livemore, California, 1998.

Harrigan J.J., Peng C. and Reid S.R., Inertia effects in impact energy absorbing materials and structures, International Journal of Impact Engineering 1999, 22: 955-979.

Hinman E., Approach for Designing Civilian Structures Against Terrorist Attack, in Concrete and Blast Effects, American Concrete Institute Special Publication – 175, Ed. W. Bounds, 1998

Hint C.W., Amsden A.A. and Cook J.L., An arbitrary Lagrangian Eulerian coupling method for all flow speeds, Journal of Computational Physics 1974, 14: 227–253.

Hopkins H.G., The method of characteristics and its application to the theory of stress waves in solids, In: Heyman J., Leckie F.A. (Eds.), Engineering Plasticity, Cambridge University Press 1968, 277-315.

Hutchinson J.W., Ashby M.F., Evans T., Wadley H.N.G., Gibson L.J. and Fleck N.A., Metal foams: A design guide, Society of Automotive Engineers Inc, 2000.

Kaiser M.A., Advancements in the Split Hopkinson Bar Test. M.S. Thesis, Department of Mechanical Engineering, The Virginia Polytechnic Institute and State University, 1998.

Kenny L.D., Mechanical properties of particle stabilised aluminium foam, Materials Science Forum 1996, Vols 217–222: 1883-1890.

Kingery C. N. and Bulmash G, Airblast Parameters from TNT Spherical Air Burst and Hemispherical Surface Burst, ARBRL-TR-02555, Ballistic Research Laboratory, Aberdeen Proving Ground, MD, 1984.

Kolsky H., An investigation of the mechanical properties of materials at very high rates of loading, Proceedings of the Physical Society: Section B 1949, 62 (11):676–700.

Leveque R.J., Finite Volume Methods for Hyperbolic Problems, Cambridge University Press, 2002.

Leveque R.J., Finite-Volume method for non-linear elasticity in heterogeneous media, International journal for numerical methods in fluids 2002, 40: 93–104.

Leveque R.J. and Yong D.H., Solitary waves in layered nonlinear media, SIAM Journal on Applied Mathematics 2003, 63:1539–1560.

Levi-Hevroni D., Levy A., Ben-Dor G. and Sorek S., Numerical investigation of the propagation of planar shock waves in saturated flexible porous materials: development of the computer code and comparison with experimental results, Journal of Fluid Mechanics 2002, 462: 285-306.

Levy A., Ben-Dor G., Skews B.W. and Sorek S., Head-on Collision of Normal Shock Waves with Rigid Porous Materials, Experiments in Fluids 1993, 15: 183–190.

Levy A., Sorek S., Ben-Dor G. and Bear J., Evolution of the balance equations in saturated thermoelastic porous media following abrupt simultaneous changes in pressure and temperature, Transport in Porous Media 1995, 21: 241–268.

Levy A., Ben-Dor G. and Sorek S., Numerical Investigation of the Propagation of Shock Waves in Rigid Materials: Development of computer Code and Comparison with Experimental Results, Journal of Fluid Mechanics 1996a, 324: 163–179.

Levy A., Sorek S., Ben-Dor G. and Skews B., Waves propagation in saturated rigid porous media: analytical model and comparison with experimental results, Fluid Dynamics Research 1996b, 17(2): 49-65.

Li H. and Ben-Dor G., Head-on interaction of weak planar shock waves with flexible porous materials: analytical model, International Journal of Multiphase Flow 1995, 21(5): 941–947.

Li Q.M. and Meng H., Attenuation or enhancement–a one-dimensional analysis on shock transmission in the solid phase of a cellular material, International Journal of Impact Engineering 2002, 27: 1049–1065

Li Q.M. and Meng H., Pressure-Impulse Diagram for Blast Loads Based on Dimensional Analysis and Single-Degree-of-Freedom Model, Journal of Engineering Mechanics 2002, 128(1): 87–92.

Lopatnikova S.L., Gamaa B.A., Haquea M.J., Krauthausera C., Gillespie J.W., Guden M. and Hall I.W., Dynamics of metal foam deformation during Taylor cylinder–Hopkinson bar impact experiment, Composite Structures 2003, 61: 61–71.

Lopatnikova S.L., Gamaa B.A., Haquea M.J., authausera C. andlespie J.W., High-velocity plate impact of metal foams, International Journal of Impact Engineering 2004, 30: 421–445.

Lu G. and Yu T.X., Energy Absorption of Structures and Materials, Woodhead Publishing Ltd., Cambridge, UK, 2003.

Ma G.W. and Ye Z.Q., Analysis of foam claddings for blast alleviation, International Journal of Impact Engineering 2007, 34: 60–70.

Monti R., Normal shock wave reflection on deformable solid walls, Mecccanica 1970, 4: 285-296.

Morland L.W., The propagation of plane irrotational stress waves through an elastoplastic medium, Philosophical Transactions of the Royal Society of London, Series A, Mathematical and Physical Sciences 1959, 251:341-383.

Mosalam K.M. and Mosallam A.S., Nonlinear Transient Analysis of Reinforced Concrete Slabs Subjected to Blast Loading and Retrofitted with CFRP Composites, Composites Part B: Engineering 2001, 32: 623-636.

Mukai,T., Miyoshib, T., Nakanoc, S., Somekawaa H., and Higashic, K., Compressive response of a closed-cell aluminum foam at high strain rate, Scripta Materialia 2005, 54(4): 533–537.

National Research Council, Blast Mitigation for Structures: 1999 Status Report on the Dtra/tswg Program, National Academy Press, Washington, DC,. 1999.

Nemat-Nasser S., Kang W.J., McGee J.D., Guo W.G. and Isaacs J.B., Experimental investigation of energy-absorption characteristics of components of sandwich structures, International Journal of Impact Engineering 2007, 34: 1119–1146.

Nowinski, J.L., On the Propagation of Finite Disturbances in Bars of Rubberlike Materials, Journal of Engineering for Industry 1965, 64: 523–529

Olim M., Van Dongen M.E.H., Kitamura T. and Takayama K., Numerical simulation of the propagation of shock waves in compressible open-cell porous foams, International Journal of Multiphase Flow 1994, 20(3): 557–568.

Radford D.D., Deshpande V.S. and Fleck N.A., The use of metal foam projectiles to simulate shock loading on a structure, International Journal of Impact Engineering 2005, 31:1152–1171.

Reid, S. and Peng,C., Dynamic uniaxial crushing of wood, International Journal of Impact Engineering 1997, 19: 531–570.

Roberto M., Measurement of strain rate sensitivity of aluminium foams for energy dissipation, International Journal of Mechanical Sciences 2005, 47: 26–42.

Roe P.L. and Pike J., Efficient Construction and Utilisation of Approximate Riemann Solutions, Computing Methods in Applied Science and Engineering, North-Holland, 1984.

Saad, M., Compressible Fluid Flow, Prentice Hall, 1998.

Skews, B.W., The reflected pressure field in the interaction of weak shock waves with a compressible porous foams, Shock Waves 1991, 1: 205–211.

Skews B.W., Atkins M.D. and Seitz M.W., The impact of shock wave on porous compressible foams, Journal of Fluid Mechanics 1993, 253: 245–265.

Smith P.D. and Hetherington J.G., Blast and Ballistic Loading of Structures, Butterworth Heinemann, 1994.

Standley E., Umnova O., Attenborough K., Cummings A. and Dutta P., Shock Wave Reflection Measurements on Porous Materials, Noise Control Engineering Journal 2002, 50(6): 224-230.

Subramaniam K.V., Nian W. and Andreopoulos Y., Blast Response Simulation of an Elastic Structure: Evaluation of the Fluid-Structure Interaction Effect, International Journal of Impact Engineering 2009, 36(7): 965-974.

Tan P.J., Reid S.R., Harrigan J.J., Zou Z. and Li S., Dynamic compressive strength properties of aluminum foams, Part I: experimental data and observations, Journal of the Mechanics and Physics of Solids 2005a, 53: 2174–2205.

Tan P.J., Reid S.R., Harrigan J.J., Zou Z. and Li S., Dynamic compressive strength properties of aluminum foams, Part II: 'shock' theory and comparison with experimental data and numerical models, Journal of the Mechanics and Physics of Solids 2005b, 53: 2206–2230.

Tan. P.J., Reid, S.R., Harrigan, J.J., Discussion: "The Resistance of Clamped Sandwich Beams to Shock Loading" (Fleck, N. A., and Deshpande, V. S., 2004, ASME J. Appl. Mech., 71, pp. 386–401). Journal of Applied Mechanics 2005c, 72: 978–979.

Taylor, G., The pressure and impulse of submarine explosion waves on plates. In: Batchelor, G. (Editor.), Aerodynamics and the mechanics of projectiles and explosions, vol. III, Cambridge University Press. pp: 287–303.

Toro E.F., Riemann Solvers and Numerical Methods for Fluid Dynamics: A Practical Introduction, Springer, 1999.

Unified Facilities Criteria (UFC) 4-023-03, Design of Buildings to Resist Progessive Collapse. Department of Denfence, Washington, D.C., 2005.

Van Leer, B., Towards the Ultimate Conservative Difference Scheme, V. A Second Order Sequel to Godunov's Method, Journal of Computational Physics, 1979, 32, 101–136.

Ye Z. Q. and Ma G. W., Effects of Foam Claddings for Structure Protection against Blast Loads, Journal of Engineering Mechanics 2007, 133(1): 41–47.

Yi Z., Blast Load Effects on Highway Bridges, PhD Thesis, The City University of New York, 2009.